IB 2019-74

Experimental study of the inner layer of an adverse-pressure-gradient turbulent boundary layer

Tobias Knopp

Deutsches Zentrum
für Luft- und Raumfahrt

Berichts.-Nr.: **DLR-IB-AS-GO-2019-74**

Verfasser: Tobias Knopp

Titel: Experimental study of the inner layer of an adverse-pressure-gradient turbulent boundary layer

Datum:

Auftraggeber:

Auftrags-Nr.:

Vorgesehen für:

Der Bericht umfaßt:
104 Seiten einschl.
17 Tabellen
63 Bilder
136 Literaturstellen

Vervielfältigung und Weitergabe dieser Unterlagen sowie Mitteilung ihres Inhalts an Dritte, auch auszugsweise, nur mit Genehmigung X des DLR X des Auftraggebers.

D L R

Institut für Aerodynamik und Strömungstechnik
Bunsenstraße 10
37073 Göttingen
Deutschland

Abteilung AS-CAS

DLR

Titel: Experimental study of the inner layer of an adverse-pressure-gradient turbulent boundary layer

We present an analysis of the inner layer of adverse-pressure-gradient turbulent boundary layers at Reynolds numbers up te Re-theta=57000. The major aim is to determine the resilience of the log-law, the possible change of the log-law slope and the appearance of a square-root law above the log-law at significant adverse pressure gradients. The second objective is to characterise the total shear stress. The third aim is to provide a well-defined test case for the validation and improvement of numerical flow simulation methods. The experiment was performed within the DFG funded project "Analyse turbulenter Grenzschichten mit Druckgradient bei großen Reynoldszahlen mit hochauflösenden Vielkameramessverfahren" and the evaluation of the presented results was performed within the DLR project VicToria

We designed and performed a new wind-tunnel experiment, in which the turbulent boundary layer flow of interest develops on the side wall of the wind-tunnel and then follows an accelerating ramp and a long flat plate at almost zero pressure gradient. Then the flow enters into the adverse pressure gradient section, first along a curved surface and then on a flat plate. We use a large-scale overview particle imaging velocimetry method for characterising the streamwise evolution of the flow over a streamwise distance of 15 boundary layer thicknesses. In the focus region, we use microscopic and Lagrangian particle tracking velocimetry to measure the mean velocity and the Reynolds stresses down to the viscous sublayer. Oil-film interferometry is used for the complementary direct measurement of the wall shear stress.

In the adverse pressure gradient region we observe a composite form of the mean velocity profile with a thin log law region and a square-root law above up to 12% boundary layer thickness. We find lower values for the log-law slope coefficient than for zero pressure gradient boundary layers, but the reduction is within the uncertainties in the measurement and possible history effects. The total shear stress and the turbulent viscosity in the inner layer can be described by an analytical model whose parameters are the pressure gradient parameter and the acceleration parameter based on the streamwise gradient of the wall shear stress.

Then we use a data base of adverse pressure gradient turbulent boundary layer flows at large Reynolds numbers from the literature. We find that the mean velocity profiles for different flows almost collapse provided that both the pressure gradient parameter and the wall shear stress gradient parameter are close to each other. Finally we describe and discuss the effects of the convex curvature and the relaxation of upstream curvature effects on a flat plate. The streamwise eddy-turnover distance indicates that the flow relaxes fast in the inner layer, whereas the turnover length is strongly increasing in the outer part of the boundary layer.

DEUTSCHES ZENTRUM FÜR LUFT-
UND RAUMFAHRT E.V.

Institut für Aerodynamik und Strömungstechnik

Institutsleiter::

(Prof. Dr. Andreas Dillmann)

Verfasser:

T. Knopp

(Dr. Tobias Knopp)

Abteilungsleiter:

C. Grabe

(Dr. Cornelia Grabe)

Datum: 15.11.19 **Bearbeitet:**	**Abteilung:** AS-CAS	**Bericht:** IB-AS-GO-2019-74

Contents

Abstract

We present an analysis of the inner layer of adverse-pressure-gradient turbulent boundary layers at Reynolds numbers up to $Re_\theta = 57000$. The major aim is to determine the resilience of the log-law, the possible change of the log-law slope and the appearance of a square-root law above the log-law at significant adverse pressure gradients. The second objective is to characterise the total shear stress. The third aim is to provide a well-defined test case for the validation and improvement of numerical flow simulation methods. We designed and performed a new wind-tunnel experiment, in which the turbulent boundary layer flow of interest develops on the side wall of the wind-tunnel and then follows an accelerating ramp and a long flat plate at almost zero pressure gradient. Then the flow enters into the adverse pressure gradient section, first along a curved surface and then on a flat plate. We use a large-scale overview particle imaging velocimetry method for characterising the streamwise evolution of the flow over a streamwise distance of 15 boundary layer thicknesses. In the focus region, we use microscopic and Lagrangian particle tracking velocimetry to measure the mean velocity and the Reynolds stresses down to the viscous sublayer. Oil-film interferometry is used for the complementary direct measurement of the wall shear stress.

In the adverse pressure gradient region we observe a composite form of the mean velocity profile with a thin log law region and a square-root law above up to $0.12\delta_{99}$. We find lower values for the log-law slope coefficient than for zero pressure gradient boundary layers, but the reduction is within the uncertainties in the measurement and possible history effects. The total shear stress and the turbulent viscosity in the inner layer can be described by an analytical model whose parameters are the pressure gradient parameter and the acceleration parameter based on the streamwise gradient of the wall shear stress. Then we use a data base of adverse pressure gradient turbulent boundary layer flows at large Reynolds numbers from the literature. We find that the mean velocity profiles for different flows almost collapse provided that both the pressure gradient parameter and the wall shear stress gradient parameter are close to each other. Finally we describe and discuss the effects of the convex curvature and the relaxation of upstream curvature effects on a flat plate. The streamwise eddy-turnover distance indicates that the flow relaxes fast in the inner layer, whereas the turnover length is strongly increasing in the outer part of the boundary layer.

Chapter 1

Introduction

Turbulent boundary layers subjected to an adverse pressure gradient still pose many open questions. At the same time, they have a high relevance in many technical applications. Lift generation on airplane wings, thrust generation using turbomachinery blades, and energy harvesting using wind turbine blades are just a few examples out of many. Among these flows, the flow around airplane wings are special due to the very high Reynolds numbers. These flows are characterised by a streamwise changing pressure gradient and surface curvature. Modern commercial transport aircrafts use so-called supercritial airfoil geometries since the 1970s. In the rear part of the airfoil, the flow on the upper side experiences an adverse pressure gradient and a convex surface curvature. On the lower side the geometry is S-shaped with a convex followed by a concave curvature. Consequently the pressure gradient is changing from adverse to favourable. Due to the strong changes in streamwise direction, these flows show significant effects of non-equilibrium, relaxation and flow history.

The proper mathematical description of the statistically averaged mean flow of a turbulent boundary layer at a significant adverse pressure gradient (APG) is still under debate. For boundary layers at zero-pressure gradient, there is large experimental support and agreement in the literature that the mean velocity in the inner layer can be described by the log-law

$$u^+ = \frac{1}{\kappa}\log(y^+) + B \tag{1.1}$$

for sufficiently large Reynolds numbers, see e.g. Rotta [1962], Österlund et al. [2000], and Marusic et al. [2013]. Therein, the superscript + denotes the viscous units. The values for the slope coefficient κ and for the intercept B are still under discussion in the literature, see Örlü et al. [2010] for an overview. During the years, besides the values $\kappa = 0.41$ and $B = 5.0$ by Coles and Hirst [1969], also lower values were proposed, e.g., $\kappa = 0.384$ and $B = 4.17$ found by Österlund et al. [2000].

Regarding the mean flow structure of canonical wall-bounded flows, i.e. turbulent channel and pipe flows and turbulent boundary layers at zero pressure gradient, traditionally, these flows are divided into four layers, i.e., the viscous sublayer ($y^+ < 5$), the buffer layer ($5 < y^+ < 30$), the logarithmic layer ($30 < y^+ < 0.15\delta_{99}^+$) and the wake layer ($y^+ > 0.15\delta_{99}^+$), see e.g., Wei et al. [2005a] for a review. Therein δ_{99} denotes the boundary layer thickness. A historical overview over the extent of the log-layer in the literature can be found in Örlü et al. [2010]. In the more recent publications, there is agreement on the outer edge of the log-layer near $y = 0.15\delta_{99}$, see Örlü et al. [2010] and Marusic et al. [2013]. The region $y < 0.15\delta_{99}$ will be referred to as the inner layer. Regarding the beginning of the log-layer, larger values ranging from $y^+ > 150$ up to $y^+ > 300$ have been proposed recently. A mesolayer located between the buffer layer and the log-layer in the region $30 < y^+ < 300$ was proposed by George and Castillo [1997]. Another view was given by Hultmark et al. [2012], who found for turbulent pipe flows at very high Reynolds numbers the existence of a region where the log-law for the mean velocity and a logarithmic profile for the streamwise (and spanwise) turbulence intensities hold simultaneously, as suggested by Townsend [1976]. This result was supported in Marusic et al. [2013] for turbulent boundary layer flows, leading to the proposal $3Re_\tau^{1/2} < y^+ < 0.15Re_\tau$, with $Re_\tau = \delta_{99}^+$, for this region.

For flows with a significant adverse pressure gradient, there is no consensus on the law-of-the-wall in the literature, and the discussion described in Alving and Fernholz [1995a] is still open. A first hypothesis is that the log-law (1.1) still holds and that slope $1/\kappa$ and intercept B still have the same value as for a flat-plate turbulent boundary layer at zero pressure gradient (ZPG), but that the region occupied by the log-law is progressively reduced with increasing adverse pressure gradient. This hypothesis was called the "progressive breakdown" of the law of the wall in Galbraith et al. [1977]. It was suggested from the measurements by Wieghardt and Tillmann [1944] and advocated, among other, by Coles [1956], Perry [1966], Coles and Hirst [1969], Galbraith et al. [1977], Granville [1989], and Huang and Bradshaw [1995]. We note that the empirical two-parameter family of mean velocity profiles by Thompson [1967] also uses the ZPG log-law for $y/\delta_{99} < 0.05$. This is of interest for the present work, since this profile family was found to be successful to describe a large number of adverse pressure gradient flows.

In conjunction with the first hypothesis, Perry [1966] proposed that above the log-law region there is a so-called half-power law region. In the special case of a vanishing wall shear stress close to separation due to a continuous APG, the half-power law extends almost down to the wall. This proposal by Stratford [1959] was recently supported by direct numerical simulations in Coleman et al. [2017] and Coleman et al. [2018]. Alternative composite wall-laws based on a log-region in the inner part and a different form of the half-power law in the outer part of the inner layer were proposed for boundary layers by Kader and Yaglom [1978], by Kiel [1995], and by Afzal [2008], and for Couette-Poiseuille flow by Telbany and Reynolds [1980] and by Vieth [1996]. Moreover, Kader and Yaglom [1978] and Telbany and Reynolds [1980] proposed a model for the thickness of the log-law region. We mention also the work by Perry and Schofield [1973] which was refined in Schofield [1981] and Schofield [1986]. A three-layer structure of the law-of-the-wall was proposed by Durbin and Belcher [1992]. For a mathematical approach we refer to Scheichl and Kluwick [2006, 2007].

A second hypothesis is that, in the log-law region, the coefficients κ and B change their values. Nickels [2004] proposed a functional dependence of κ on the so-called pressure gradient parameter in inner scaling Δp_x^+

$$\Delta p_x^+ = \frac{\nu}{\rho u_\tau^3}\frac{\mathrm{d}P_\mathrm{w}}{\mathrm{d}x}\,. \tag{1.2}$$

This proposal was studied for sink flows by Dixit and Ramesh [2008]. Regarding a possible change of κ and B, a number of data sets were evaluated by Nagib and Chauhan [2008], who found an empirical correlation between κ and B. Experimental results by Nagano et al. [1991] could indicate a change in B, and also the DNS data by Lee and Sung [2009] give indications that κ and B may change. A recent work by Luchini [2017] also gives some indications.

A third hypothesis in that direction is that the pressure gradient causes "[...] a change in the character of the velocity distribution over the entire region [...]" occupied by the log-law in a ZPG flow, see Galbraith et al. [1977], which is called a "general breakdown" of the log-law. Some authors proposed a single formulation for the entire inner layer based on a generalised half power law, see Szablewski [1960], Townsend [1961], McDonald [1969], van den Berg [1975], Skote and Henningson [2002]. For the theoretical analysis therein, it is assumed that the half-power law is accompagnied by a region, where the total shear stress grows linearly with the wall-distance, see e.g., Szablewski [1954] and Brown and Joubert [1969].

An increasing number of new experiments and numerical simulations for turbulent boundary layers at adverse pressure gradient have been provided during the last decade. Wind tunnel experiments were performed for equilibrium flows by Atkinson et al. [2016], and for streamwise changing flows by e.g. Drobniak et al. [2010], Monty et al. [2011], Harun et al. [2013], Cuvier et al. [2014], Atkinson et al. [2014], Knopp et al. [2015], Soria et al. [2016], Schatzman and Thomas [2017], and Vila et al. [2017]. Recent numerical simulations of equilibrium turbulent boundary layer flows at adverse pressure gradient were performed by Lee and Sung [2008], and Kitsios et al. [2016, 2017], and for the Couette-Poiseuille flow by Coleman et al. [2015], for which the special case of a zero skin friction flow was studied in Coleman et al. [2017]. Streamwise developing turbulent boundary layer flows were studied in e.g. Inoue et al. [2013], Gungor et al. [2014, 2016], Vinuesa et al. [2018], and Coleman et al. [2018].

The scaling and characterisation of turbulent boundary layers with pressure gradients has also been attracting recent research activities. Regarding the question of scaling and self-similarity of the mean velocity profiles and the Reynolds stresses in the outer part of the boundary layer we refer to e.g. Mellor and Gibson [1966], Elsberry et al. [2000], Schatzman and Thomas [2017], Maciel et al. [2006a], Gungor et al. [2016], and Maciel et al. [2018]. For the inner layer, the classical scaling is based on viscous units, whereas Mellor [1966] proposed to use a velocity scale based on the pressure gradient. Nickels [2004] proposed to use a velocity scale which is based on the total shear stress at the outer edge of the viscous sublayer.

The question of characteristic mean flow parameters which govern the behaviour of mean velocity and Reynolds stresses is still an open question. There is agreement in the literature that the pressure gradient plays a central role, and it is used in the form of the pressure gradient parameter Δp_x^+, or using the scaling by Rotta and Clauser or by Zagarola and Smits [1997], see Maciel et al. [2018]. The question of additional relevant parameters is still open and thus the complexity of the parameter space needed to describe turbulent boundary layers with pressure gradients. Monty et al. [2011] used the pressure gradient parameter in the Rotta-Clauser scaling and the acceleration parameter $K = \nu U_e^{-2} \mathrm{d}U_e/\mathrm{d}x$ where U_e denotes the local free-stream velocity at the boundary layer edge. For the inner layer, the acceleration parameter

$\Delta u^+_{\tau,x} = \nu u_\tau^{-2} \mathrm{d}u_\tau/\mathrm{d}x$ based on the streamwise derivative of the friction velocity (or equivalently, of the wall shear stress) was used in addition to Δp^+_x by Perry et al. [1966], van den Berg [1973] and Galbraith et al. [1977]. In Bobke et al. [2017] the local boundary layer thickness $Re_\tau = \delta^+_{99}$ was used as a second parameter.

For flows with pressure gradients in conjunction with streamwise surface curvature, the scaling properties become even more challenging, and only a small number of experiments can be found in the literature, e.g., by Baskaran et al. [1987] and by Bandyopadhyay and Ahmed [1993]. The effect of surface curvature has been studied in depth since the pioneering work by Bradshaw [1970]. For the present work the focus in on convex curvature. The magnitude of curvature effects depends on the ratio of the local boundary layer thickness δ_{99} to the local radius of curvature R_c. Large curvature effects are associated with values for $\delta_{99}/R_c > 0.05$, which were investigated by e.g. So and Mellor [1973] and Gillis and Johnston [1983]. An impulse like curvature was studied in Smits et al. [1979]. Values of $\delta_{99}/R_c < 0.01$ are associated with mild curvature in the literature, which were studied e.g. by Gibson et al. [1984], and by Ramaprian and Shivaprasad [1978]. The relaxation of a turbulent boundary layer from curvature on a flat plate was studied for the zero-pressure gradient case by Gillis and Johnston [1983] and by Alving et al. [1990]. Baskaran et al. [1987] and Bandyopadhyay and Ahmed [1993] studied the effect of an abrupt change in surface curvature which can initiate the growth of an internal boundary layer. Baskaran et al. [1987] studied the effect of a perturbation in wall curvature for a flow with prolonged convex curvature. They performed experiments for a wall mounted curved hill with an abrupt change in curvature and a free wing based on the same convex curvature geometry. They describe that an abrupt change in surface curvature can initiate the growth of an internal boundary layer. The internal layer grows as an independent boundary layer beneath a turbulent free-shear layer, and establishes its own inner and outer region during its development in streamwise direction. Bandyopadhyay and Ahmed [1993] designed a flow experiment with an abrupt change of curvature and pressure gradient. The curvature changes on one wall from flat to convex-concave and on the other from flat to concave-convex, and then the flow relaxes on a flat wall.

Once a wall-law for the mean velocity at adverse presssure gradient is discovered, this could stimulate the improvement of RANS turbulence models, see Rao and Hassan [1998] and Knopp [2016], and of near-wall models and wall-functions for hybrid RANS/LES methods. A significant improvement in the predictive accuracy of RANS modelling is needed to reach the vision to design and optimise an aircraft based on computer simulations, see Bush et al. [2019]. The computational costs of direct numerical simulations of realistic aircrafts with their large ratio of viscous surface area compared to the boundary layer thickness is unfeasible even for a single flight case, see Spalart [2015], but the design and certification of an aircraft require data for several millions of flight conditions.

We have optimism that a step towards a wall-law for adverse pressure gradients, even if it may be only empirically motivated and cannot account for all higher order effects in full detail, can lead to new questions, which may lead to a deeper understanding of turbulent boundary layers at adverse pressure gradients e.g. using the idea of organised structures, see, for example, Adrian [2007], Lee and Sung [2009], Marusic and Monty [2019], and Bross et al. [2019].

This paper is organised as follows. After a short review of the classical and recent theory of turbulent boundary layers with pressure gradients in section 2, we describe the new wind-tunnel experiment in section 3. The aim of the experiment is to study possible changes of the log-law slope coefficient according to the theory by Nickels [2004] and the appearance of a sqrt-law at large Re by achieving values of $\Delta p_x^+ > 0.01$ and large Reynolds numbers, i.e., $Re_\theta > 30000$, in the adverse pressure gradient region. The characterisation of pressure gradient and curvature is given in section 4. The results for the zero pressure gradient region upstream of the region of the adverse pressure gradient are presented in section 5. The results for the mean velocity in the adverse pressure gradient region are described in section 6. The experimental data support a composite form of the mean velocity profile by Perry et al. [1966] with a thin log-law region and a sqrt-law region above. In section 7 we study the mean-momentum balance and the turbulent shear stress. The aim is to identify the dominant terms of the mean-momentum balance and to characterise them using suitable flow parameters. This will lead to a two-parameter model for the total shear stress based on the pressure gradient parameter Δp_x^+ and the wall-shear stress gradient parameter $\Delta u_{\tau,x}^+$. In section 8 we compare the results for the present flow with other representative turbulent boundary layer flows at APG using a data base from the literature. The results indicate similarity of the mean velocity profiles in the inner layer among different flows for similar values of Δp_x^+ and $\Delta u_{\tau,x}^+$, despite differences in the upstream history of the flows. In section 9 we attempt to assess the role of history effects and surface curvature for the present experiment, and we study the question if other, possibly higher order terms with additional parameters, determine the details of the mean velocity profiles in the region $y^+ < 150$. The main conclusions of the analysis are summarised in section 10.

Chapter 2

Classical theory

2.1 Boundary layer theory

In this work we assume for simplicity a two-dimensional, incompressible turbulent boundary layer flow without external forces. We assume a wall-fitted local coordinate system with streamwise wall-parallel direction x, wall-normal direction y, and mean velocity components U (streamwise wall-parallel) and V (wall-normal). We assume that the following boundary layer approximation of the U-momentum equation can be used

$$\nu \frac{\partial^2 U}{\partial y^2} - \frac{\partial \overline{u'v'}}{\partial y} = \frac{1}{\rho}\frac{\mathrm{d}P_\mathrm{w}}{\mathrm{d}x} + U\frac{\partial U}{\partial x} + V\frac{\partial U}{\partial y} - \nu\frac{\partial^2 U}{\partial x^2} + \frac{\partial}{\partial x}\left(\overline{u'^2} - \overline{v'^2}\right) . \tag{2.1}$$

Therein the relation $P(x,y) = P_\mathrm{w}(x) - \overline{v'^2}(x,y)$ is used, which can be obtained by integration of the boundary layer equation for the V-momentum

$$\frac{1}{\rho}\frac{\partial P}{\partial y} + \frac{\partial \overline{v'^2}}{\partial y} = 0$$

from the wall up to the wall-distance y in wall-normal direction, see Pope [2000], Hinze [1975]. Due to integration from the wall, the wall-pressure $P_\mathrm{w}(x)$ arises, whereas integration from the boundary layer edge leads to the free-stream pressure, which is used in Hinze [1975].

In the sequel, we neglect the term $\nu\partial^2 U/\partial x^2$. Then for the total shear stress τ with

$$\frac{\tau}{\rho} \equiv \nu\frac{\partial U}{\partial y} - \overline{u'v'} \tag{2.2}$$

integration of equation (2.1) from the wall to the wall-distance y gives the relation

$$\frac{\tau}{\rho} = \frac{\tau_w}{\rho} + \frac{1}{\rho}\frac{\mathrm{d}P_\mathrm{w}}{\mathrm{d}x}y + \int_0^y U\frac{\partial U}{\partial x}\mathrm{d}\tilde{y} + \int_0^y V\frac{\partial U}{\partial \tilde{y}}\mathrm{d}\tilde{y} + \int_0^y \frac{\partial}{\partial x}\left(\overline{u'^2} - \overline{v'^2}\right)\mathrm{d}\tilde{y} \tag{2.3}$$

where τ_w denotes the wall shear stress. For abbreviation we introduce

$$I_\mathrm{cu}(y) = \int_0^y U\frac{\partial U}{\partial x}\mathrm{d}\tilde{y}\,, \quad I_\mathrm{cv}(y) = \int_0^y V\frac{\partial U}{\partial \tilde{y}}\mathrm{d}\tilde{y}\,,$$

$$I_\mathrm{r}(y) = \int_0^y \frac{\partial}{\partial x}\left(\overline{u'^2} - \overline{v'^2}\right)\mathrm{d}\tilde{y} \tag{2.4}$$

to denote the integrated convective term and the Reynolds normal stress term.

2.2 Scaling for the inner layer

The classical scaling based on the friction velocity is

$$u^+ = \frac{U}{u_\tau}\,, \quad y^+ = \frac{y u_\tau}{\nu}\,, \quad \tau^+ = \frac{\tau}{\tau_w}\,, \quad u_\tau = \sqrt{\frac{\tau_w}{\rho}}\,, \quad \Delta p^+ = \frac{\nu}{\rho u_\tau^3}\frac{\mathrm{d}P_\mathrm{w}}{\mathrm{d}x}\,,$$

and the integrated terms defined in (2.4) become

$$I^+_\mathrm{cu}(y^+) = \frac{I_\mathrm{cu}}{u_\tau^2}\,, \quad I^+_\mathrm{cv}(y^+) = \frac{I_\mathrm{cv}}{u_\tau^2}\,, \quad I^+_\mathrm{r}(y^+) = \frac{I_\mathrm{r}}{u_\tau^2}\,.$$

Then the relation for the total shear stress (2.3) becomes in inner viscous units

$$\tau^+ \equiv \frac{\mathrm{d}u^+}{\mathrm{d}y^+} - \overline{u'v'}^+ = 1 + \Delta p_x^+ y^+ + I^+_\mathrm{cu}(y^+) + I^+_\mathrm{cv}(y^+) \;\; + I^+_\mathrm{r}(y^+)\,. \tag{2.5}$$

A second classical scaling based on the so-called pressure-viscosity velocity u_p leads to

$$u^* = \frac{U}{u_p}, \quad y^* = \frac{y u_p}{\nu}, \quad u_p = \left|\frac{\nu}{\rho}\frac{\mathrm{d}P_\mathrm{w}}{\mathrm{d}x}\right|^{1/3}, \quad \Delta p^+ = \left(\frac{u_p}{u_\tau}\right)^3,$$

which was proposed by Mellor [1966], see also Simpson [1983] and Manhart et al. [2008].

2.3 A model for the total shear stress

the data can be can For a model of the total shear stress, we follow the work by Coles [1956], Perry [1966], Galbraith et al. [1977], and van den Berg [1973, 1975]. They use the following ansatz for the mean velocity profile in the inner region

$$U(x,y) = u_\tau(x)\, f(y^+(x,y))\,, \quad y^+(x,y) = \frac{u_\tau(x) y}{\nu}\,. \tag{2.6}$$

Then using the chain-rule for differentiation and invoking the continuity equation they obtain the following model for the mean inertial terms

$$\int_0^y U\frac{\partial U}{\partial x}\mathrm{d}\tilde{y} + \int_0^y V\frac{\partial U}{\partial \tilde{y}}\mathrm{d}\tilde{y} = \nu\frac{\mathrm{d}u_\tau}{\mathrm{d}x}\int_0^{y^+} f^2\mathrm{d}\tilde{y}^+\,. \tag{2.7}$$

By substitution of (2.7) into (2.5) and neglecting $I^+_\mathrm{r}(y^+)$ they obtain the following relation for the total shear stress τ

$$\tau^+(y^+) = 1 + \Delta p_x^+ y^+ + \Delta u^+_{\tau,x} I^+_\mathrm{u}\,, \qquad I^+_\mathrm{u} = \int_0^{y^+} f^2\mathrm{d}\tilde{y}^+\,. \tag{2.8}$$

This reveals that even for the most simple ansatz for a wall-law, viz. (2.6), the total shear stress in the inner layer depends on two non-dimensional parameters, the pressure gradient parameter Δp_x^+ and the wall shear stress gradient parameter $\Delta u_{\tau,x}^+$ defined by

$$\Delta u_{\tau,x}^+ = \frac{\nu}{u_\tau^2}\frac{\mathrm{d}u_\tau}{\mathrm{d}x}\,. \tag{2.9}$$

From (2.8) a linear approximation for the total shear stress can be motivated for small values of $\Delta u_{\tau,x}^+ I_{\mathrm{u}}^+$ compared to $\Delta p_x^+ y^+$. The classical literature, e.g. McDonald [1969], uses the assumption that the effect of mean inertia can be accounted for by writing

$$\tau^+ = 1 + \lambda \Delta p_x^+ y^+\,. \tag{2.10}$$

Therein λ is a constant smaller than one, and $\lambda\Delta p_x^+$ is called the effective pressure gradient, see also Durbin and Belcher [1992]. For flows at a mild adverse pressure gradient near equilibrium, McDonald [1969] proposes $\lambda = 0.7$, and from Perry et al. [1966] a value of $2/2.4 = 0.833$ can be inferred at the outer edge of the logarithmic layer for the flows considered their work. Similar values were found in Knopp et al. [2015].

2.4 Wall laws for the mean velocity at adverse pressure gradients

This section gives a brief survey on wall laws for the mean velocity at adverse pressure gradients which are used in the present work.

2.4.1 A model for the viscous sublayer thickness by T. Nickels

Nickels [2004] proposes an analytical model for the mean velocity in boundary layers subjected to mild and moderately strong pressure gradients, which can be favourable and adverse. Therein the viscous sublayer solution $U_{\mathrm{vis}}^+ = U_{\mathrm{vis}}^+(y^+;\Delta p_x^+, y_c^+)$ is given by

$$U_{\mathrm{vis}}^+ = y_c^+\left[1 - \left[1 + 2\frac{y^+}{y_c^+} + \frac{1}{2}\left(3 - \Delta p_x^+ y_c^+\right)\left(\frac{y^+}{y_c^+}\right)^2 - \frac{3}{2}\Delta p_x^+ y_c^+\left(\frac{y^+}{y_c^+}\right)^3\right] e^{-3\frac{y^+}{y_c^+}}\right] \tag{2.11}$$

which depends on the local value of Δp_x^+ and a parameter y_c^+, which is associated with the thickness of the viscous sublayer. The idea is that the thickness of the viscous sublayer y_c can be determined by a stability argument using a critical value Re_c of a suitably defined local Reynolds number

$$Re_c = \frac{u_T y_c}{\nu}, \qquad u_T = \left(\frac{\tau|_{y=y_c}}{\rho}\right)^{1/2}\,. \tag{2.12}$$

Therein y_c is the critical value of y above which the viscous sublayer becomes unstable. The velocity scale u_T is based on a linear approximation of the total shear stress, neglecting the mean inertial term

$$\tau^+|_{y=y_c} = 1 + \Delta p_x^+ y_c^+ \,. \tag{2.13}$$

The assumption that Re_c has a universal value for all wall-bounded flows implies that y_c satisfies the cubic equation

$$Re_c = \frac{u_T y_c}{\nu} = y_c^+ \sqrt{1 + \Delta p_x^+ y_c^+} \quad \Leftrightarrow \quad \Delta p_x^+ \left(y_c^+\right)^3 + \left(y_c^+\right)^2 - Re_c^2 = 0 \tag{2.14}$$

where Re_c is the only free parameter and is chosen from zero-pressure-gradient data to be $Re_c = 12$. The physically relevant solution for y_c is the smallest positive root of (2.14).

2.4.2 A model for the log-law slope κ by T. Nickels

Regarding the log-law slope, Nickels [2004] argues that two relations to characterise the vorticity scale in the inner layer should be equal. The first relation is based on the velocity scale u_τ and the second is based on u_T. This leads to

$$\frac{\partial U}{\partial y} = \frac{u_T}{\kappa_0 y} = \frac{u_\tau}{\kappa y} \quad \Leftrightarrow \quad \frac{\kappa}{\kappa_0} = \frac{u_\tau}{u_T} \tag{2.15}$$

Therein κ_0 is the log-law slope for the zero pressure gradient case. This implies that

$$\frac{\kappa}{\kappa_0} = \sqrt{\frac{1}{1 + p_x^+ y_c^+}} \tag{2.16}$$

where κ_0 is the only free parameter, for which he chooses $\kappa_0 = 0.39$.

2.4.3 Half-power law

A half-power law (or: square-root law, abbreviated: sqrt-law) is studied in several publications on turbulent boundary layers at adverse pressure gradient. In the present work we write the sqrt-law in the form used by e.g. Skote and Henningson [2002]

$$u^+ = \frac{1}{K_\mathrm{o}} \left[\log(y^+) + 2\left(\sqrt{1 + \Delta p_x^+ y^+} - 1\right) + 2\log\left(\frac{2}{\sqrt{1 + \Delta p_x^+ y^+} + 1}\right)\right] + B_\mathrm{o} \,. \tag{2.17}$$

Then the mean velocity gradient in wall-normal direction is

$$\left(\frac{\mathrm{d}u^+}{\mathrm{d}y^+}\right)_{\mathrm{sqrt,theory}} = \frac{\sqrt{1 + \Delta p_x^+ y^+}}{K_\mathrm{o} y^+} \,. \tag{2.18}$$

2.4.4 Composite form of the mean velocity in the inner layer

The idea of a composite form of the mean velocity profile with a sqrt-law region above the log-law region was proposed by some authors, e.g. Perry [1966], Kader and Yaglom [1978], Telbany and Reynolds [1980]. Then the question arises on the wall distance where the transition from a log-law to the sqrt-law takes place, see e.g., Kader and Yaglom [1978].

2.4.5 Mean velocity slope diagnostic functions

The mean velocity slope diagnostic function is a method to assess the functional behaviour of the mean velocity gradient with more scrutiny, see e.g. Österlund et al. [2000] for zero pressure gradient flows. In the general form the diagnostic function may be written as

$$\xi^{-1} \sim \left(\frac{\mathrm{d}u^+}{\mathrm{d}y^+}\right)^{-1}_{\text{theory}} \left(\frac{\mathrm{d}u^+}{\mathrm{d}y^+}\right)_{\text{data}} . \tag{2.19}$$

The first term on the right hand side is the theoretically assumed mean velocity gradient to be tested and the second term is the actual mean velocity gradient computed from the data. For the log-law the diagnostic function becomes

$$\xi^{-1}_{\text{log}} = y^+ \left(\frac{\mathrm{d}u^+}{\mathrm{d}y^+}\right)_{\text{data}} . \tag{2.20}$$

For the sqrt-law (2.17) the mean velocity slope diagnostic function is

$$\xi^{-1}_{\text{sqrt}} = \frac{y^+}{\sqrt{1 + \Delta p_x^+ y^+}} \left(\frac{\mathrm{d}u^+}{\mathrm{d}y^+}\right)_{\text{data}} . \tag{2.21}$$

A plateau region of the slope diagnostic function can be seen as support for an the assumed (theoretical) behaviour $u^+(y^+)$. For zero pressure gradient turbulent boundary layers, a plateau can be seen only for $Re_\theta \gtrapprox 6000$, see Österlund et al. [2000]. The overlap of inner and outer layer becomes sufficiently thick in terms of y^+ only for asymptotically high *Re*. We expect that a similar *Re* is needed to observe an asymptotic behaviour with a sufficiently thick overlap region at adverse-pressure gradients. This can be reached at the moment only using wind-tunnel experiments.

Chapter 3

Experimental investigation

The aim of the experiment was to answer the following questions for the mean velocity profile at adverse pressure gradients:

(Q1) Does a log-law region still exist at APG?

(Q2) Does the slope of the log-law change with Δp_x^+, as proposed by Nickels [2004]?

(Q3) Is there a sqrt-law region above the log-law, see e.g. Perry et al. [1966]?

The hypothesis by Nickels [2004] of a changing log-law slope led to the first design condition (C1) to reach $\Delta p_x^+ > 0.01$ in the focus region of the APG, so that a possible change of the log-law slope due to the pressure gradient is large enough to be distinguished from uncertainties related to the evaluation of the log-law slope and the determination of u_τ. For this purpose the measurements were performed on the contour geometry model and not on the flat wind tunnel opposite to the model, since the values of Δp_x^+ are significantly larger on the contour model. The second design condition (C2) was to reach large Reynolds numbers in the APG focus region, since we assume that only at large Reynolds numbers the asymptotic structure of a possible wall-law with a significantly thick log-layer and a significantly thick sqrt-law region forms at APG, similar to the observation for the ZPG case, see e.g. Österlund et al. [2000].

Two additional conditions were a consequence of the aim to use the measurement technique as accurate as possible. The third condition (C3) was to use a flat surface in the APG focus region to enable measurements through a glass plate from behind to reduce the issue of reflections of particle imaging methods in the near-wall region. The fourth design condition (C4) was to achieve large Reynolds numbers at moderately low flow speeds and large boundary layer thicknesses to enable accurate measurements in the viscous sublayer. Due to the design condition (C4) in conjunction with the decision to measure on the geometry model, the issue of surface curvature effects arose. We accepted this issue, since the aim to reach at least $\Delta p_x^+ > 0.005$ on the wind tunnel wall side would lead to a much stronger pressure gradient on the geometry model causing the flow to separate. This would mean either to accept a three-dimensional flow with corner separation, whose complexity was described just recently by Simmons et al. [2019], or to use flow actuation to prevent separation with all

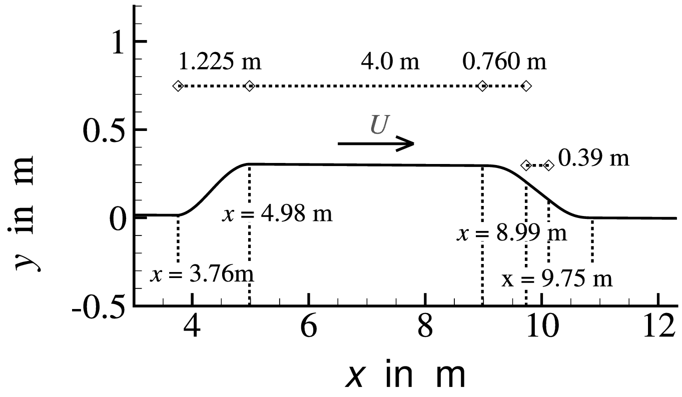

Figure 3.1: Sketch of the wind tunnel experiment with flow direction (axes not to scale).

its technical challenges to reach constant and well-defined flow conditions over the measurement time and reproducible results for different flow experiments.

3.1 Design of the experiment and set-up in the wind tunnel

We performed the experiment in the Eiffel type atmospheric wind tunnel of UniBw in Munich, which has a 22-m-long test section with a rectangular cross section of $2 \times 2\,\mathrm{m}^2$. As described in figure 3.1, the flow develops on the side wall of the wind tunnel over around $4\,\mathrm{m}$ and is then accelerated along a first ramp of height $0.30\,\mathrm{m}$ and of length $1.225\,\mathrm{m}$. Then the flow gradually develops along a flat plate of length $4.0\,\mathrm{m}$ with ZPG into an equilibrium. The flow follows a curvilinear deflection of length $l_c = 0.75\,\mathrm{m}$ which initially causes a small FPG, and enters into the APG region. The focus region is an inclined flat plate of length $0.4\,\mathrm{m}$ at an opening angle of $\alpha = 14.4^\circ$ with respect to the $4.0\,\mathrm{m}$ long flat plate. Finally, the flow follows a second deflection down to the wind tunnel wall. The opening angle was chosen to keep the flow remote from separation in a more conservative way than in the precursor experiment by Knopp et al. [2014] and was designed based on CFD results with the DLR TAU code using the Spalart-Allmaras model and the SST k-ω model.

The coordinate system is shown in figure 3.1. The origin $x = 0$ is defined at the nominal begin of the test section, which is located $0.875\,\mathrm{m}$ downstream of the thinnest cross-section of the contraction. The curvilinear deflection can be described by a fourth order polynomial $f(\zeta)$. Therein ζ denotes the relative coordinate $\zeta = x - 8.99\,\mathrm{m}$, i.e., $\zeta = 0$ at the begin of the curvilinear element and $\zeta = l_c$ at its end. Then the conditions of a smooth transition between the flat plate and the curved wall imply $f'(0) = 0$, $f'(l_c) = a = \arctan(\pi\alpha/180)$ with $\alpha = 14.4^\circ$, and $f''(0) = f''(l_c) = 0$. Therein f' and f'' denote the first and second derivative. This leads to $f(\zeta) = -a/(2l_c^3)\zeta^4 + a/l_c^2\zeta^3$.

The first idea was to remove the initial boundary layer upstream of the ramp by some means of flow actuation and to start with a fresh boundary layer similar

	2D2C PIV	LR-μPTV	3D3C LPT
U_e at x_{ref}	$28.1\,\mathrm{m/s}$	$28.1\,\mathrm{m/s}$	$43.2\,\mathrm{m/s}$
Field of view	$0.44 \times 0.37\,\mathrm{m}^2$	$20 \times 17\,\mathrm{mm}^2$	$50 \times 90 \times 8\,\mathrm{mm}^3$
Resolution	$5.9\,\mathrm{px_{obj}/mm}$	$125\,\mathrm{px_{obj}/mm}$	$35\,\mathrm{px_{obj}/mm}$
Interrogation vol. $l_x \times l_y \times l_z$	$2.7 \times 2.7 \times 1\,\mathrm{mm}^3$	–	–
IW size l_y resp. bin size at x_{ref}	$91\delta_\nu$	$0.27\delta_\nu$	$2.88\delta_\nu$
$\delta_\nu = \nu/u_\tau$ at x_{ref}	$30\,\mu\mathrm{m}$	$30\,\mu\mathrm{m}$	$20\,\mu\mathrm{m}$

Table 3.1: Summary of the experimental parameters. The flow was seeded with DEHS droplets with a diameter of approx. 1μm. The flow parameters are for the reference position $x_{\mathrm{ref}} = 9.944\,\mathrm{m}$.

to the situation on an aircraft wing. The motivation for this was to keep the boundary layer thickness δ_{99} small compared to the radius of curvature R_c to reduce the curvature effects. This idea was abandoned for technical reasons and to ensure a well-defined simple flow for CFD.

The experiments were performed at a free-stream velocity of $U_\infty = 10\,\mathrm{m/s}$, $U_\infty = 23\,\mathrm{m/s}$, and $U_\infty = 36\,\mathrm{m/s}$ which was measured at a reference position upstream of the contour. This yields $Re_\theta = 8400$, 16000, and 23000 at $x = 8.36\,\mathrm{m}$ in the ZPG region and $Re_\theta = 15000$, 28000, and 41000 at $x = 9.94\,\mathrm{m}$ in the APG region. In order to reduce the effects of the side walls, the dimension of the APG part of the geometry was reduced by a factor of two compared to the previous experiment by Knopp et al. [2014].

3.2 Measurement technique

3.2.1 Large-scale 2D2C particle image velocimetry

We combined different particle imaging approaches in order to match the requirement of measuring the mean velocity and the Reynolds stresses over a streamwise extent of several boundary layer thicknesses from the outer edge of the boundary layer down to the viscous sublayer. For an overview measurement from $x = 8\,\mathrm{m}$ to $x = 10.2\,\mathrm{m}$ we applied a multi-camera large-scale 2D2C-PIV measurement using 9 cameras named c1 to c9 in the following. The cameras c1 to c7 were located in the region of ZPG, FPG and mild APG, whereas the cameras c8 and c9 were located in the region of the largest APG. The 2D2C-PIV data were evaluated using a single-pixel ensemble correlation and a window correlation method, see Reuther et al. [2015]. The interrogation window (IW) size was $16 \times 16\,\mathrm{px}^2$ and the interrogation step size was 8 px, corresponding to an overlap of 50%. From the 2D2C-PIV data, the mean velocity profiles where extracted at 13 selected streamwise positions. Details of the PIV method are given in table 3.1.

The spatial resolution of the PIV method depends mainly on the magnification of the imaging system, the pixel size of the recording cameras and the selected interrogation window dimensions, see Kähler et al. [2012a]. To locally capture the entire boundary layer, the nine sCMOS cameras were equipped with

50 mm Zeiss lenses (c1-c7) and 35 mm Zeiss lenses (c8-c9), respectively, where the boundary layer thickness increases significantly due to the present adverse pressure gradient. In the regions of ZPG, FPG and mild APG, the field of view was $0.32 \times 0.27\,\mathrm{m}^2$ and the interrogation volume size was $2 \times 2 \times 1\mathrm{mm}^3$ yielding a resolution of $8\mathrm{px}_{\mathrm{obj}}/\mathrm{mm}$ for cameras c1 to c7. Regarding the resolution in viscous units δ_ν, we consider the position at $x = 8.12\,\mathrm{m}$. We obtain for the interrogation window size $l_y^+ = 125$ based on $\delta_\nu = \nu/u_\tau = 16\,\mu\mathrm{m}$ for $U_\infty = 23\,\mathrm{m/s}$, and $l_y^+ = 57$ based on $\nu/u_\tau = 35\,\mu\mathrm{m}$ for $U_\infty = 10\,\mathrm{m/s}$. In the APG region the field of view was $0.44 \times 0.37\,\mathrm{m}^2$ and the interrogation volume $l_x \times l_y \times l_z$ was $2.7 \times 2.7 \times 1\,\mathrm{mm}^3$. This yields an interrogation window size in wall-normal direction of $l_y^+ = 91$ for camera c8 at $x_{\mathrm{ref}} = 9.944\,\mathrm{m}$.

3.2.2 Particle tracking velocimetry

To resolve the near wall region, a high magnification approach using long-range microscopic particle tracking velocimetry (2D-μPTV), see Kähler et al. [2006], Kähler et al. [2012b], Cierpka et al. [2013], was applied at the position $x_{\mathrm{ref}} = 9.944\,\mathrm{m}$ in the APG region, which gives a 2D2C data field. The wall normal extent of the field of view was $140\delta_\nu$ for the case $U_\infty = 23\,\mathrm{m/s}$. The size of a bin in wall-normal direction was $0.27\delta_\nu$.

Additionally the 3D Lagrangian particle tracking (LPT) approach using the Shake-The-Box (STB) method was used, which gives a 3D3C data field. This technique was applied here in a multi-pulse acquisition strategy. For details we refer to Novara et al. [2016]. The macroscopic field of view of $50 \times 90 \times 8\,\mathrm{mm}^3$ covered approximately $0.4\delta_{99}$. In this work we use the data which were sampled over a bin size of $2.88\delta_\nu$ in wall-normal direction. This evaluation will be referred to as LPT detail. The LPT data provide an very good resolution of all components of the Reynolds stresses.

For a study of the terms of the mean momentum equation, a second evaluation of the data was performed. The field of view was divided into 111 bins in wall-normal direction and 5 bins in wall-parallel direction, corresponding to a bin size of $321 \times 30\,\mathrm{px}^2$ (or: $9.2 \times 0.86\,\mathrm{mm}^2$) in streamwise and wall-normal direction. The gradients are evaluated using a linear interpolation over a kernel of 5 points located in the center of each bin. The choice of the large bin size in streamwise direction was motivated by statistical convergence reasons, as more than 400000 entries per bin are available to estimate the mean and fluctuating velocity components. Since the bin size in wall-normal direction corresponds to around $41\delta_\nu$, this evaluation will be referred to as LPT average (abbreviated: LPT ave).

3.2.3 Oil film interferometry

The wall shear stress was measured using oil film interferometry (OFI) in the region of interest from $x = 8.33\,\mathrm{m}$ to $x = 10.02\,\mathrm{m}$. This provides absolute measurements of the wall shear stress independent of any assumption on the mean velocity profile. For technical details of the oil film interferometry measurements we refer to Schülein et al. [2017].

U_∞ m/s	x m	U_e m/s	Re_θ	Re_τ	δ_{99} mm	δ_{995} mm	δ^* mm	θ mm	H_{12}	u_τ m/s	Δp_x^+	β_RC
10	8.120	11.81	12920	4133	145.3	166.1	18.07	13.99	1.292	0.430	-0.00058	-0.300
10	9.944	10.75	16015	2835	195.5	211.6	37.78	23.59	1.601	0.219	0.0436	24.07
23	8.120	28.13	24358	9304	147.6	161.0	16.78	13.43	1.250	0.977	-0.00015	-0.156
23	9.944	25.50	39783	6939	203.7	215.5	37.01	24.19	1.530	0.528	0.0185	27.10
36	8.120	43.29	35908	13214	142.2	157.2	16.06	12.88	1.247	1.443	-0.00011	-0.167
36	9.944	39.18	57363	9799	192.9	206.9	34.54	22.73	1.520	0.789	0.0141	26.36

Table 3.2: Characteristic boundary layer parameters for the 2D2C PIV measurements evaluated by the PIV single-pixel ensemble correlation method.

3.3 Flow conditions

The experiment was performed for three different reference velocities $U_\infty = 10\,\mathrm{m/s}$, $U_\infty = 23\,\mathrm{m/s}$, and $U_\infty = 36\,\mathrm{m/s}$. The reference velocity U_∞ was measured near $x = 0$ little downstream of the nozzle at the beginning of the test section at a distance of 0.30 m above the wind-tunnel wall. The measurements using the different measurement techniques were performed at different days, nominally for the same values of U_∞. The PIV measurements were performed during two consecutive weeks at very similar ambient conditions. The OFI measurement campaign was performed some months later at little larger values for ν by around 10% compared to the PIV measurement campaign. Details of the flow conditions in the wind tunnel are summarised in table A.1 in appendix A.

The characteristic boundary layer parameters are given in table 3.2. They are based on the 2D2C PIV measurements evaluated by the single-pixel method. The values should be seen only as approximate values. The boundary layer thicknesses δ_{99} and δ_{995} are determined as the wall distance where the mean velocity reaches 99 % and 99.5 % of its maximum value along a wall-normal line. In the present work the focus is on the inner part of the boundary layer, and therefore the method used is considered to be sufficient to characterise the flow conditions. In the focus region, the mean velocity profiles near the boundary layer edge do not show the more difficult situations which can occur for the flow around airfoils, see, e.g., Vinuesa et al. [2016], Knopp and Probst [2013], and Probst et al. [2011]. For the determination of the length scale to characterise the outer boundary layer, more sophisticated methods are needed for the boundary layer edge and the turbulent/non-turbulent interface, see, e.g., Chauhan et al. [2014b,a], Vinuesa et al. [2016], Reuther and Kähler [2018, 2019].

We remark that the mean velocity profiles obtained by the single-pixel ensemble correlation method and the window correlation method show small deviations near the boundary layer edge, leading to a small deviation in δ_{995}. The parameters are given for two streamwise positions, namely, at $x = 8.12\,\mathrm{m}$ where the flow is almost at ZPG, and at $x = 9.944\,\mathrm{m}$ in the APG region. The boundary layer thicknesses δ_{99} and δ_{995} are decreasing with increasing Re for $U_\infty = 23\,\mathrm{m/s}$ and $U_\infty = 36\,\mathrm{m/s}$. However, for the case $U_\infty = 10\,\mathrm{m/s}$ the boundary layer thickness is slightly thinner than expected.

Chapter 4

Characterisation of the streamwise flow evolution

In this section we describe of the streamwise evolution of the flow. The goal is to characterise the pressure gradient and the effects of surface curvature.

4.1 Characterisation of pressure gradient and curvature

The characterisation of the effects of an adverse pressure pressure gradient is still not clear in the literature, as pointed out in section 2. For the characterisation of the pressure gradient in the inner part of the boundary layer, we show Δp_x^+ in figure 4.1 (a). The pressure gradient in Clauser-Rotta scaling

$$\beta_{\mathrm{RC}} = \frac{\delta^*}{\rho u_\tau^2} \frac{\mathrm{d}P_{\mathrm{w}}}{\mathrm{d}x} \tag{4.1}$$

shows a very similar distribution as Δp_x^+, see figure 4.1 (b). Both become largest in the region where u_τ becomes smallest. This appears in the APG region on the inclined flat plate. We included RANS results using the SSG/LRR-ω model, see Eisfeld et al. [2016]. The pressure gradient parameter in Zagarola-Smits scaling β_{ZS}, see Zagarola and Smits [1997], Gungor et al. [2014], is shown in figure 4.2 (a), and does not involve the friction velocity

$$\beta_{\mathrm{ZS}} = \frac{\delta_{99}^2}{\rho U_e^2 \delta^*} \frac{\mathrm{d}P_{\mathrm{w}}}{\mathrm{d}x} \tag{4.2}$$

Downstream of the ZPG region, β_{ZS} shows significant negative values for the favourable pressure gradient near $x = 9.05\,\mathrm{m}$, then changes its sign and reaches large positive values with a maximum near $x = 9.62\,\mathrm{m}$ where a significant adverse pressure gradient is reached.

The streamwise distance over which the pressure gradient changes may be compared to the boundary layer reference thickness, which is $\delta_{99,\mathrm{ref}} = 0.15\,\mathrm{m}$ at $x = 8.12\,\mathrm{m}$. The curvature first causes an FPG from $x = 8.85\,\mathrm{m}$ to $x = 9.24\,\mathrm{m}$ over a streamwise length of $2.6\delta_{99,\mathrm{ref}}$. The change of β_{ZS} from a significant FPG

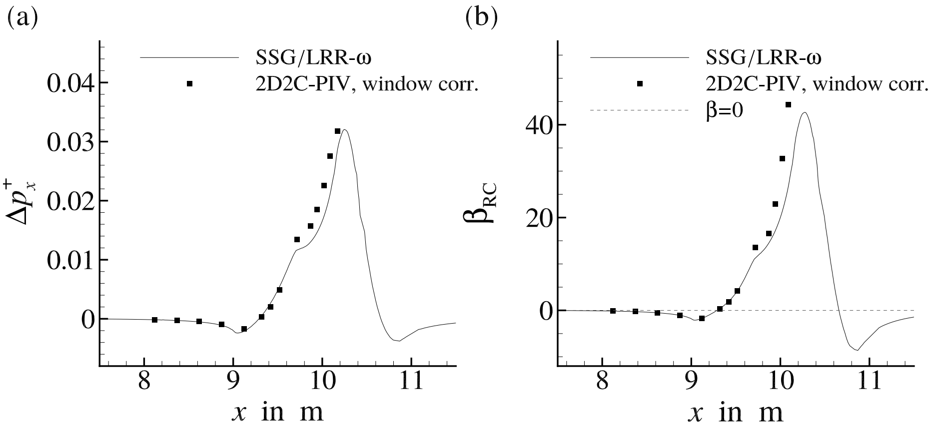

Figure 4.1: Streamwise pressure gradient parameter for $U_\infty = 23\,\mathrm{m/s}$ (a) in inner scaling and (b) in Clauser-Rotta scaling.

to a significant APG from $x = 9.05\,\mathrm{m}$ to $x \leq 9.62\,\mathrm{m}$ corresponds to $4\delta_{99,\mathrm{ref}}$. In the APG region on the inclined flat plate for $x > 9.75\,\mathrm{m}$, the curvature is absent and β_{ZS} is slowly decreasing in streamwise direction. The focus measurement position at $x = 9.944\,\mathrm{m}$ in the APG region is located $1.3\delta_{99,\mathrm{ref}}$ downstream of the end of curvature.

The convex curvature of the geometry and the resulting mean-streamline curvature is expected to have a significant influence on the flow. The ratio of the local boundary layer thickness δ_{99} to the local radius of curvature R_c is shown in figure 4.2 (b). The values for δ_{99}/R_c are larger than the value of 0.01 which is associated with mild curvature in the literature. We note that the value given in Knopp et al. [2017] was too low due to an unfortunate error in the calculation. On the other hand, the value for δ^*/R_c is smaller than 0.005, which is lower by one order of magnitude than the criterion by Bradshaw [1970] to characterise strong curvature.

At the junction between the flat wall and the curvilinear wall, the surface is smooth, but the change in curvature needs to be quantified. Baskaran et al. [1987] and Bandyopadhyay and Ahmed [1993] describe that an abrupt change in surface curvature can initiate the growth of an internal boundary layer. Baskaran et al. [1987] characterise the strength of the perturbation in curvature using the parameter $\Delta k^* = \Delta k \nu / u_\tau$ for a step change of R_c with $\Delta k = R_{c,2}^{-1} - R_{c,1}^{-1}$. Since $\Delta k = 0$ at the junction, we assess the change Δk over a streamwise distance Δs of one inner layer thickness, i.e., $\Delta s = 0.15\,\delta_{99}$. We obtain $\Delta k^* \approx 6.7 \times 10^{-7}$ at the begin of curvature at $x = 8.99\,\mathrm{m}$ and $\Delta k^* \approx 1.0 \times 10^{-6}$ at the end of curvature at $x = 9.75\,\mathrm{m}$, both of which are smaller than the threshold value of $\Delta k^* \approx 3.7 \times 10^{-5}$ reported by Bandyopadhyay and Ahmed [1993] to initiate an internal layer.

The present flow is thus subjected to convex curvature effects and relaxation on a flat wall in conjunction with a streamwise changing pressure gradient from favourable to adverse. The focus region begins at the reference stations $x = 8.12\,\mathrm{m}$ and $x = 8.37\,\mathrm{m}$ with a fully developed turbulent boundary layer profile at almost zero pressure gradient, although the flow still shows history effects

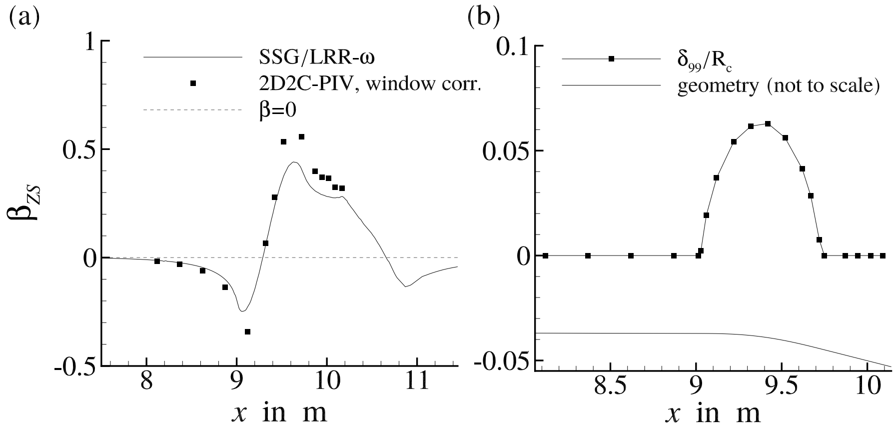

Figure 4.2: (a) Streamwise pressure gradient for $U_\infty = 23\,\mathrm{m/s}$ in the scaling by Zagarola & Smits (b) δ_{99}/R_c.

due to the accelerating ramp. Then the turbulent boundary layer first enters a region of convex surface curvature at a favourable pressure gradient, then convex curvature at a changing pressure gradient from favourable to adverse, followed by convex curvature at an adverse pressure gradient and then relaxation from convex curvature on a flat wall at an adverse pressure gradient.

4.2 Concave curvature ramp and longitudinal vortices

Before we can proceed with the results, an important detail on the flow needs to be described. Upstream of the 4 m long flat plate and the focus region, the flow follows a first ramp, where it experiences a concave surface curvature in conjunction with a significant favourable pressure gradient. During the evaluation of the data, some indications arose that the concave curvature could cause the generation of longitudinal vortices, similar to Görtler vortices. A first indication came from the OFI measurements showing a spanwise variation of c_f, see Schülein et al. [2017] with a wavelength in the range 0.10 m to 0.14 m. Moreover we observed a deviation in u_τ between the OFI results and the Clauser chart method at $x = 8.37\,\mathrm{m}$ for the cases $U_\infty = 10\,\mathrm{m/s}$ and $U_\infty = 36\,\mathrm{m/s}$, whereas the agreement was very close for the case $U_\infty = 23\,\mathrm{m/s}$. The second indication were 2D2C measurements in wall parallel planes at different wall-distances, showing small but noticeable spanwise variations of the mean flow, as reported in a personal communication by Eich [2017]. A simple empirical model for Görtler vortices yields a wavelength which is similar to the observed values, which is described in appendix F.

The spanwise position of the longitudinal vortices is different for $U_\infty = 10\,\mathrm{m/s}$, $U_\infty = 23\,\mathrm{m/s}$, and $U_\infty = 36\,\mathrm{m/s}$. The longitudinal vortices seem to meander in streamwise direction. For $U_\infty = 23\,\mathrm{m/s}$, the vortex travels outside of the plane of the present PIV measurements and does not cross this plane. However, for $U_\infty = 10\,\mathrm{m/s}$ and for $U_\infty = 36\,\mathrm{m/s}$, the position of the longitudinal vortex is located closer to the measurement plane, and for $U_\infty = 10\,\mathrm{m/s}$ the longitudinal vortex could cross the measurement plane at some measurement positions. Although time-resolved PIV measurements could not be performed, the PIV data in wall-parallel planes indicate a small unsteadiness in the meandering of the longitudinal vortex, in particular for $U_\infty = 10\,\mathrm{m/s}$. As a conclusion, we will focus on the cases $U_\infty = 23\,\mathrm{m/s}$ and $U_\infty = 36\,\mathrm{m/s}$. For the latter case, we do not use the OFI results, but instead we determine u_τ from the mean velocity.

For the standard statistical averaging procedure for the Reynolds stresses, the presence of the longitudinal vortex in the measurement plane is expected to cause a small increase in the Reynolds stresses. This increase is assumed mainly in the outer part of the boundary layer.

Chapter 5

Results for the zero pressure gradient region

First we consider the mean velocity profile at the long flat plate section, before the flow enters the region of curvature and adverse pressure gradient. The result for $x = 8.12\,\mathrm{m}$ at almost zero pressure gradient is shown in figure 5.1. As a reference, we include the experimental data for a turbulent boundary layer flow at zero pressure gradient for a similar value of Re_τ and for a similar value of Re_θ by Marusic et al. [2015]. Moreover we include the composite law of the wall by Coles with $\eta = y/\delta_{98}$ and $\Pi = 0.45$ in the form

$$u^+ = \frac{1}{0.41}\log(y^+) + 5.0 + \frac{2\Pi}{0.41}\left(\sin\left(\frac{\Pi\eta}{2}\right)\right)^2$$

We observe that the wake of the present data is less pronounced than for the reference data. We suppose that this is a long-living history effect caused by the prior history of the flow, i.e., the flow acceleration over the ramp. In the log-law region, the present data are close to the reference data. The small differences are supposed to be due to the small favourable pressure gradient and due to details in the method to determine u_τ. For the present data, the wall shear stress was determined using a Clauser chart method (CCM) and using oil-film interferometry. For the Clauser chart, we used (i) $\kappa = 0.41$ and $B = 5.0$, (ii) $\kappa = 0.384$ and $B = 4.17$, and (iii) $\kappa = 0.395$ and $B = 4.475$. The value for u_τ is computed by a least-squares fit of the experimental data to the log-law (1.1) in different intervals $y^+_{\mathrm{log,min}} < y^+ < y^+_{\mathrm{log,max}}$, which are specified in table 5.1. In figure 5.1 we use method (i) for scaling the present data. For the reference data, u_τ was determined using a composite velocity profile, as described in Marusic et al. [2015].

Then we determine κ and B by a least squares fit of the data to the log-law (1.1) using the value obtained for u_τ. The results are given in table 5.1. For a statistical evaluation for u_τ and κ, we vary $y^+_{\mathrm{log,min}}$ and $y_{\mathrm{log,max}}/\delta_{995}$ within the intervals summarised in table 5.1. Therein δ_{995} denotes the wall-distance where $U = 0.995U_e$, with U_e being the boundary layer edge velocity. We remark that for the 2C2C PIV data using the window correlation method, the first reliable data point is for $y^+ = 300$. For the computation of δ^* and θ, we use a composite method, i.e., we use the mean-velocity profile by Chauhan et al. [2007] for y^+-

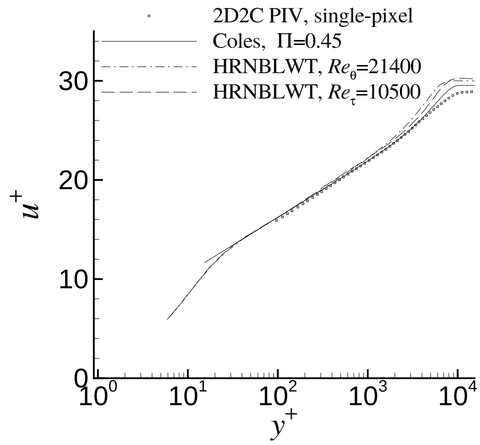

Figure 5.1: Mean velocity profile for $U_\infty = 23\,\mathrm{m/s}$ at $x = 8.12\,\mathrm{m}$ in the region of almost zero pressure gradient and comparison with reference data for a turbulent boundary layer at zero pressure gradient for a similar value of Re_τ and Re_θ by Marusic et al. [2015].

U_∞ m/s	PIV techn.	Method for c_f	$10^4 \Delta p_x^+$	$y^+_{\mathrm{log,min}}$-interval	$y_{\mathrm{log,max}}/\delta_{995}$-interval	u_τ m/s	κ
23	single px.	OFI	-1.5	$[100, 800]$	$[0.1, 0.15]$	0.9774	0.3905
23	single px.	CCM	-1.5	$[100, 800]$	$[0.1, 0.15]$	0.9681	0.3868
23	wind. corr.	CCM	-1.5	$[300, 800]$	$[0.1, 0.15]$	0.9627	0.3987
36	single px.	CCM	-1.1	$[100, 800]$	$[0.1, 0.15]$	1.4327	0.3916
36	wind. corr.	CCM	-1.1	$[500, 800]$	$[0.1, 0.15]$	1.4270	0.4007

Table 5.1: Statistical evaluation of u_τ and κ at almost zero pressure gradient at $x = 8.12\,\mathrm{m}$ by variation of lower bound $y^+_{\mathrm{log,min}}$ and upper bound $y_{\mathrm{log,max}}/\delta_{995}$ assumed for the log-law region.

values below the first reliable data point and the experimental data are used above.

The shape factor H_{12} and the skin friction coefficient c_f evaluated at $x = 8.12\,\mathrm{m}$ are shown in figure 5.2. For comparison we include the hot-wire and Pitot tube reference data by Bailey et al. [2013] and Marusic et al. [2015], measured in the HRNBLWT and in the minimum turbulence level wind tunnel (MTL) at the Royal Institute of Technology (KTH). For the present flow, the value for H_{12} is smaller than for the reference data, which can be explained by the smaller wake factor. On the other hand, the value for c_f at $x = 8.12\,\mathrm{m}$ is larger than for the reference data at zero pressure gradient. From these observations, we draw the conclusion that the history effects of the flow acceleration along the first ramp are still visible in the outer layer at $x = 8.12\,\mathrm{m}$, despite the $4.0\,\mathrm{m}$ long flat plate downstream of the first ramp. The inner layer follows the log-law in good agreement with the reference data.

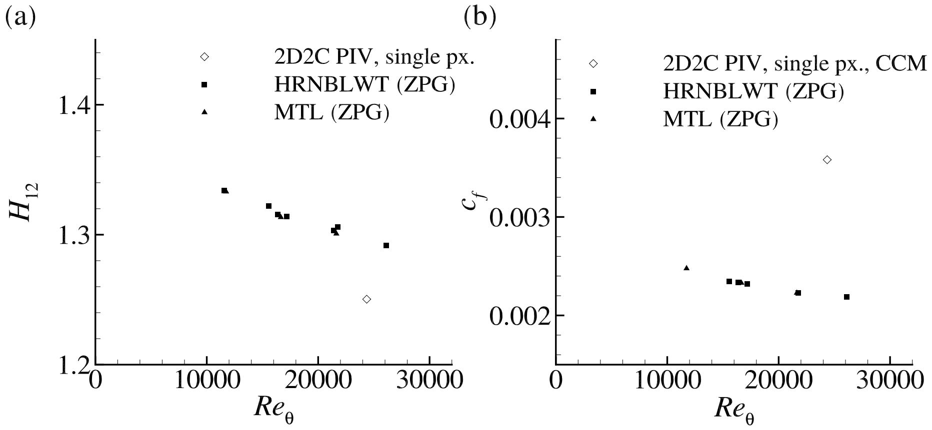

Figure 5.2: (a) Shape factor H_{12} and (b) skin friction coefficient c_f for $U_\infty = 23\,\mathrm{m/s}$ at $x = 8.12\,\mathrm{m}$ and comparison with reference data for the turbulent boundary layer at zero pressure gradient from Bailey et al. [2013] and Marusic et al. [2015].

Chapter 6

Experimental results for the adverse pressure gradient region

The goal of this section is to find an empirical description for the mean velocity profile in the inner layer in the adverse pressure gradient region based on the experimental data. As we use the classical inner scaling, special care is needed for the determination of the friction velocity. We consider the results for the mean velocity in the adverse pressure gradient region, at the detail measurement position $x_{\text{ref}} = 9.944\,\text{m}$ in the middle of the inclined flat plate, which is around $1.14\delta_{99}$ downstream of the end of the curvilinear deflection. We study the results for two Reynolds numbers, i.e., for the onflow velocities $U_\infty = 23\,\text{m/s}$ and $U_\infty = 36\,\text{m/s}$.

6.1 Determination of the wall shear stress

Accurate values for u_τ are needed to investigate wall-laws with a scaling involving u_τ. We use oil film interferometry to determine u_τ without any assumption on the mean velocity profile. Additionally we attempt to determine the wall shear stress from the mean velocity profiles. By definition of the wall shear stress τ_{w}, this requires the evaluation of the mean velocity gradient in wall-normal direction at the wall

$$\frac{\tau_{\text{w}}}{\rho} = u_\tau^2 = \sqrt{\nu \frac{\partial U}{\partial y}\bigg|_{\text{w}}} \tag{6.1}$$

The implications of this definition in terms of resolution requirements for measurements are still open for flows at a significant APG. At high Re, several accurate measurement points below $y^+ = 2$ or even below $y^+ = 1$ are very hard to obtain. For the present experiment, the data points below $y^+ = 2$ are not considered reliable enough, even for the μPTV technique applied here. We note that in a later measurement campaign proper measurements for $y^+ < 2$ could be achieved on the same model for the case $U = 10\,\text{m/s}$, see Bross et al. [2019].

As a remedy we apply different indirect methods. These methods use a fit of the data to an assumed mean velocity profile in a certain y^+-region.

6.2 Mean velocity profiles in the viscous sublayer

For the case $U_\infty = 23\,\mathrm{m/s}$, the μPTV data for the mean velocity are considered to be reliable for $y^+ > 2$. We determine u_τ by a least-squares fit of the data to the relation $u^+ = y^+$ in the region $y^+ \in [2 \pm 0.1; 4.6 \pm 0.6]$. This region was found by a visual comparison of the data with the curve $u^+ = y^+$ and by an inspection of $\partial U/\partial y$. The upper bound is little lower than the value of $y^+ < 5$ used by Nagano et al. [1991]. The statistics are obtained by a variation of the lower and upper bound of the y^+-interval. We obtain $u_\tau = 0.5217 \pm 0.0230\,\mathrm{m/s}$. The estimation of the relative uncertainty of 4.4% is described in C.1. For comparison, OFI yields $u_\tau = 0.5281 \pm 0.0106\,\mathrm{m/s}$. The deviation from the OFI result is around 1%. The mean velocity profiles are shown in figure 6.1, where the inner scaling uses u_τ from OFI (a) and from the fit $u^+ = y^+$ (b).

The detailed behaviour of the mean velocity profile in the viscous sublayer is studied next. The second order Taylor-series expansion $u^+ = y^+ + \frac{1}{2}\Delta p_x^+ (y^+)^2$ is also shown in figure 6.1. The importance of the fourth-order and higher-order terms for $y^+ > 3$ can be clearly seen, as described by Nickels [2004]. On the other hand, for $y^+ < 3$ the number of data points is not sufficient to show an advantage of the second-order approximation. The mean velocity profile (2.11) for the viscous sublayer by Nickels [2004] is also included. This profile depends on Δp_x^+ as a parameter. Interestingly, this profile follows the μPTV data very closely up to $y^+ = 20$. The mean velocity profile for a turbulent boundary layer at ZPG is also included. We use the DNS data by Schlatter and Örlü [2010]. The ZPG data are close to the APG data near the wall, and the deviation increases for $y^+ > 10$, where the APG profile turns below the ZPG profile. This downward turn can be described by the profile by Nickels.

For the case $U_\infty = 36\,\mathrm{m/s}$, we use the 3D LPT data with an evaluation which gives the first reliable data point at $y^+ = 5$. The OFI data are not used due to the possible effects of longitudinal vortices described in section 4.2. First we determine u_τ using a standard Clauser chart method. Then we used an empirical correction for APG to improve the result. The correction is motivated from the difference found between the Clauser chart method and the direct method for u_τ for the μPTV data at $U_\infty = 23\,\mathrm{m/s}$. The method is described in appendix D and is given by equation (D.1). Alternatively we determine u_τ by a least squares fit of the data to the profile by Nickels [2004] for $y^+ < 21$, motivated by the findings for the μPTV data at $U_\infty = 23\,\mathrm{m/s}$. The results for u_τ are shown in table 6.2. The two latter methods have a relative deviation of 1%.

6.3 On the log-law at adverse pressure gradients

In this subsection we study the question of "the resilience of the logarithmic law to pressure gradients", to use the words by Johnstone et al. [2010], for the present flow. In the case of a significant pressure gradient, we write the log-law

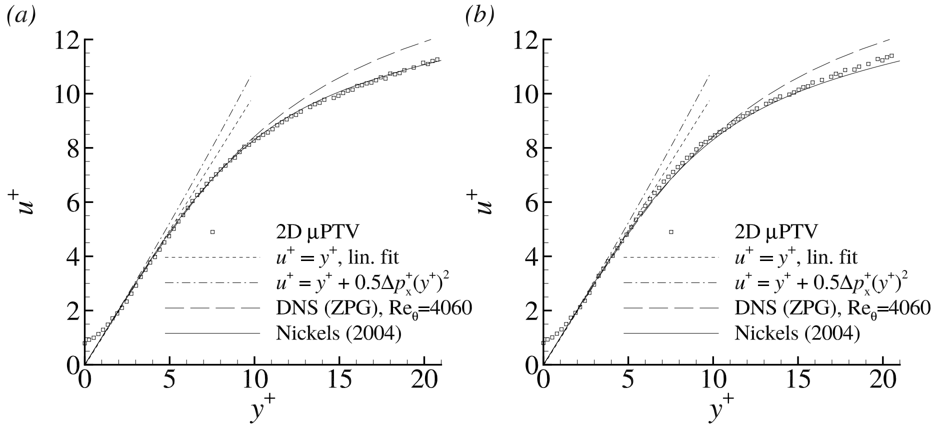

Figure 6.1: 2D μPTV data for $U_\infty = 23\,\mathrm{m/s}$: Mean velocity profile in the viscous sublayer in inner units using u_τ (a) from OFI and (b) from a linear fit to $u^+ = y^+$.

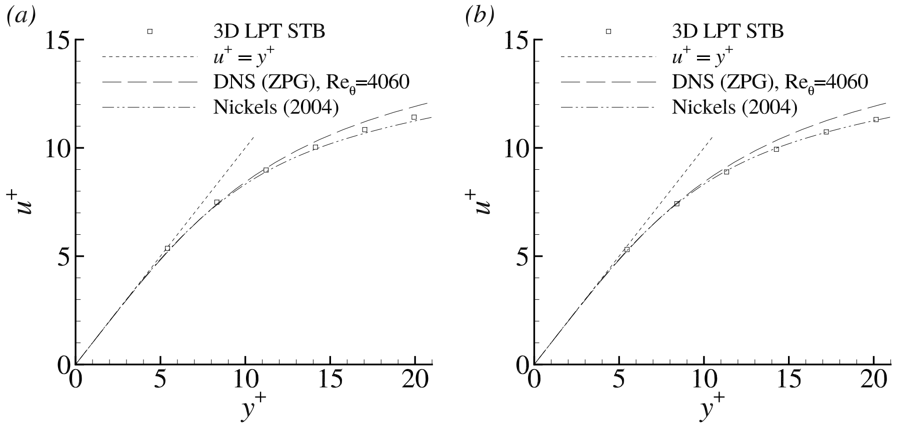

Figure 6.2: $U_\infty = 36\,\mathrm{m/s}$. Mean velocity profile in the viscous sublayer in inner units using u_τ (a) from the corrected Clauser chart described in appendix D and (b) from a least-squares fit to the mean velocity profile by Nickels [2004].

Method for u_τ	u_τ in m/s	ϵ_{u_τ} in %	$100\Delta p_x^+$	$\epsilon_{\Delta p_x^+}$ in %	K_i	ϵ_{K_i} in %
OFI	0.5281 ± 0.0106	2.0	1.826 ± 0.219	12.0	0.3703 ± 0.0167	4.5
Fit $u^+ = y^+$	0.5217 ± 0.0230	4.4	1.894 ± 0.364	19.2	0.3659 ± 0.0252	6.9
Fit to Nickels [2004]	0.5270 ± 0.0200	3.8	1.837 ± 0.320	17.4	0.3697 ± 0.0233	6.3
CCM	0.5037 ± 0.0307	6.1	2.104 ± 0.512	24.3	0.3530 ± 0.0304	8.6

Table 6.1: $U_\infty = 23\,\mathrm{m/s}$: Results for u_τ using different methods and evaluation of K_i for the log-law slope at APG from the μPTV data.

using the notation

$$u^+ = \frac{1}{K_\mathrm{i}} \log(y^+) + B_\mathrm{i} \tag{6.2}$$

and we write K_i and B_i instead of κ and B. At the detail measurement position, the pressure gradient parameter Δp_x^+ is around 0.0185 for the case $U_\infty = 23\,\mathrm{m/s}$ and 0.0115 for the case $U_\infty = 36\,\mathrm{m/s}$. In both cases, we observe a region where the mean velocity profile can be fitted by a log-law by visual inspection of the plot u^+ versus $\log(y^+)$. In order to identify such a region and its extent, we consider the mean velocity slope diagnostic function (2.20) for the log-law. For the case $U_\infty = 36\,\mathrm{m/s}$, we find an indication for a plateau in the region $84 < y^+ < 152$, which is shown in figure B.1 in appendix B. For the case $U_\infty = 23\,\mathrm{m/s}$ we find an indication for a plateau in the region $86 < y^+ < 135$, albeit the result is less clear than for the case $U_\infty = 36\,\mathrm{m/s}$, see appendix B.

Then we evaluate the log-law slope coefficient K_i. First we consider the case $U_\infty = 23\,\mathrm{m/s}$. We determine K_i using a log-linear regression in a y^+-region with lower bound $y^+_{\mathrm{log,min}} \in [82; 92]$ and upper bound $y^+_{\mathrm{log,max}} \in [126; 138]$. The y^+-range is motivated from the slope diagnostic function. The results are given in table 6.1. We obtain $\kappa = 0.370 \pm 0.017$ for the case that u_τ from OFI is used. Beyond the bounds of the y^+-range, the values obtained for K_i change significantly due to the systematic deviation of the mean velocity profile from a log-linear behaviour, in particular for y^+ much larger than 140. The result for the log-law fit is shown in figure 6.3 (a). The discussion of the uncertainties can be found in appendix C.2 and the estimated uncertainties are summarised in table C.4.

For the case $U_\infty = 36\,\mathrm{m/s}$, the log-linear regression is applied in a y^+-region with $y^+_{\mathrm{log,min}} \in [82; 90]$ and $y^+_{\mathrm{log,max}} \in [142; 150]$. We obtain $\kappa = 0.379 \pm 0.020$ for the case that u_τ is determined by the least-squares fit to the profile by Nickels. The detailed results are given in table 6.2. The mean velocity profile and the log-law fit are shown in figure 6.3 (b). A detailed discussion of the uncertainties and their quantification is given again in appendix C.2. The results are summarised in table C.5.

6.4 Clauser chart method

We use the above results to review the Clauser chart method to determine u_τ at adverse pressure gradients. First we consider the case $U_\infty = 23\,\mathrm{m/s}$.

Method for u_τ	u_τ in m/s	ϵ_{u_τ} in %	$100\Delta p_x^+$	$\epsilon_{\Delta p_x^+}$ in %	K_i	ϵ_{K_i} in %
CCM	0.7710 ± 0.0431	5.6	1.253 ± 0.287	22.8	0.3696 ± 0.0251	6.8
CCM + corr. (v1)	0.7964 ± 0.0446	5.6	1.137 ± 0.259	22.8	0.3804 ± 0.0259	6.8
CCM + corr. (v2)	0.7885 ± 0.0441	5.6	1.171 ± 0.269	22.8	0.3765 ± 0.0256	6.8
Fit to Nickels [2004]	0.7946 ± 0.0318	4.0	1.144 ± 0.206	18.0	0.3794 ± 0.0197	5.2

Table 6.2: $U_\infty = 36\,\mathrm{m/s}$: Results for u_τ using different methods and evaluation of u_τ and K_i for the log-law slope at APG for the 3D LPT data.

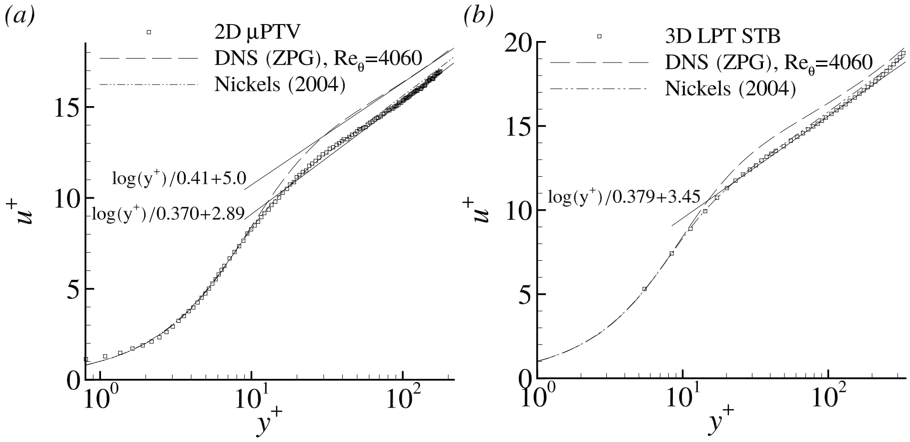

Figure 6.3: Mean velocity profile and least-squares fit in the log-law region (a) for $U_\infty = 23\,\mathrm{m/s}$ using u_τ from OFI and (b) for $U_\infty = 36\,\mathrm{m/s}$ using u_τ from a least-squares fit to the profile by Nickels [2004] for $y^+ < 20$.

The Clauser chart is applied in the identified log-law region, and a variation of $y^+_{\mathrm{log,min}} \in [82; 92]$ and $y^+_{\mathrm{log,max}} \in [126; 138]$ is used for a statistical evaluation. We find $u_\tau = 0.5037\,\mathrm{m/s}$ for $\kappa = 0.41$ and $B = 5.0$ and $u_\tau = 0.5051\,\mathrm{m/s}$ for $\kappa = 0.384$ and $B = 4.17$. Therefore the sensitivity of u_τ on the values for κ and B calibrated for zero pressure gradient flows appears to be small, given the upper and lower bounds for the assumed log-law region are held constant. The values for u_τ determined by the Clauser chart are systematically lower than the value determined from OFI and from the viscous sublayer fit. This finding is in agreement with the results in Monty et al. [2011]. The discussion of the uncertainties is described in table C.6 in appendix C.3.

Then we consider a modified Clauser chart where we use $\kappa = K_\mathrm{i}$ and $B = B_\mathrm{i}$ found from the linear regression with u_τ from OFI. In this case the Clauser chart yields the same value for u_τ as obtained by OFI. Therefore we can conclude that a reliable Clauser chart method for significant adverse pressure gradients needs a method to know K_i and B_i depending on the local flow conditions. This finding will be studied in more detail in the next subsection.

Then we consider the case $U_\infty = 36\,\mathrm{m/s}$. The Clauser chart is applied in the region $y^+_{\mathrm{log,min}} \in [82; 90]$ and $y^+_{\mathrm{log,max}} \in [142; 150]$. We find $u_\tau = 0.7691\,\mathrm{m/s}$ for $\kappa = 0.41$ and $B = 5.0$ and $u_\tau = 0.7710\,\mathrm{m/s}$ for $\kappa = 0.384$ and $B = 4.17$. The deviation is smaller than 0.3%. The discussion of the uncertainties is summarised in table C.7 in appendix C.3. The latter value $u_\tau = 0.7710\,\mathrm{m/s}$ is used for the empirical correction method (D.1) in appendix D.

6.5 Log-law slope and intercept

We consider the results for the log-law slope and intercept in more detail. The question is, if a correlation for K_i and/or B_i as a function of local flow parameters can be found. An example is the correlation (2.16) by Nickels [2004], in which the relevant local flow parameter is Δp^+_x. This is related to the question whether the mean-velocity profile in the inner part of the inner layer can be described as a function of local flow parameters.

In figure 6.4 (a) we plot K_i versus Δp^+_x, as proposed by Nickels [2004]. The correlation (2.16) is included. The error bars for both quantities Δp^+_x and K_i are also attached. The uncertainty of Δp^+_x uses an assumed uncertainty of 5% for $\mathrm{d}P_\mathrm{w}/\mathrm{d}x$. The symbols indicate the method used to determine u_τ. We observe a smaller value for K_i for the case $U_\infty = 23\,\mathrm{m/s}$, which has a larger value for Δp^+_x, than for the case $U_\infty = 36\,\mathrm{m/s}$. Thus the results are consistent with the proposal by Nickels in the sense that K_i is decreasing for increasing values of Δp^+_x. As a reference value for κ for zero pressure gradient turbulent boundary layers, we assume $\kappa = 0.40 \pm 0.02$, with an uncertainty motivated by Bailey et al. [2014]. We find a reduction of K_i in the APG region compared to $\kappa = 0.40$, but this reduction is within the estimated uncertainty bounds.

Moreover we observe a significant role of the method to determine u_τ. The Clauser chart method (CCM) yields lower values for u_τ, and hence larger values for Δp^+_x, and lower smaller for K_i are obtained. This gives a warning that a possible change of K_i can appear enlarged if u_τ is used from a standard Clauser chart method.

Regarding the intercept B_i, the values for $K_\mathrm{i} B_\mathrm{i}$ are plotted against B_i in Figure 6.4 (b) and follow the trend of the correlation proposed by Nagib and

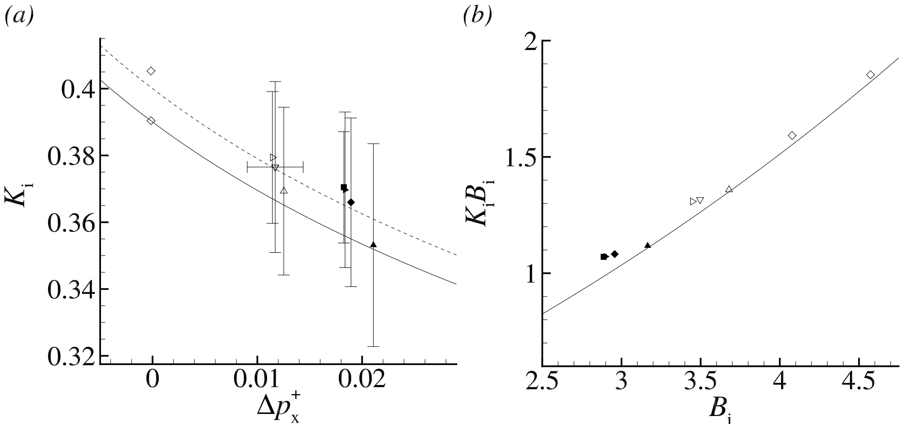

Figure 6.4: (a) Log-law slope K_i vs. Δp_x^+. The symbols take into account the method used for u_τ. For the 2D μPTV data for $U_\infty = 23\,\mathrm{m/s}$: ■, OFI; ♦, fit to $u^+ = y^+$; ►, fit to profile by Nickels [2004]; ▲, Clauser chart. For the 3D LPT data for $U_\infty = 36\,\mathrm{m/s}$: △, Clauser chart; ▷, fit to profile by Nickels [2004]; ▽, Clauser chart with empirical correction. For the 2D2C PIV data using OFI for u_τ: ◊, $x = 8.12\,\mathrm{m}$ at almost zero pressure gradient; solid line, correlation by Nickels [2004] for $\kappa_0 = 0.39$; dashed line, correlation by Nickels [2004] using $\kappa_0 = 0.40$. (b) Plot of $K_\mathrm{i}B_\mathrm{i}$ and vs B_i. Same symbols as in the figure left; solid line, correlation by Nagib and Chauhan [2008].

Chauhan [2008]. There is a detail that needs further investigation in future research, viz., the symbols at APG for the Clauser chart are closer to the correlation than the symbols for the more accurate methods for u_τ. However, here we need to consider the possible role of history effects. For a discussion we refer to section 9.4

6.6 On the half-power law region

We study the hypothesis of a half-power law region (or: sqrt-law region) above the log-law. We attempt to identify a region where the mean velocity profile can be described by the sqrt-law (2.17) using the mean velocity slope diagnostic function (2.21). First we consider the results for the case $U_\infty = 23\,\mathrm{m/s}$. We use the 2D2C PIV data evaluated using the single-pixel ensemble correlation method and u_τ from OFI. In figure 6.5 (a) we show the mean velocity profile and the fit to the sqrt-law. The least-squares fit of (2.17) to the data is computed in the region where the slope diagnostic function (2.21) shows a small plateau, which is shown in figure 6.5 (b). The single-pixel data show an approximative plateau in the region $500 < y^+ < 860$, whereas the window-correlation data are smoother and show a little smaller plateau in the region $520 < y^+ < 840$. Interestingly, the outer edge of the approximative plateau $y^+ \approx 840$ corresponds to $0.115\delta_{995}^+$, which is in good agreement with the outer edge of the log-law at zero pressure gradient. The single-pixel results for the slope diagnostic function exhibit some oscillations and smoothing was not applied in order not to influence the results. We note that in the region $y^+ < 200$ the slope of the single-pixel data shows a

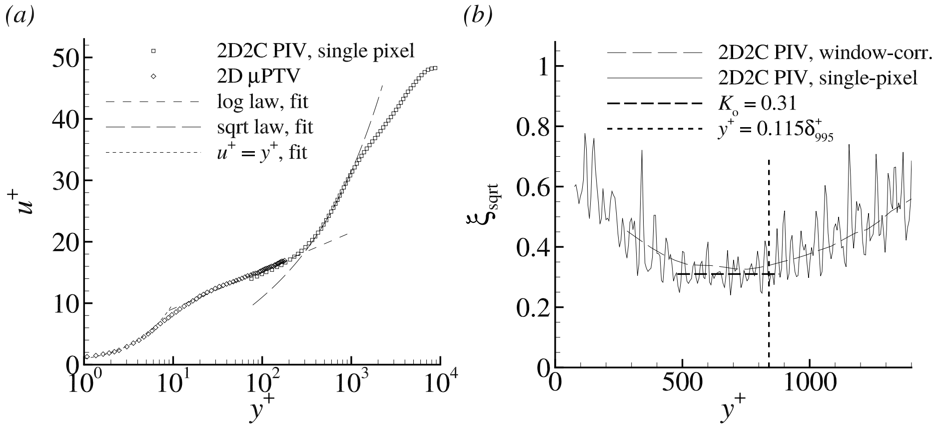

Figure 6.5: 2D2C PIV results for $U_\infty = 23\,\mathrm{m/s}$. (a) Composite profile and sqrt-law region. (b) Mean velocity slope diagnostic function of the sqrt-law.

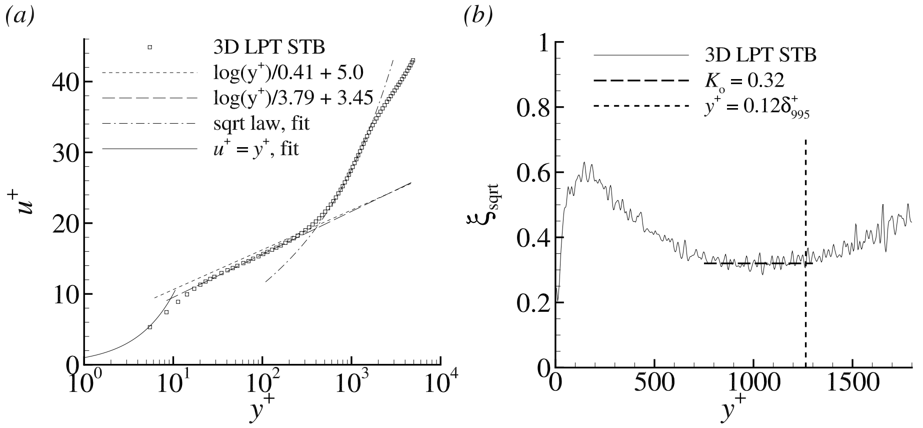

Figure 6.6: 3D LPT STB results for $U_\infty = 36\,\mathrm{m/s}$. (a) Composite profile and sqrt-law region. (b) Mean velocity slope diagnostic function of the sqrt-law.

small difference compared to the μPTV data.

For the case of the larger Reynolds number at $U_\infty = 36\,\mathrm{m/s}$ the mean velocity profile and the fit to the sqrt-law are shown for the 3D LPT data in figure 6.6 (a). A region of an approximative plateau for the slope diagnostic function (2.21) can be observed for $y^+ > 750$ which extends up to around $y^+ \approx 1260$, see figure 6.6 (b). Its outer edge corresponds to $0.12\delta^+_{995}$. The minimum region appears more clearly as an approximative plateau than for the lower Reynolds number case.

As a final remark, we note that the mean velocity profile cannot be fitted by the sqrt-law (2.17) in the entire inner region, say, $y^+ \in [150, 0.12\delta^+_{99}]$.

The slope coefficient K_o can be determined by a least-square fit of (2.17) to the data. For the case $U_\infty = 23\,\mathrm{m/s}$ we obtain $K_\mathrm{o} = 0.310$ for the single-pixel data and $K_\mathrm{o} = 0.341$ for the window correlation data, if for u_τ the OFI result is used. For the case $U_\infty = 36\,\mathrm{m/s}$ we obtain $K_\mathrm{o} = 0.320$ for the 3D LPT STB data, if for u_τ the least-squares fit of the data to the profile by Nickels is used.

6.7 A model for the wall law at adverse pressure gradient

An attractive aspect of the composite mean velocity profile is that it can describe both zero pressure gradient flows and adverse pressure gradient flows, if we assume that the wall distance of the change from the log-law to the sqrt-law depends on Δp_x^+ and possibly on additional parameters. On the one hand, there is the limit case of ZPG, i.e., for very small values of Δp_x^+. Then the outer edge of the log-law region extends up to the outer edge of the inner layer and the sqrt-law region disappears. The other limit case is $u_\tau \to 0$ and $\Delta p_x^+ \to \infty$, as the flow approaches separation. Then the sqrt-law occupies almost the entire inner layer, possibly except a thin viscous region near the wall.

Using this idea, we consider the streamwise evolution of a flow from ZPG to APG up to the verge of separation. In the first stage, for moderate values of Δp_x^+ due to the still large values of u_τ, $y^+_{\mathrm{log,max}}$ is progressively reduced and the composite profile describes a progressive breakdown of the log-law region, see Galbraith et al. [1977]. Above the log-law region, a sqrt-law region appears. Note that for small values of Δp_x^+, the value of K_i is practically unchanged, if the model by Nickels [2004] is assumed. In the second stage, for significantly large values of Δp_x^+, the extent of the log-law fit region is further reduces and K_i and B_i would change following Nickels [2004]. This can be viewed as a general breakdown of the log-law in the sense of Galbraith et al. [1977].

The parametrisation of the composite wall law in Knopp [2016], of a similar composite wall law in Kader and Yaglom [1978] and of the sqrt-law in Afzal [1996, 2008] is based on Δp_x^+. In the next two sections, we will develop the idea that also the local flow deceleration, characterised by $\Delta u^+_{\tau,x}$, needs to be taken into account.

6.8 Summary

To summarise the results of this section, we find that the mean velocity profile in the inner layer can be described by a composite form. The data can be fitted by a log-law in a thin log-law region, above which the data can be fitted by a sqrt-law up to $0.12\delta_{99}$. The parameters of the wall law are the slope coefficient for the log-law K_i and for the sqrt-law K_o, and the extent of the log-law region $y^+_{\mathrm{log,max}}$ and the begin of the sqrt-law region $y^+_{\mathrm{sqrt,min}}$. Regarding K_i, the results tend to support the hypothesis by Nickels [2004] that K_i is decreasing with increasing values of Δp_x^+ at APG, but significance cannot be shown due to the measurement uncertainty. The open question is, if $y^+_{\mathrm{log,max}}$ and $y^+_{\mathrm{sqrt,min}}$ can be described by suitable flow parameters. For this purpose we study the Reynolds stresses and the mean-momentum balance in the next section.

Chapter 7

Results for the Reynolds stresses at adverse pressure gradient

In this section we study the Reynolds stresses and the mean-momentum balance. The aim is to find the dominant terms of the mean-momentum balance and to characterise them using suitable flow parameters. This will lead to a two-parameter model for the total shear stress based on the pressure gradient parameter and the wall-shear stress gradient parameter.

We consider the results at the detail measurement position $x_{\mathrm{ref}} = 9.944\,\mathrm{m}$ in the adverse pressure gradient region. The position is located $1.14\delta_{99,\mathrm{apg}}$ downstream of the end of surface curvature. We consider the 3D LPT data for the case $U_\infty = 36\,\mathrm{m/s}$. We mainly use the data for the evaluation using the large sampling volume (3D LPT average), as described in section 3.2.2. For a detailed view near the wall we additionally show the data for the evaluation using the small sampling volume (3D LPT detail) due to the filtering effect near the wall for the large sampling bin.

7.1 Mean momentum balance in differential form

The terms of the mean momentum equation in differential form (2.1) are studied first. This is motivated by the work by Wei et al. [2005a] for the zero pressure gradient case. The 3D LPT data provide all terms arising in (2.1), in particular all spatial derivatives of U_i and $\overline{u_i' u_j'}$ $(i, j = 1, 2, 3)$. The viscous stresses are small for $y^+ > 100$ and are not shown. The pressure gradient term is reconstructed from the balance of all remaining terms. The fit of a constant pressure gradient for $250 < y^+ < 1600$ is also shown. The data are non-dimensionalised using u_τ and ν. The results are shown for $y < 0.35\delta_{99}$ in figure 7.1 (a). A detailed view for $y < 0.15\delta_{99}$ is given in figure 7.1 (b). For clarity only every fourth symbol is shown in figure 7.1 (a) and every second symbol in figure 7.1 (b).

The dominant terms are the pressure gradient, the mean convection and the turbulent shear stress in the region $y < 0.35\delta_{99}$. We see that $|V\,\partial U/\partial y|$ is not negligible compared to $|U\,\partial U/\partial x|$, so that both contributions need to be

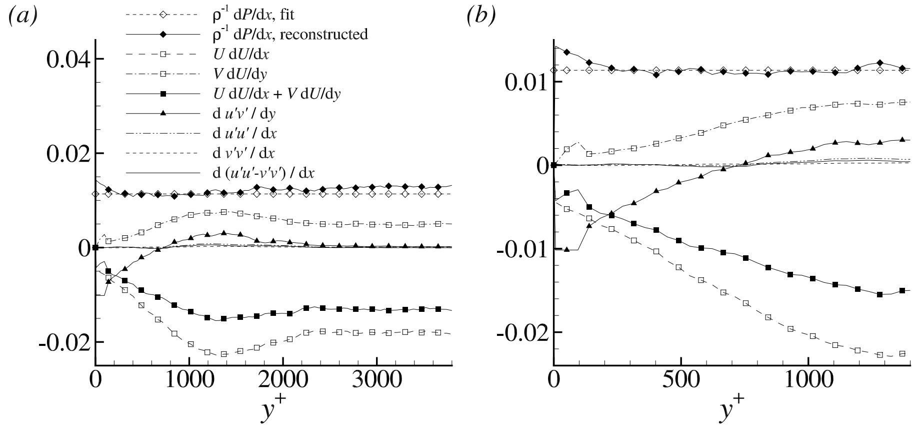

Figure 7.1: (a) Terms of the mean momentum equation in differential form computed from the 3D LPT data for $U_\infty = 36\,\mathrm{m/s}$. (b) Zoom for the inner layer $y < 0.12\delta_{99}^{+}$.

considered. The pressure gradient term and the sum of the mean convective terms give the largest contribution for $y^+ > 450$, where the magnitude of the turbulent shear stress is only 30% of the convective term. Closer to the wall, for $y^+ < 220$, the largest terms are the pressure gradient term and the turbulent shear stress. The ratio of the viscous to turbulent shear stress is 0.02 at $y^+ = 130$ and is decreasing for larger y^+-values. For $y^+ < 130$ the data are not considered to be sufficiently accurate since the number of samples is not large enough to obtain fully converged profiles for the gradients and the wall-normal size of the sampling volume is expected to cause a significant filtering error.

The streamwise gradients of the normal stresses are negligible small for $y^+ < 840$. For $y^+ > 840$, they grow slowly, and $\partial\overline{u'^2}/\partial x$ and $\partial(\overline{u'^2} - \overline{v'^2})/\partial x$ reach a small local maximum at around $y^+ = 1240$, see figure 7.1 (b). As $\partial\overline{u'^2}/\partial x$ is positive and $\partial\overline{v'^2}/\partial x$ is negative in this region, the sum $\partial(\overline{u'^2} - \overline{v'^2})/\partial x$ is smaller than $\partial\overline{u'^2}/\partial x$. The magnitude of $\partial(\overline{u'^2} - \overline{v'^2})/\partial x$ is 25% of the turbulent shear stress term at $y^+ = 1240$. Compared to other results in the literature, the non-negligible role of the streamwise gradients of the normal stresses in adverse pressure gradient flows, "[...] particularly those approaching separation [...]", is pointed out in Castillo et al. [2004], who refers to the flows by Simpson et al. [1981], Dengel and Fernholz [1990], Alving and Fernholz [1995b], and Elsberry et al. [2000]. This is not seen in contradiction to the present result, since the present flow is far from incipient separation at $x_{\mathrm{ref}} = 9.944\,\mathrm{m}$ for $U_\infty = 36\,\mathrm{m/s}$.

In the outer layer, for $y^+ > 2500$ (or: $y^+ > 0.25\delta_{99}^{+}$), the contribution of the Reynolds stress terms to the mean momentum balance in the differential form is very small and the dominant terms are the pressure gradient and the sum mean inertial term. We suppose that this is strongly influenced by the significant reduction of the Reynolds stresses in the upstream region of convex surface curvature. This will be studied in section 9.

As a final remark, the momentum balance indicates that the pressure gradient is not constant in wall-normal direction up to the boundary layer edge at $x = 9.944\,\mathrm{m}$. RANS simulations reveal that the isolines of the pressure deviate from the wall-normal direction in the outer part of the boundary layer due to the surface curvature regions located upstream and downstream of the flat inclined plate.

7.2 Balance equation for the turbulent shear stress

We consider the momentum balance in the integral form (2.3) for the 3D LPT data at $U_\infty = 36\,\mathrm{m/s}$. This equation can be seen as a relation between the total shear stress τ^+ and the sum of the wall shear stress, the pressure gradient term, the mean inertia terms, and the normal stress gradient terms. The integrals I^+_{cu}, I^+_{cv} and I^+_{r} are evaluated numerically using the trapezoidal rule. The 3D LPT data provide all quantities, including $\partial U/\partial x$, $\partial \overline{u'^2}/\partial x$ and $\partial \overline{v'^2}/\partial x$.

Relation (2.3) can be used in different ways. First, it can be used as a consistency check for the experimental data. Secondly we can use (2.3) to assess and to improve the accuracy of the term with the largest assumed uncertainty. This largest assumed uncertainty might be associated with the Reynolds stresses for some older experimental data. In the present work, we use the balance (2.3) to assess and to improve the accuracy of the streamwise pressure gradient, since the Reynolds stresses are assumed to be accurate for the 3D LPT data. For this purpose we compare the directly measured total shear stress τ^+ and the exactly reconstructed total shear stress in inner viscous scaling (2.5), i.e.,

$$\tau^+_{\mathrm{reconstr}} = 1 + \Delta p^+_x y^+ + I^+_{\mathrm{cu}} + I^+_{\mathrm{cv}} + I^+_{\mathrm{r}} \,. \tag{7.1}$$

The notation $\tau^+_{\mathrm{reconstr}}$ indicates that the total shear stress is reconstructed from the remaining terms of the momentum balance. The improved value for $\mathrm{d}P_{\mathrm{w}}/\mathrm{d}x$ is determined by fitting (7.1) to the directly measured $\tau^+ = \mathrm{d}u^+/\mathrm{d}y^+ - \overline{u'v'}^+$ in the region $y^+ \lessapprox 760$ where τ^+ reaches its maximum. Figure 7.1 gives a motivation to assume that the streamwise pressure gradient is constant across the inner part of the boundary layer. The result for (7.1) is shown in figure 7.2. The profiles for $\tau^+_{\mathrm{reconstr}}$ agree closely with the exact total shear stress up to $y^+ \approx 760$ where τ^+ has its maximum. The term I^+_{r} is found to be small for $y^+ < 920$, and has a moderate, albeit discernible, effect on the slope $\partial\tau^+/\partial y^+$ for $y^+ > 920$.

7.3 A parametric model for the turbulent shear stress

The momentum balance is then used to assess the parametric model (2.8) for the total shear stress. The two approximations involved are the approximation of the mean inertia term using (2.6) and to neglect I^+_{r}. The highest level of modelling is to use the measured data for U^+ to evaluate I^+_{u}, i.e.,

$$\tau^+_{\mathrm{model,exact}} = 1 + \Delta p^+_x y^+ + \Delta u^+_{\tau,x} \int_0^{y^+} \left(U^+\right)^2 \mathrm{d}\tilde{y}^+ \tag{7.2}$$

which will be denoted by $\tau^+_{\mathrm{model,exact}}$ as the measured solution for U^+ is substituted. The model (7.2) provides a good quantitative approximation to (7.1) for $y^+ < 430$. The deviation between (7.2) and (7.1) including I^+_{r} is smaller than

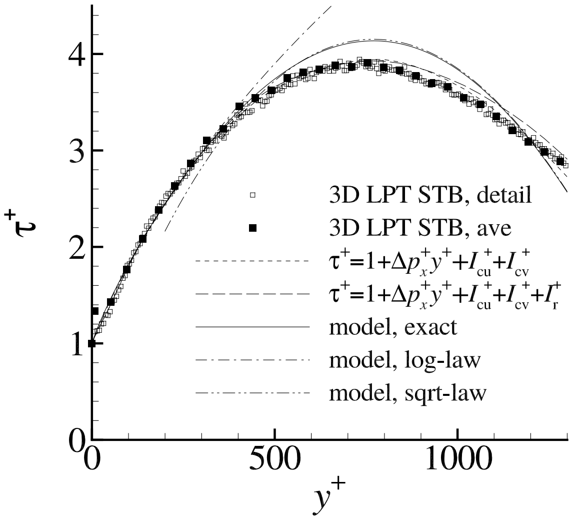

Figure 7.2: Total shear stress τ^+ computed from the 3D LPT data using the resolved Reynolds shear stress and reconstruction of τ^+ using (2.5) for $U_\infty = 36\,\mathrm{m/s}$ at $x = 9.944\,\mathrm{m}$. Moreover the model $\tau^+_{\mathrm{model,exact}}$ in (2.5), the approximation $\tau^+_{\mathrm{model,log}}$ in (7.3) and the approximation $\tau^+_{\mathrm{model,sqrt}}$ in (7.4) are shown.

1% for $y^+ < 430$ and 2.2% at $y^+ = 500$. For larger y^+-values, the deviation increases but the model still provides a qualitatively satisfying approximation of (7.1). In particular, the wall-distance where τ^+ reaches its maximum can be predicted. Model (7.2) relates τ^+ to the two flow parameters Δp_x^+ and $\Delta u^+_{\tau,x}$. This could explain the observation that a model for τ^+ based on Δp_x^+ alone has not been found in the literature.

7.3.1 An analytical model for the log-law region reviewed

The next level of approximation is to use an approximative profile for U^+. Galbraith et al. [1977] describe a result for the log-law region. They use an analytical profile for $y^+ < 30$ and the log-law for $y^+ > 30$ and obtain

$$\tau^+_{\mathrm{model,log}} = 1+\Delta p_x^+ y^+ +\Delta u^+_{\tau,x}\left[y^+\left(k_1\left(\log y^+\right)^2 + k_2\log(y^+) + k_3\right) + k_4\right] \quad (7.3)$$

for $y^+ > 30$. In the present work we use the log-law notation (6.2) with coefficients K_i and B_i. Following Galbraith et al. [1977], the coefficients can be written as

$$\begin{aligned} k_1 &= \frac{1}{K_\mathrm{i}^2}, \qquad k_2 = \frac{2B_\mathrm{i}}{K_\mathrm{i}} - \frac{2}{K_\mathrm{i}^2}, \qquad k_3 = \frac{2}{K_\mathrm{i}^2} - \frac{2B_\mathrm{i}}{K_\mathrm{i}} + B_\mathrm{i}^2 \\ k_4 &= -\frac{30\left(\log 30\right)^2}{K_\mathrm{i}^2} + \frac{60\log 30}{K_\mathrm{i}^2} - \frac{60}{K_\mathrm{i}^2} - \frac{60B_\mathrm{i}\log 30}{K_\mathrm{i}} + \frac{60B_\mathrm{i}}{K_\mathrm{i}} - 30B_\mathrm{i}^2 \end{aligned}$$

The total shear stress given by (7.3) is an analytical function in y^+ and depends on the two local flow parameters Δp_x^+ and $\Delta u_{\tau,x}^+$. The result for (7.3) is shown in figure 7.2, where we use $K_\mathrm{i} = 0.38$ and $B_\mathrm{i} = 3.44$, see figure 6.3 (b). The deviation between (7.3) and (7.2) is below 0.3% for $y^+ < 300$ and 1.8% for $y^+ = 400$. This y^+-region is in good agreement with the extent $y \leq 0.05\delta_{99}$ assumed for the outer edge of the log-law region in the profile family by Thompson [1967] which was used by Galbraith et al. [1977]. For $y^+ > 400$ the difference in the slopes of the two curves becomes clearly visible.

7.3.2 An analytical model for the sqrt-law region

For the aim to extend (7.3) for $y^+ > y^+_{\mathrm{sqrt,min}}$ up to $y^+ = 0.12\delta^+_{99}$, we use the composite formula for U^+. We use (7.3) up to the outer edge of the log-law region. In the sqrt-law region, we substitute (2.17) for U^+. The terms of $\left(U^+\right)^2$ were integrated from the wall to y^+. The details are described in appendix E. The final result is

$$\begin{aligned}
I_\mathrm{u}^+ \quad = \quad & c_{a1}\Delta p_x^+ \left(y^+\right)^2 + \frac{c_{b1}}{\Delta p_x^+}\left[\left(1+\Delta p_x^+ y^+\right)^{3/2} - 1\right]\log\left(y^+\right) \\
& + \frac{c_{b2}}{\Delta p_x^+}\left(1+\Delta p_x^+ y^+\right)^{3/2}\log\left(\sqrt{1+\Delta p_x^+ y^+}+1\right) + \frac{c_{b3}}{\Delta p_x^+}\left(1+\Delta p_x^+ y^+\right)^{3/2} \\
& + c_{c0}\, y^+ + c_{c1}\, y^+ \log\left(y^+\right) + c_{c2}\, y^+ \log^2\left(y^+\right) + c_{c3}\, y^+ \log\left(\sqrt{1+\Delta p_x^+ y^+}+1\right) \\
& + c_{c4}\, y^+ \log\left(y^+\right)\log\left(\sqrt{1+\Delta p_x^+ y^+}+1\right) + c_{c5}\, y^+ \log^2\left(\sqrt{1+\Delta p_x^+ y^+}+1\right) \\
& + \frac{c_{d1}}{\Delta p_x^+}\left[\sqrt{1+\Delta p_x^+ y^+} - 1\right]\log\left(y^+\right) \\
& + \frac{c_{d2}}{\Delta p_x^+}\left[\sqrt{1+\Delta p_x^+ y^+} + 1\right]\log\left(\sqrt{1+\Delta p_x^+ y^+}+1\right) + \frac{c_{d3}}{\Delta p_x^+}\sqrt{1+\Delta p_x^+ y^+} \\
& + \frac{c_{e1}}{\Delta p_x^+}\log\left(\sqrt{1+\Delta p_x^+ y^+}+1\right) + \frac{c_{e0}}{\Delta p_x^+}
\end{aligned}$$

with constants

$$\begin{aligned}
c_{a1} &= \frac{2}{K_\mathrm{o}^2}\ , \quad c_{b1} = \frac{8}{3K_\mathrm{o}^2}\ , \quad c_{b2} = -\frac{16}{3K_\mathrm{o}^2}\ , \quad c_{b3} = \frac{8B_\mathrm{o}}{3K_\mathrm{o}} - \frac{16(1-\log(2))}{3K_\mathrm{o}^2} \\
c_{c0} &= \left(\frac{16}{3} - 8\log(2) + 4\log^2(2)\right)\frac{1}{K_\mathrm{o}^2} - \frac{4(1-\log(2))B_\mathrm{o}}{K_\mathrm{o}} + B_\mathrm{o}^2 \\
c_{c1} &= \frac{2B_\mathrm{o}}{K_\mathrm{o}} - \frac{4(1-\log(2))}{K_\mathrm{o}^2}\ , \quad c_{c2} = \frac{1}{K_\mathrm{o}^2}\ , \quad c_{c3} = \frac{8(1-\log(2))}{K_\mathrm{o}^2} - \frac{4B_\mathrm{o}}{K_\mathrm{o}} \\
c_{c4} &= -\frac{4}{K_\mathrm{o}^2}\ , \quad c_{c5} = \frac{4}{K_\mathrm{o}^2}\ , \quad c_{d1} = -\frac{4}{K_\mathrm{o}^2}\ , \quad c_{d2} = \frac{8}{K_\mathrm{o}^2} \\
c_{d3} &= \frac{8(1-\log(2))}{K_\mathrm{o}^2} - \frac{4B_\mathrm{o}}{K_\mathrm{o}}\ , \quad c_{e1} = -\frac{48}{9K_\mathrm{o}^2}\ , \quad c_{e0} = \frac{4B_\mathrm{o}}{3K_\mathrm{o}} - \frac{8(1+\log(2))}{3K_\mathrm{o}^2}
\end{aligned}$$

The result for $\tau^+_{\mathrm{model,sqrt}}$ is shown in figure 7.2, where we use the notation

$$\tau^+_{\mathrm{model,sqrt}} = 1 + \Delta p_x^+ y^+ + \Delta u_{\tau,x}^+ I_\mathrm{u}^+ \tag{7.4}$$

We use the sqrt-law for U^+ for $y^+_{\mathrm{sqrt,min}} \geq 580$. The curve is shifted by hand to match the reference curve at $y^+_{\mathrm{sqrt,min}}$. For the coefficients we use $K_{\mathrm{o}} = 0.320$ and $B_{\mathrm{o}} = -4.69$ found for the least-squares fit to the sqrt-law. Regarding the case $\Delta p^+_x \to 0$, we note that then the outer edge of the log-law region extends up to the outer edge of the inner layer and the sqrt-law region disappears.

7.4 Outer peak of the turbulent shear stress

The observation of an outer peak in the Reynolds stresses was often reported for the outer part of adverse pressure gradient turbulent boundary layers, see e.g. Gungor et al. [2016]. Examples are the equilibrium turbulent boundary layer by Skare and Krogstad [1994] at a high $Re_\theta > 40000$, and the non-equilibrium flows by Maciel et al. [2006b] at $Re_x = 1.5 \times 10^6$, and by Nagano et al. [1991] for Re_θ up to 3350. For the present flow, the Reynolds stresses are strongly reduced for $y > 0.1\delta_{99}$ in the region of convex surface curvature and streamwise changing pressure gradient from favourable to adverse. Therefore an outer peak of the Reynolds stresses cannot be observed for the present flow in the APG region.

There are two related questions, which arise. The first question is the change of the position of the outer peak with the Reynolds number, and its behaviour for very large Reynolds numbers. The second question is the role of the mean inertia term, in particular in the absence of upstream curvature effects. We expect that a correlation between the maximum of the turbulent shear stress and β_{RC} as described for equilibrium flows in figure 8 of Skare and Krogstad [1994], is limited to these flows. An investigation of the role of Δp^+_x and $\Delta u^+_{\tau,x}$ to characterise the outer peak is not attempted in this work. In particular, if the outer peak is located in the middle of the boundary layer, then history effects can be expected to be too complicated to be described in a local model, even in the absence of upstream curvature effects.

7.5 A parametric model for the turbulent viscosity

The turbulent viscosity can be computed from the definition

$$\nu^+_t = \frac{-\overline{u'v'}^+}{\mathrm{d}u^+/\mathrm{d}y^+} \tag{7.5}$$

For the exact computation of ν^+_t, we use the measured data for $\overline{u'v'}$ and for $\mathrm{d}u^+/\mathrm{d}y^+$. As a minor technical aspect, for the computation of $\mathrm{d}u^+/\mathrm{d}y^+$ at y^+_i, we use a linear regression over an n-point stencil, i.e., over the subset of data points $\{y_j \mid j = i-n, \ldots, i+n\}$, with $n = 3$ to apply a small amount of smoothing to the gradients. This corresponds to an average over six interrogation windows or $18\delta^+_\nu$ in viscous units.

As a model for ν_t to describe (7.5), we approximate the turbulent shear stress using $\tau^+_{\mathrm{model,exact}}$ in (7.2), where the integral is evaluated using the measured profile for U^+

$$\nu^+_{t,\mathrm{model,exact}} = \frac{\tau^+_{\mathrm{model,exact}}}{(\mathrm{d}u^+/\mathrm{d}y^+)_{\mathrm{exact}}} \tag{7.6}$$

Then we consider two parametric models. To approximate ν_t in the log-law region, we use $\tau^+_{\mathrm{model,log}}$ in (7.3) for the shear stress and the gradient of the log-law for the mean velocity gradient

$$\nu^+_{t,\mathrm{model,log}} = \frac{\tau^+_{\mathrm{model,log}}}{(\mathrm{d}u^+/\mathrm{d}y^+)_{\mathrm{log}}} \tag{7.7}$$

This leads to the relation

$$\nu^+_{t,\mathrm{model,log}} = K_\mathrm{i} y^+ \left[1 + \Delta p^+_x y^+ + \Delta u^+_{\tau,x} \left[y^+ \left(k_1 \left(\log y^+\right)^2 + k_2 \log(y^+) + k_3\right) + k_4\right]\right] \tag{7.8}$$

In order to extend this relation for the sqrt-law region up to $y^+ = 0.12\delta^+_{99}$, we substitute the sqrt-law solution (7.4) for the shear stress and the sqrt-law slope for the mean velocity gradient into (7.5). Then we obtain the relation

$$\nu^+_{t,\mathrm{model,sqrt}} = \frac{\tau^+_{\mathrm{model,sqrt}}}{(\mathrm{d}u^+/\mathrm{d}y^+)_{\mathrm{sqrt}}}, \qquad y^+ > y^+_{\mathrm{sqrt,min}} \tag{7.9}$$

For comparison we consider two algebraic relations for the turbulent viscosity in the log-law region. First we consider the relation for zero pressure gradient flows

$$\nu^+_t = K_\mathrm{i} y^+ \tag{7.10}$$

Secondly we consider the relation proposed by Nituch et al. [1978] to improve the Cebeci-Smith eddy-viscosity model (see also Granville [1989])

$$\nu^+_t = \frac{1 + \Delta p^+_x y^+}{(\mathrm{d}u^+/\mathrm{d}y^+)_{\mathrm{log}}} = K_\mathrm{i} y^+ (1 + \Delta p^+_x y^+) \tag{7.11}$$

which uses the linear stress model and the log-law for the mean velocity gradient in (7.5).

The results are shown in figure 7.3. The model approximation based on the measured solution (7.6) is in close agreement with ν_t evaluated from (7.5) up to $y^+ = 400$. For $y^+ > 400$, the deviation is more pronounced than for the shear stress, see figure 7.2. The reason for this is the stronger weighting caused by differences between the exact and the modelled shear stress for increasing y^+ values, due to decreasing values of the mean velocity gradient in the denominator. The ZPG relation (7.10) cannot describe ν_t in the log-law fit region. The APG relation (7.11) captures the steeper gradient of ν^+_t compared to zero pressure gradient, but overpredicts ν_t for $y^+ > 80$ and fails to capture the decreasing slope of ν_t for $y^+ > 180$ and the local maximum. In both cases we use $K_\mathrm{i} = 0.38$ based on the experimental data. Relation (7.8) with $K_\mathrm{i} = 0.38$ gives a closer approximation to the exact curve for ν_t for $y^+ < 150$. However, the behaviour of ν_t for $y^+ > 180$ cannot be captured. Relation (7.9) with $K_\mathrm{o} = 3.20$ gives

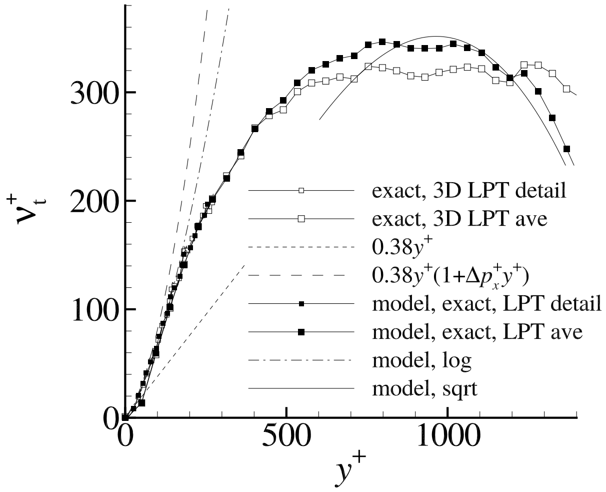

Figure 7.3: Turbulent viscosity ν_t computed from the 3D LPT data and for $\nu^+_{t,\text{model,exact}}$ in (7.6), for $\nu^+_{t,\text{model,log}}$ in (7.7), for $\nu^+_{t,\text{model,sqrt}}$ in (7.9), and for the relation for ZPG in (7.10) and for APG in (7.11) for the case $U_\infty = 36\,\text{m/s}$ at $x = 9.944\,\text{m}$.

a much better qualitative description in the region $850 < y^+ < 1150$, which is the core region of the plateau for the mean velocity slope diagnostic function, see figure 6.6. However for $y^+ < 750$ the deviation becomes clearly visible. The difference is caused by the subtle deviation of the mean velocity gradient from the sqrt-law for $y^+ < 750$, which can be seen from the slope diagnostic function in figure 6.6. In the transition region from a log-law to a sqrt-law, say in the region $160 < y^+ < 700$, neither (7.8) nor (7.9) provide a reasonable description for ν_t. This region needs further work in future research. We conclude that a qualitative and quantitative description of ν_t up to $0.12\delta_{99}$ needs at least the two flow local parameters Δp_x^+ and $\Delta u^+_{\tau,x}$.

The derivation of a sqrt-law in the classical literature, e.g., Szablewski [1954], Stratford [1959], Townsend [1961], uses the assumption of a linear shear stress. The present investigation is seen as an indication that the sqrt-law can be a reasonably good fit to the mean velocity, albeit the total shear stress is far from being linear in the region of the sqrt-law. Moreover the motivation of the sqrt-law using a mixing length approach for the turbulent viscosity in conjunction with the assumption of a linear shear stress appears to need a critical review.

7.6 Summary

We find that the dominant terms of the mean momentum balance in the inner layer are the mean inertia term, the streamwise pressure gradient, and the turbulent shear stress. The mean inertia term can be modeled using the mean velocity profile and the wall shear stress gradient parameter, see section 2.3. The model for the total shear stress (2.8) is found to describe the experimental data qualitatively and quantitatively. The question arises if the composite form of the mean velocity profile, parametrised using the pressure gradient parameter and the wall shear stress gradient parameter, can also describe other representative turbulent boundary layer flows at APG from the literature. This will be studied in the next section.

Chapter 8

Characterisation and similarity of the inner layer

The idea, that the leading order parameters for the total shear stress and the composite form of the mean velocity profile are the pressure gradient parameter and the wall-shear stress gradient parameter, was developed so far for the present flow experiment. The aim of this section is to investigate this idea for other representative turbulent boundary layer flows at APG. Therefore we set-up and study a data base from the literature.

The characterisation of turbulent boundary layer flows at adverse pressure gradient using suitable boundary layer parameters is still an open question, cf. Vila et al. [2017]. The parameter space is much wider than for fully developed turbulent flows in channels and pipes and for turbulent boundary layers at zero pressure gradient. In this section we assume that the dominant parameters are the pressure gradient and the local flow acceleration, motivated by the results of section 7. The role of upstream history effects due to the accelerating ramp with possible Görtler type vortices is briefly addressed in appendix F, and the region of a streamwise changing pressure gradient and convex surface curvature upstream of the APG region will be studied in section 9.

8.1 Data base approach

To evaluate the sensitivity and the richness of the parameter space of APG flows qualitatively, we set up a data base from the literature and the experiment. The data base covers the test cases collected in Coles and Hirst [1969]. Moreover we use the experiments by Samuel and Joubert [1974], Skare and Krogstad [1994], and Marusic and Perry [1995]. We assume that the sqrt-law region between the log-law region and the outer part of the boundary layer is arising only for sufficiently large Re. Therefore we only consider velocity profiles at $Re_\theta > 10000$. Moreover we restrict the data base to boundary layers, i.e., Couette-Poiseuille flows are not considered. We use the identifiers (IDENTs, abbreviated IDs) for the flows and for the streamwise positions given within the collection by Coles and Hirst [1969]. We note that the flow 2900 by Perry is omitted, since its results show some differences compared to the other flows. This might be explained by the configuration, where the mean velocity profiles are measured on a 5m long flat plate mounted at an incidence angle of 9.5° into the center of the wind-tunnel with a flap used to control the flow on the leading edge. Regarding the flow 2600 by Bradshaw, we omit profile 2604, since possible initial effects of interference between the boundary layer on the upper and lower wall are mentioned in Coles and Hirst [1969].

The data-base covers equilibrium flows and non-equilibrium flows. If relation (2.8) were exact, then self similar solutions in the inner layer can be expected only if both Δp_x^+ and $\Delta u_{\tau,x}^+$ have the same values. We remark that some experiments established conditions for similarity in the inner and outer flow, leading to the condition that u_τ/U_e and hence the skin friction coefficient based on U_e (instead of U_∞) remains constant in streamwise direction and $U_e \sim (x - x_0)^{-m}$, where x_0 is the virtual origin of the equilibrium state and $0 < m < 0.23$ for attached flows at adverse pressure gradient. Then $\Delta u_{\tau,x}^+ \sim -m(x-x_0)^{-m-1}$ is decreasing slowly in streamwise direction.

For all flows in the data-base, we use the values for u_τ given by the original authors which are tabulated in Coles and Hirst [1969]. Most authors used an indirect method for u_τ. The values for $\mathrm{d}u_\tau/\mathrm{d}x$ are computed using a finite difference approximation.

8.2 Boundary layer characterisation for the inner layer

We attempt to use the parameters Δp_x^+ and $\Delta u_{\tau,x}^+$ to characterise the inner layer of a turbulent boundary layer over a flat plate, motivated by relation (2.8). For this purpose we introduce the $\Delta u_{\tau,x}^+$-Δp_x^+-plane. For a given flow, the streamwise evolution of $\Delta u_{\tau,x}^+(x)$ and $\Delta p_x^+(x)$ can be parametrised by the streamwise position x. The trajectory through the $\Delta u_{\tau,x}^+$-Δp_x^+-plane describes the streamwise evolution of the flow parameters. For the test-cases of the data-base, this evolution is shown in figure 8.1. Each velocity profile at a certain measurement station corresponds to a point in the $\Delta u_{\tau,x}^+$- Δp_x^+- plane. Equilibrium flows and non-equilibrium flows are both included.

The history of a flow is contained in the trajectory through the $\Delta u_{\tau,x}^+$- Δp_x^+-plane, as far as upstream regions of acceleration and deceleration are concerned which effect u_τ. Here we focus on the adverse pressure gradient region of the different flows. The symbols within each equilibrium flow are much closer together than for the streamwise evolving flows. The trajectories of the non-equilibrium flows are from small values of $\Delta u_{\tau,x}^+$, Δp_x^+ towards large values of $\Delta u_{\tau,x}^+$, Δp_x^+ in streamwise direction, as u_τ is typically decreasing in streamwise direction in the APG region. For the streamwise evolving flows, the $\Delta u_{\tau,x}^+$-values of the symbols are within a certain band and larger than for the equilibrium flows. We also include the numerical results of the RANS simulations for two airfoil flows at high lift, where the flow on the upper airfoil surface experiences a significant adverse pressure gradient. The simulations use the Reynolds-stress transport turbulence model SSG/LRR-ω, see Eisfeld et al. [2016]. Both flows are at subsonic Mach numbers $Ma = 0.15$. For the NACA 4412 airfoil at Reynolds number $Re_c = 4.2 \times 10^6$ based on the chord length at an incidence angle $\alpha = 13°$, the flow separates in the rear part of the airfoil, whereas for the HGR01 airfoil at $Re_c = 2.5 \times 10^7$ and $\alpha = 10°$, the flow remains attached. The streamwise

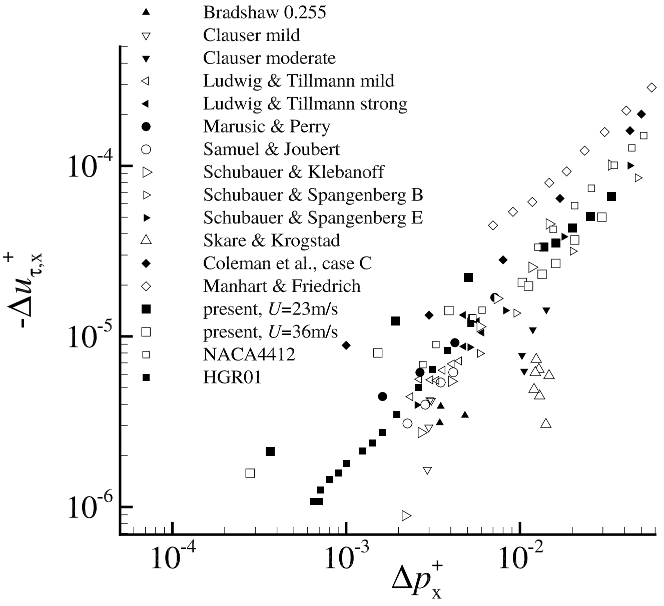

Figure 8.1: Characterisation of the flow in the inner layer of turbulent boundary layer flows at adverse pressure gradient using Δp^+_x and $\Delta u^+_{\tau,x}$.

evoluation in the $\Delta u^+_{\tau,x}$- Δp^+_x- plane is similar for the airfoil flows and for the boundary layer flows in the data-base.

8.3 Composite mean velocity profile

The composite form of the mean velocity profile in the inner layer with a log-law region and a sqrt-law region above can describe the mean velocity profiles of the present data base. This is shown exemplarily for the data by Samuel and Joubert [1974] at $\Delta p^+_x = 0.0040$ and for the data by Marusic and Perry [1995] at $\Delta p^+_x = 0.0042$ in figure 8.2. We include the log-law with $K_\mathrm{i} = 0.41$ and $B_\mathrm{i} = 5.0$ and a least-square fit of the sqrt-law (2.17) to the experimental data. The sqrt-law fit is in the region $y^+_{\mathrm{sqrt,min}} < y^+ < 0.15\delta_{99}$ for the profile by Marusic and Perry [1995]. For the profile by Samuel and Joubert [1974] the sqrt-law fit is up to $0.18\delta_{99}$ due to the relatively low Reynolds number.

8.4 Approximate model for the turbulent shear stress

In this section we study the approximative model for the turbulent shear stress (2.8) for cases of the data-base for which experimental data for the Reynolds stresses are available. The aim is to study the mean-inertia effects and to describe them using the parameter $\Delta u^+_{\tau,x}$. First we study the equilibrium flow by Skare and Krogstad [1994] at $x = 4.4\,\mathrm{m}$ where $\Delta p^+_x = 0.0132$ and

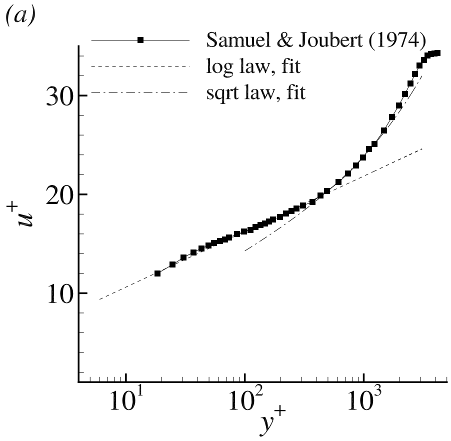

Figure 8.2: Composite structure of the mean velocity profile (a) for the data by Samuel and Joubert [1974] at $x = 3.04\,\mathrm{m}$ with $\Delta p_x^+ = 0.0040$ and $Re_\theta = 13500$, and (b) for Marusic and Perry [1995] at $x = 3.08\,\mathrm{m}$ with $\Delta p_x^+ = 0.0042$ and $Re_\theta = 19133$.

$\Delta u_{\tau,x}^+ = -4.4 \times 10^{-6}$, see figure 8.3 (a). The experimental data are for the turbulent shear stress, as the viscous shear stress is small for $y^+ > 100$. The contribution of the mean-inertial term to the total shear stress is small, which can be seen from the low value of $\Delta u_{\tau,x}^+$ compared to Δp_x^+. The linear stress relation $1 + \lambda \Delta p_x^+ y^+$ with $\lambda = 0.9$ gives a good approximation to the experimental data. The prediction by model (2.8) is close to the linear stress relation. From this the hypothesis arises that for flows near equilibrium with a small role of the mean-inertia terms, the linear stress model can be a reasonable approximation for the total shear stress in the inner layer. We remark that the parameter λ can be determined by a fit of the linear stress model to the model (2.8).

For the non-equilibrium flow by Marusic and Perry [1995], the mean-inertia terms become important. We consider the flow at $x = 2.64\,\mathrm{m}$, where $\Delta p_x^+ = 0.0042$ and $\Delta u_{\tau,x}^+ = -9.2 \times 10^{-6}$. We assume that the inner layer extends up to $y^+ = 0.15\delta_{99}^+ = 458$, as $\delta_{99}^+ = 3053$. The result is shown in figure 8.3 (b). Obviously the linear stress model cannot be fitted to the measured shear stress profile up to $0.15\,\delta_{99}^+$. The linear stress model with $\lambda = 0.7$ gives a reasonable approximation only near the wall. On the other hand, model (2.8) is able to describe the shear stress profile and its departure from a linear behaviour at least qualitatively.

We remark that we found the results of model (2.8) to be sensitive with respect to the parameter values for Δp_x^+ and $\Delta u_{\tau,x}^+$, and their measurement error and uncertainty. Moreover there is the question if all effects of first order importance are included in model (2.8). In the approximation leading to model (2.8), further higher order terms and their parameters may be missing. The streamwise gradient of the Reynolds normal stresses was omitted explicitely. Additional parameters involving $\mathrm{d}^2 P_\mathrm{w}/\mathrm{d}x^2$ and $(\mathrm{d}P_\mathrm{w}/\mathrm{d}x)(\mathrm{d}u_\tau/\mathrm{d}x)$ could be possible, see Knopp et al. [2015].

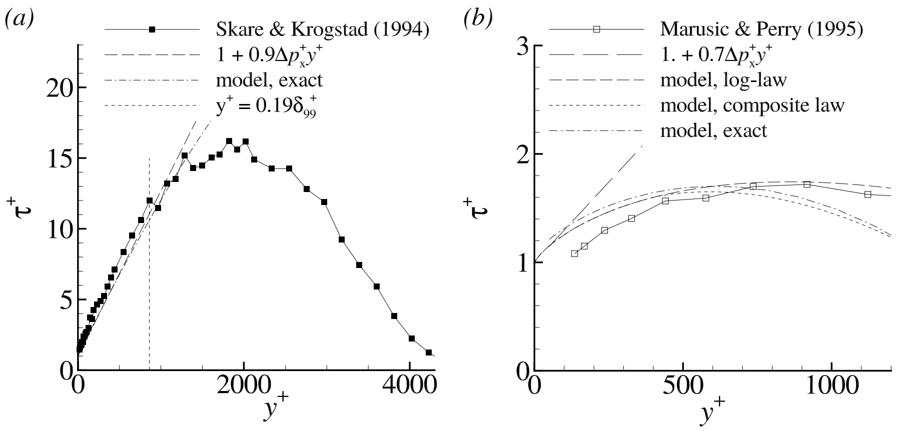

Figure 8.3: A model for the total shear stress at APG (a) for the flow by Skare and Krogstad [1994] near equilibrium at $x = 4.4\,\mathrm{m}$ where $\Delta p_x^+ = 0.0132$ and $\Delta u_{\tau,x}^+ = -4.4 \times 10^{-6}$ and (b) for the non-equilibrium flow by Marusic and Perry [1995] at $x = 2.64\,\mathrm{m}$ where $\Delta p_x^+ = 0.00422$ and $\Delta u_{\tau,x}^+ = -9.19 \times 10^{-6}$.

8.5 Similarity of the mean-velocity profiles in the inner layer

To study the question of mean flow similarity in the inner layer, we compare different mean velocity profiles of the data-base at stations with similar values for Δp_x^+ and $\Delta u_{\tau,x}^+$.

8.5.1 Results for moderate values of the pressure gradient parameter

First we consider moderate values for Δp_x^+, i.e., $\Delta p_x^+ \in [0.0025, 0.0035]$ in figure 8.4 (a), and $\Delta p_x^+ \in [0.0035, 0.0048]$ in figure 8.4 (b). The flow parameters are given in table 8.1. As a reference curve for comparison, we include the profile ID 2130 by Schubauer & Klebanoff at $\Delta p_x^+ = 0.004$ in both figures. The profiles shown in figure 8.4 (a) include the equilibrium flows by Clauser and by Bradshaw and different non-equilibrium flows. The values for $\Delta u_{\tau,x}^+$ are similar, albeit little larger in magnitude for the equilibrium flows. All curves are very close to each other in the inner 15% of the boundary layer. A small difference can be observed for the flow by Bradshaw, where the upward turn above the log-law begins at little larger y^+-value than for the other profiles. We note that the profiles with the largest Reynolds numbers are for the flow by Bradshaw and by Schubauer & Klebanoff, which also have the largest extent $y^+ = 0.15\delta_{99}^+$ of the inner layer. The velocity profiles shown in figure 8.4 (b) are also close to each other in the inner 15% of the boundary layer. The upward turn above the log-law for the different profiles is little larger than for the profile ID 2130, which is explained by the little larger value of Δp_x^+. We note that the profile ID 2130 has a larger value of δ_{99}^+ and hence a larger extent of the inner layer in terms of y^+ than the other flows in this figure.

The sources of uncertainties for u^+ versus y^+ are due to the uncertainty in

Author	ID	x	Re_θ	Δp_x^+	$\Delta u_{\tau,x}^+ \times 10^5$	β_{RC}	H_{12}
Ludwieg & Tillmann	1108	3.532 m	25870	0.00306	−0.557	3.282	1.519
Clauser, mild APG	2206	26.92 ft	15515	0.00309	−0.420	2.164	1.461
Clauser, mild APG	2207	29.75 ft	16182	0.00299	−0.292	2.172	1.443
Clauser, mild APG	2208	32.25 ft	17405	0.00303	−0.423	2.349	1.446
Bradshaw, $a = -0.255$	2603	5.417 ft	30247	0.00346	−0.311	4.292	1.558
Schubauer & Spangenb.	4804	8.333 ft	12094	0.00256	−0.396	1.430	1.442
Schubauer & Klebanoff	2128	21.00 ft	29379	0.00270	−0.273	3.202	1.444
Schubauer & Klebanoff	2130	22.00 ft	36066	0.00404	−0.545	5.710	1.521
Samuel & Joubert		2.87 m	12369	0.00350	−0.537	2.75	1.480
Samuel & Joubert		3.04 m	13498	0.00413	−0.616	3.59	1.510
Ludwieg & Tillmann	1205	2.782 m	19775	0.00475	−0.874	4.004	1.535
Marusic & Perry		2.24 m	10997	0.00266	−0.615	1.39	1.435
Marusic & Perry		2.64 m	14209	0.00422	−0.919	2.74	1.489

Table 8.1: Summary of boundary layer parameters for flows at moderate Δp_x^+-values.

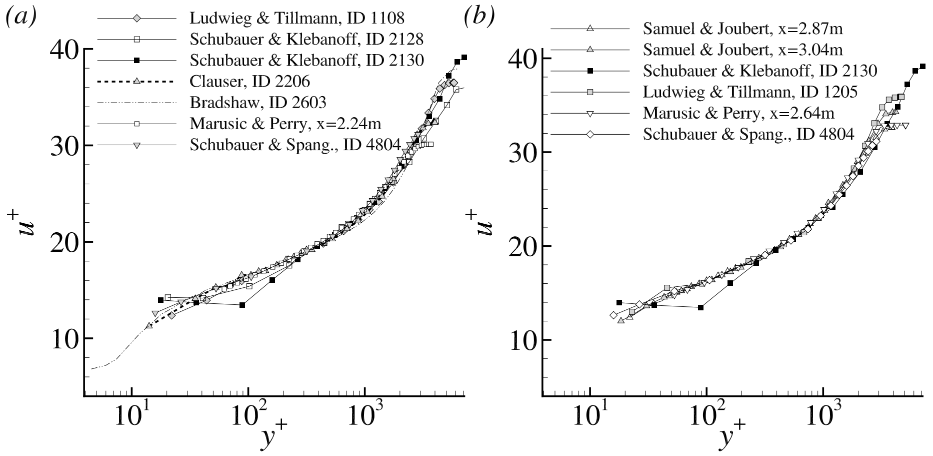

Figure 8.4: Mean velocity profiles at similar values of Δp_x^+ and $\Delta u_{\tau,x}^+$, see table 8.1.

Author	ID	x	Re_θ	Δp_x^+	$\Delta u_{\tau,x}^+ \times 10^5$	β_{RC}	H_{12}
Present flow, $U_\infty = 36\,\mathrm{m/s}$		9.944 m	51600	0.0120	−1.974	23.6	1.478
Schubauer & Spangenberg	4505	6.667 ft	15182	0.00952	−1.370	6.202	1.638
Schubauer & Klebanoff	2134	24.00 ft	53838	0.0117	−2.55	20.286	1.857
Schubauer & Klebanoff	2135	24.50 ft	58117	0.0147	−4.57	27.291	1.983

Table 8.2: Summary of boundary layer parameters for flows at moderately strong Δp_x^+-values.

u_τ used for scaling and in the parameters Δp_x^+ and $\Delta u_{\tau,x}^+$. The uncertainty of u_τ is assumed to be moderately small due to the moderate value of $\Delta p_x^+ < 0.005$. However, there could arise an additional uncertainty in u_τ due to missing Pitot tube corrections, which we infer from Bailey et al. [2013]. Regarding the remaining differences beween the profiles, a possible reason is that there are still small history effects in the inner layer and higher order effects, e.g., possibly involving $\mathrm{d}^2 P_\mathrm{w}/\mathrm{d}x^2$. Another possible reason are effects of the outer layer, which is much more influenced by history effects than the inner layer. Moreover, there can be small effects of flow details, which contribute to the remaining differences, e.g., possible three-dimensional effects of the wind-tunnel side walls, and effects of the Reynolds number, which is possibly not large enough in the asymptotic sense.

8.5.2 Results for moderately large values of the pressure gradient parameter

Then we consider different velocity profiles for $\Delta p_x^+ \approx 0.01$, which are summarised in table 8.2. In figure 8.5 (a) we show profiles for similar values of $\Delta u_{\tau,x}^+$, and in figure 8.5 (b) for different values of $\Delta u_{\tau,x}^+$. We note that for the present data at $U_\infty = 36\,\mathrm{m/s}$ we show $u^+(y^+)$ using the Clauser chart method for u_τ. The uncertainty of u_τ is moderately small for $\Delta p_x^+ \approx 0.01$, and, more importantly, the profiles of the data-base also use an indirect method for u_τ. We find that the present data are close to the profile ID 2134 by Schubauer & Klebanoff. Both flows have similar values for Δp_x^+ and $\Delta u_{\tau,x}^+$. The profile ID 2135 is for a little larger value of Δp_x^+ and shows a little larger upward turn above the log-law. The agreement with the profile ID 4505 by Schubauer & Spangenberg, which is at similar values for Δp_x^+ and $\Delta u_{\tau,x}^+$, is also close, albeit this flow is at a smaller Re_θ. On the other hand, in the outer layer for $y > 0.15\delta_{99}$, the velocity profile for the present flow looks clearly different compared to the profiles by Schubauer & Klebanoff. A possible explanation for this is that the relaxation time is much longer in the outer layer than in the inner layer. Therefore the differences in the outer layer of the mean-velocity profiles are supposed to be due to the long-living effects of flow history of the region of curvature and the streamwise changing pressure gradient.

The role of different values of the parameter $\Delta u_{\tau,x}^+$ is studied in figure 8.5 (b). We use the flow data by Clauser and by Skare & Krogstad, see table 8.3. The flows by Clauser and by Skare & Krogstad are close to equilibrium, and the values for $\Delta u_{\tau,x}^+$ are smaller than for the other flows shown in figure 8.5 (a). We observe that the velocity profiles for the two equilibrium flows are

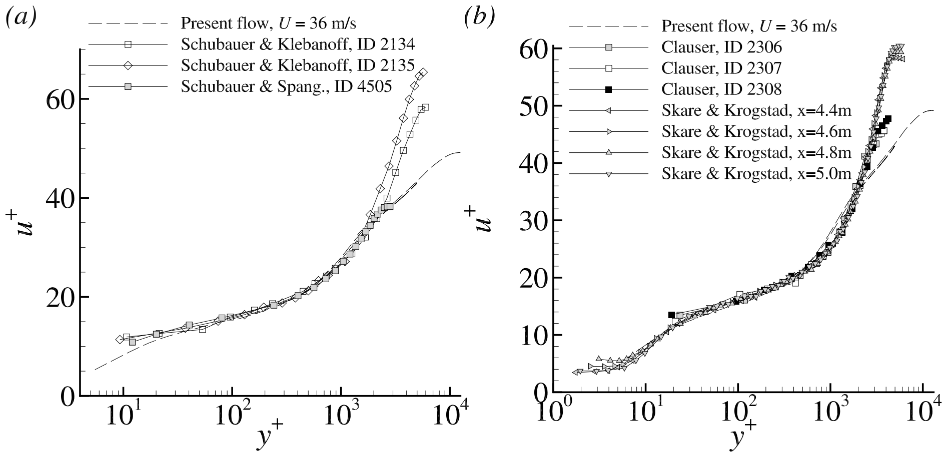

Figure 8.5: (a) Comparison of the present flow at $x = 9.944\,\mathrm{m}$ for $U_\infty = 36\,\mathrm{m/s}$ and different flows at similar values of Δp_x^+ and $\Delta u_{\tau,x}^+$, see table 8.2. (b) Comparison with flows at different values of $\Delta u_{\tau,x}^+$, see table 8.3.

Author	ID	x	Re_θ	Δp_x^+	$\Delta u_{\tau,x}^+ \times 10^5$	β_{RC}	H_{12}
Clauser	2306	19.17 ft	20917	0.0103	−0.774	8.70	1.766
Clauser	2307	23.92 ft	26438	0.0119	−1.10	12.07	1.757
Clauser	2308	26.67 ft	31018	0.0142*	−1.43*	16.28	1.758
Skare & Krogstad		4.4 m	44420	0.0130	−0.448	19.6	1.989
Skare & Krogstad		4.6 m	46250	0.0129	−0.641	20.1	1.998
Skare & Krogstad		4.8 m	49180	0.0123	−0.614	20.2	1.994
Skare & Krogstad		5.0 m	50980	0.0124	−0.734	21.2	1.998

Table 8.3: Summary of boundary layer parameters for flows close to equilibrium at moderately strong Δp_x^+-values.

close to each other. The region occupied by the log-law appears to be larger for the equilibrium flows with their smaller magnitude of $\Delta u_{\tau,x}^+$. For the non-equilibrium flows in table 8.2, the extent of the log-law fit region is smaller. This figure shows that we cannot expect similar mean velocity profiles in the inner layer for the same value of Δp_x^+, if the values for $\Delta u_{\tau,x}^+$ are significantly different.

We remark that there is possibly a considerable uncertainty of u_τ and $\mathrm{d}u_\tau/\mathrm{d}x$ for the flow ID 2300 by Clauser. The mean velocity profiles provide only three data points in the logarithmic region and are effected by measurement uncertainties. Moreover, it seems difficult to determine $\mathrm{d}u_\tau/\mathrm{d}x$ accurately, in particular for station ID 2308, see p. 213 in Coles and Hirst [1969]. Therefore the corresponding values for ID 2308 are marked with an asterix in table 8.3.

8.6 Summary

From the analysis of a large number of adverse pressure gradient turbulent boundary layer flows, we show indications for similarity of the mean velocity profiles, where the leading order similarity parameters are Δp_x^+ and $\Delta u_{\tau,x}^+$. The form of the mean velocity profile is composite with a thin log-law region and a sqrt-law region above. Noteworthy, the similarity is despite the differences in the upstream history of the flows considered. The APG flows of the literature data base evolve on a flat plate, whereas the present flow is subjected to strong curvature, relaxation from curvature on a flat plate, and a streamwise changing pressure gradient from favourable to adverse upstream of the APG focus region. The role of the upstream history will be studied in the next section.

Chapter 9

Streamwise evolution of the flow

The aim of this section is to assess possible higher order effects, e.g., history effects due to curvature and relaxation from curvature on a flat plate, which are neglected by the simple model based on Δp_x^+ and $\Delta u_{\tau,x}^+$. We attempt to describe the response time of the flow and the corresponding streamwise travelling distance by considering the eddy turnover time. Then we study the small details of the mean velocity profile in the region $y^+ < 150$ for the present flow and different flows from the literature data base to assess the role of possible higher order effects of the flow history and of the Reynolds number.

We consider the streamwise evolution of the flow using the results of the large-scale 2D2C PIV overview measurement. The profiles for the mean-velocity and for the Reynolds stresses were extracted at different streamwise positions along wall-normal lines in a wall-fitted coordinate system with wall-normal direction y. The streamwise positions of the profiles are given in table 9.1 and in table 9.2.

Therein we define the streamwise distance $x^*_{\mathrm{curv}} = (x - x_b)/\delta_{99,\mathrm{ref}}$ from the begin of curvature at $x_b = 8.990\,\mathrm{m}$ as a multiple of $\delta_{99,\mathrm{ref}}$. Moreover we define the streamwise distance of flow relaxation downstream of the end of curvature $x^*_{\mathrm{relax}} = (x - x_e)/\delta_{99,\mathrm{apg}}$, which is measured from the end of curvature at $x_e = 9.750\,\mathrm{m}$. The latter is expressed as a multiple of the reference boundary layer thickness $\delta_{99,\mathrm{apg}}$ in the adverse pressure gradient region, taken at $x = 9.72\,\mathrm{m}$.

x in m	8.12	8.37	8.62	8.87	9.12	9.32	9.42	9.52
x^*_{curv}	-5.80	-4.14	-2.47	-0.80	0.86	2.20	2.86	3.53
x^*_{relax}	-	-	-	-	-	-	-	-
$100\Delta p_x^+$	-0.015	-0.025	-0.046	-0.095	-0.17	0.037	0.20	0.49
β_{RC}	-0.15	-0.27	-0.52	-1.08	-1.74	0.29	1.50	4.30
$\frac{100\delta_{99,\mathrm{ref}}}{R_c}$	-	-	-	-	4.3	7.4	7.3	6.1

Table 9.1: Positions for the mean-flow profiles from the 2D2C PIV overview measurement. The values are for the case $U_\infty = 23\,\mathrm{m/s}$ using the values for u_τ obtained by OFI (Part 1).

x in m	9.72	9.87	9.944	10.02	10.09
x^*_{curv}	4.86	-	-	-	-
x^*_{relax}	-0.20	0.70	1.14	1.59	2.00
$100\Delta p_x^+$	1.34	1.57	1.85	2.26	2.75
β_{RC}	14.2	17.7	24.9	33.9	44.5
$\frac{100\delta_{99,\text{ref}}}{R_c}$	0.65	-	-	-	-

Table 9.2: Positions for the mean-flow profiles from the 2D2C PIV overview measurement. The values are for the case $U_\infty = 23\,\text{m/s}$ using the values for u_τ obtained by OFI (Part 2).

We found $\delta_{99,\text{apg}} = 0.17\text{m}$ for the case $U_\infty = 23\,\text{m/s}$. Moreover we include the values for the pressure gradient parameter in inner scaling Δp_x^+ and in the Clauser-Rotta scaling β_{RC} using the value for u_τ obtained by OFI. Finally we include the values for $\delta_{99,\text{ref}}/R_c$.

9.1 Mean velocity

9.1.1 Results

For the mean velocity, we consider the 2D2C PIV data evaluated by the single-pixel ensemble correlation method for the case $U_\infty = 23\,\text{m/s}$. The profiles are scaled to viscous units using u_τ from OFI. First we consider the change from zero to a favourable pressure gradient and the begin of curvature, see figure 9.1 (a). We use the profile at $x = 8.12\,\text{m}$ as the reference. We also include the log-law with $\kappa = 0.390$ and intercept $B = 4.07$, obtained by a least squares fit of the log-law to the data. Note that we write $\kappa = 0.39$ and $B = 4.1$ in the figures. We remark that the flow at the ZPG reference stations shows history effects due to the accelerating ramp, as discussed in section 5. The favourable pressure gradient is increasing at $x = 8.62\,\text{m}$ and we observe a downward shift of $\Delta u^+ = 0.4$ compared to $x = 8.37\,\text{m}$ (not shown). At $x = 8.87\,\text{m}$ the velocity profiles still show a log-law region, where slope and intercept are unchanged compared to $x = 8.62\,\text{m}$. The height of the wake is decreasing in streamwise direction.

As curvature effects and the favourable pressure gradient become stronger at $x = 9.12\,\text{m}$, the extent of the log-law region is reduced to $y^+ < 400$. Above $y^+ = 400$, the velocity profile, plotted against $\log(y^+)$, turns downwards below the log-law and then upwards at around $y^+ = 1400$ corresponding to $y/\delta_{99} = 0.14$. Above this upward turn, a second log-law region seems to appear with κ close to 0.4 and at a reduced intercept. The height of the wake is reduced significantly compared to $x = 8.87\,\text{m}$. The profile at $x = 9.12\,\text{m}$ shows features which are a combination of two effects, i.e., a favourable pressure gradient and convex curvature, which will be discussed in the following section.

In the curvature region, the pressure gradient changes from favourable to adverse. The magnitude of the adverse pressure gradient in terms of Δp_x^+ and β_{RC} is increasing in streamwise direction. The value of $u^+(100)$ being the value of u^+ at $y^+ = 100$ remains almost unaltered, see figure 9.1 (b), but the profiles do not follow the log-law up to $y^+ = 400$. Instead, they begin to turn

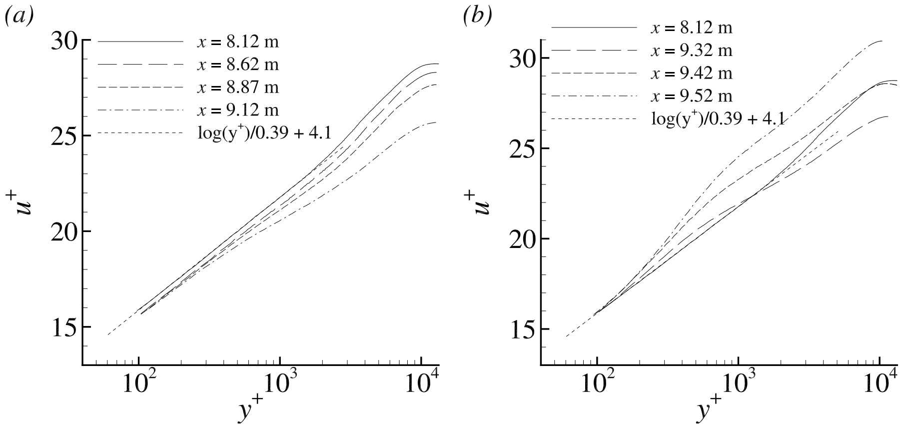

Figure 9.1: Mean velocity profiles for $U_\infty = 23\,\mathrm{m/s}$ at almost zero pressure gradient and in the region of curvature with change from favourable to adverse pressure gradient.

upwards above the log-law and make an S-shaped bending, if plotted against $\log(y^+)$. The spurious upward turn above the log-law appears at $x = 9.42\,\mathrm{m}$ where Δp_x^+ reaches a moderate value. Above this bending, a second log-law region appears whose slope is close to the value of $\kappa = 0.4$ and whose intercept is increasing in streamwise direction. The y^+-value of the outer edge of the second log-law region is decreasing in streamwise direction and the extent of the wake-region increases. The height of the wake becomes more pronouned in streamwise direction.

Downstream of the end of curvature at $x = 9.750\,\mathrm{m}$, the flow is subjected to two effects simultaneously, i.e., an adverse pressure gradient and relaxation from curvature. The results are shown in figure 9.2 (a). The value for $u^+(100)$ appears to be still almost unchanged. The upward turn above the log-law is increasing. The extent of the y^+-region where the velocity profile shows this upward turn is increasing in streamwise direction. Above this region, the profile turns back and a second log-law region can still be observed. The slope of the second log-law is increasing in downstream direction.

The mean velocity profiles in the region of the largest Δp_x^+-values are shown in figure 9.2 (b). The pressure gradient parameter Δp_x^+ is increasing in streamwise direction. The value for $u^+(100)$ is decreasing and the profiles for u^+ appear to be shifted downwards below the log-law observed at $x = 8.12\,\mathrm{m}$. A thin inner logarithmic region appears to recover as the flow relaxes from curvature. Such a recovery of the log-law during flow relaxation was also observed for flows without a significant pressure gradient, as discussed in the next section. Above the thin log-law fit region, the velocity profiles turn upwards above the log-law. The upward turn, if plotted against $\log(y^+)$, is increasing in streamwise direction. The outer edge of this region is also increasing in terms of y^+ in streamwise direction. Above $y^+ > 1500$, the profiles turn back and the second log-law still can be observed.

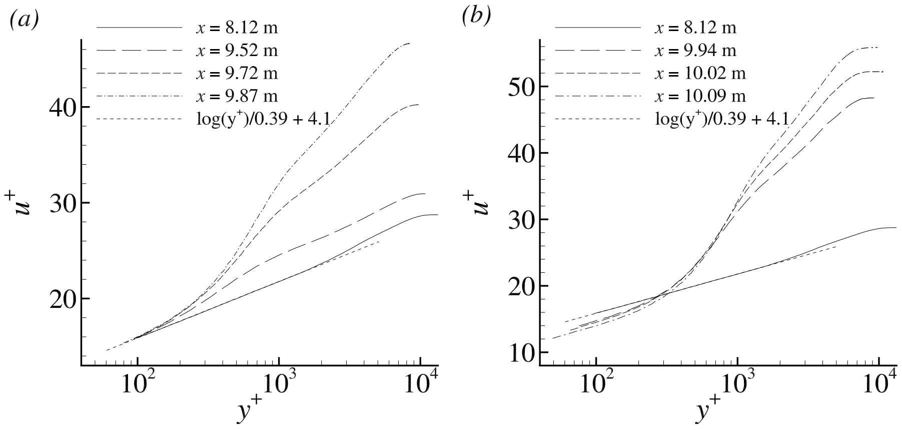

Figure 9.2: Mean velocity profiles for $U_\infty = 23\,\mathrm{m/s}$ in the adverse pressure gradient region.

	$\delta_{99,\mathrm{ref}}/R_c$	α_{curv}	$l_{\mathrm{curv}}/\delta_{99,\mathrm{ref}}$	$l_{\mathrm{relax}}/\delta_{99,\mathrm{ref}}$	$Re_{\theta,\mathrm{ref}}$
Smits et al. [1979]	0.167	30°	3	57	6000
Gillis & Johnston	0.05, 0.1	90°	16	21	3800
Alving et al. [1990]	0.08	90°	21	90	6000
Present flow	0.07	14.4°	5	2.4	12900, 24350

Table 9.3: Comparison with turbulent boundary layer flows with convex curvature and relaxation downstream on a flat plate at similar values of $\delta_{99,\mathrm{ref}}/R_c$ in the literature. For the present flow we include the cases $U_\infty = 10\,\mathrm{m/s}$ and $U_\infty = 23\,\mathrm{m/s}$.

9.1.2 Discussion

The present flow is subjected to a streamwise changing pressure gradient from favourable to adverse, convex curvature effects and relaxation on a flat wall. In table 9.3 we give some zero pressure gradient turbulent boundary layer flows subjected to convex curvature and relaxation at similar values of $\delta_{99,\mathrm{ref}}/R_c$. Among these cases, the flow by Smits et al. [1979] imposes an impulse-like sudden curvature over the shortest streamwise distance compared to the other cases.

As the flow enters the begin of the curvature region, the strongest effect is the favourable pressure gradient. The observed reduction of the wake contribution due to the favourable pressure gradient is in agreement with results e.g. for the sink-flow turbulent boundary layer by Jones et al. [2001]. Then the pressure gradient changes to adverse, and the increase of the wake parameter is again in agreement with previous findings in the literature.

In the convex curvature region, a reduction of the outer extent of the log-law region in conjunction with an upward turn of the velocity profile above the log-law starting below $y^+ = 100$ can be seen also for the data by Gillis and Johnston [1983] and Gillis et al. [1980], and in the work by Kim and Rhode [2000]. The upward turn is developing during the curvature section. Note that in Gillis and Johnston [1983] the Clauser chart method was used to determine u_τ. Some theoretical models have been proposed to describe the upward turn above the log-law due to convex curvature, see, e.g., Kim and Rhode [2000] and references therein. For the present flow, the upward turn above the log-law is stronger than for the zero pressure gradient cases. We suppose that it is the adverse pressure gradient who mainly alters the mean velocity profile and causes a sqrt-law behaviour.

The recovery of the log-law during relaxation on a flat wall was studied for the zero pressure gradient cases by Gillis et al. [1980], Smits et al. [1979] and Alving et al. [1990]. The upward turn of the velocity profile above the log-law is decreasing and the extent of the log-law is increasing in streamwise direction. In the outer layer, the relaxation of the mean velocity profile takes much longer than for the inner layer, see Gillis et al. [1980] and Alving et al. [1990]. The second log-law region can still be observed during the so-called early relaxation at $x^*_{\mathrm{relax}} = 4$ for the data in Gillis et al. [1980]. It can also be observed at $x^*_{\mathrm{relax}} = 0.8$ and $x^*_{\mathrm{relax}} = 4$ in figure 7 in Alving et al. [1990] and at $x^*_{\mathrm{relax}} = 1.3$ in figure 7 (d) for the flow by Smits et al. [1979]. We remark that the streamwise extent of the measurement region for relaxation is much longer in the zero pressure gradient cases than for the present flow. The combined effect of relaxation and adverse pressure gradient is more complex. The relaxation of the thin log-law region whose extent is slowly increasing in streamwise direction is attributed to the end of curvature, whereas the strong upward turn above the log-law is attributed to the adverse pressure gradient and the sqrt-law behaviour up to $y^+ = 0.12\delta^+_{99}$.

Regarding the phenomenon of a double log-layer, Spalart [2010] uses a theoretical model and RANS simulations to describe that this can be caused by a sudden change of u_τ over a short time. Then, inside the inner layer, the internal boundary layer yields a different slope of $\mathrm{d}u^+/\mathrm{d}y^+$ than for the layer above whose vorticity is conserved along streamlines, see figure 1 therein. Internal layers can grow if the flow is subjected to an abrupt change of pressure gradient and/or surface curvature, see Baskaran et al. [1987]. They performed experiments for a wall mounted curved hill with an abrupt change in curvature and a free wing based on the same convex curvature geometry. They describe that an abrupt change in surface curvatures initiates the growth of an internal boundary layer. In the free-wing experiment the effect of the pressure gradient was found to dominate the effect of mild convex curvature, where δ_{99}/R_c was smaller than 0.012. Bandyopadhyay and Ahmed [1993] designed a flow experiment with an abrupt change of curvature and pressure gradient. They report that for their experiment the effect of curvature dominates the accompanying changes of the pressure gradient, where δ_{99}/R_c was in the range 0.04 to 0.065. For the present flow the curvature perturbation parameter Δk^* was smaller than the threshold value of $\Delta k^* \approx 3.7 \times 10^{-5}$ reported by Bandyopadhyay and Ahmed [1993], see section 4. For the present flow, the "dip" below the log-law, using the word by Baskaran et al. [1987], and the change of the log-law slope in the second log-law region are much less pronounced than for the flow by Baskaran et al. [1987].

9.2 Reynolds stresses

9.2.1 Results

We consider the results for the Reynolds stresses for the case $U_\infty = 10\,\mathrm{m/s}$ evaluated using the window-correlation method. The resolution of the wall-normal fluctuation $\overline{v'^2}$ was found to determine the resolution requirements for the window-correlation method. The results for the position at almost zero pressure gradient at $x = 8.12\,\mathrm{m}$ show good agreement with hot-wire reference data at similar Reynolds numbers in the literature. The Reynolds stresses are made non-dimensional using the reference velocity $U_{\mathrm{ref}} = 10\,\mathrm{m/s}$. The wall-distance is scaled using the local boundary layer thickness δ_{99}.

We remark two issues before proceeding. First, for the determination of the boundary layer thickness we use the relatively simple method described in section 3.3. The aim of this section is to study the effect of curvature and pressure gradient on the magnitude of the Reynolds stresses. For a detailed characterisation in the outer part of the boundary layer, more sophisticated methods for the boundary layer edge are needed, see , e.g., Vinuesa et al. [2016]. The second issue concerns the use of the Reynolds decomposition for the computation of the mean flow and fluctuation statistics, as described in Kwon et al. [2016]. In the present work we use an unconditional average, i.e., an average over all instantaneous data. This can be justified for the inner part of the boundary layer, where the flow is fully turbulent. However, in the outer region, the flow is intermittently turbulent. Recently, new decompositions were proposed to ensure that non-turbulent regions in the flow do not contaminate the fluctuating velocity components in the turbulent regions, see, e.g., Kwon et al. [2016] and Reuther and Kähler [2019]. Such a method involves the problem to determine the turbulent/non-turbulent interface, see, e.g., Vinuesa et al. [2016], Chauhan et al. [2014b,a], Reuther and Kähler [2018, 2019]. Here we are only interested in the qualitative behaviour of the Reynolds stresses during the flow evolution. Due to the open questions of more sophisticated Reynolds decomposition methods, we use the traditional unconditional method.

The evolution of the Reynolds stresses from the zero pressure gradient region into the curvature region is considered first. The normal stresses are shown in figure 9.3 (a) and (b). The flow acceleration causes a reduction of $\overline{u'^2}$ and $\overline{v'^2}$ in the inner 50% of the boundary layer at $x = 8.87\,\mathrm{m}$. Then the convex curvature and the favourable pressure gradient cause a further reduction of $\overline{u'^2}$ and an even larger reduction of $\overline{v'^2}$ at $x = 9.32\,\mathrm{m}$ in the inner 50% of the boundary layer. As the pressure gradient changes from favourable to adverse, $\overline{u'^2}$ starts to increase whereas $\overline{v'^2}$ still decreases for $y < 0.5\delta_{99}$. The increase in $\overline{u'^2}$ and $\overline{v'^2}$ in the outer layer at $x = 9.32\,\mathrm{m}$ and $x = 9.42\,\mathrm{m}$ could be in parts due the effect of the meandering Görtler vortices, and could also be effects by details of the data evaluation at the turbulent/non-turbulent interface, see Reuther and Kähler [2018], Reuther and Kähler [2019].

The Reynolds shear stress $\overline{u'v'}$ and the correlation coefficient are shown in figure 9.3 (c) and (d). The favourable pressure gradient causes a small reduction of $-\overline{u'v'}$ from $x = 8.12\,\mathrm{m}$ to $x = 8.87\,\mathrm{m}$ for $y/\delta_{99} < 0.3$. In the curvature region, $-\overline{u'v'}$ is strongly decreasing, in particular from $x = 9.32\,\mathrm{m}$ to $x = 9.42\,\mathrm{m}$, despite the increasing adverse pressure gradient. The correlation coefficient $\overline{u'v'}/(u'_{\mathrm{rms}}v'_{\mathrm{rms}})$ gives values around 0.38 in the inner layer at $x = 8.12\,\mathrm{m}$, which

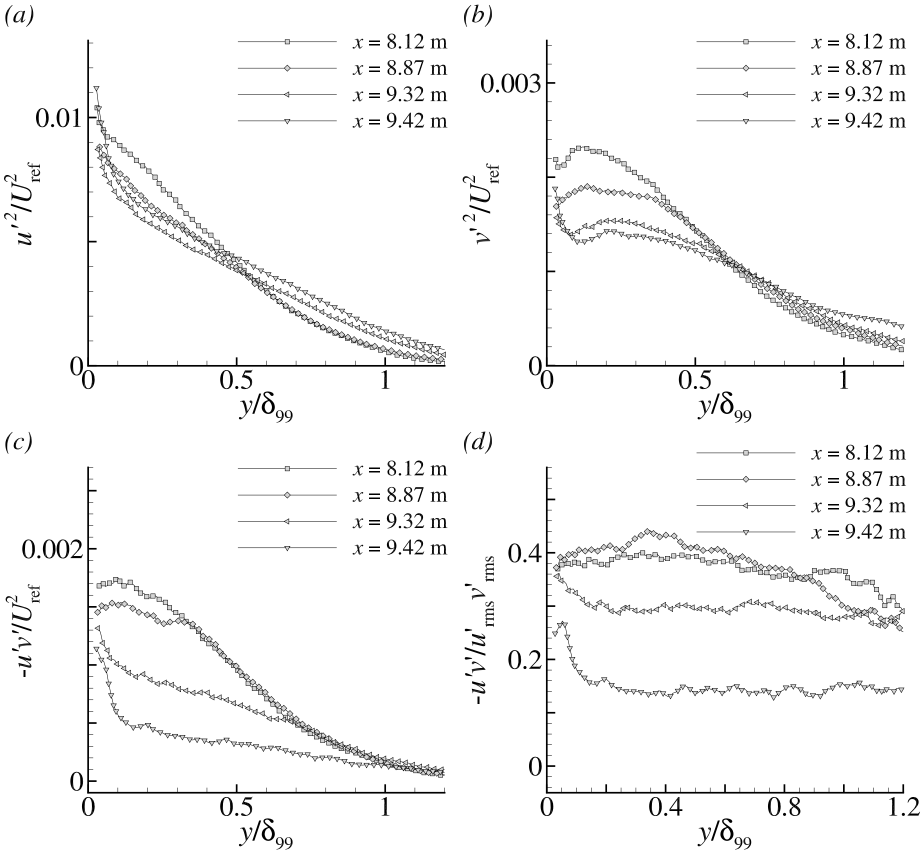

Figure 9.3: Streamwise evolution of Reynolds stresses and correlation coefficient from the region of almost zero pressure gradient to the region of curvature and change from favourable to adverse pressure gradient for $U_\infty = 10\,\mathrm{m/s}$.

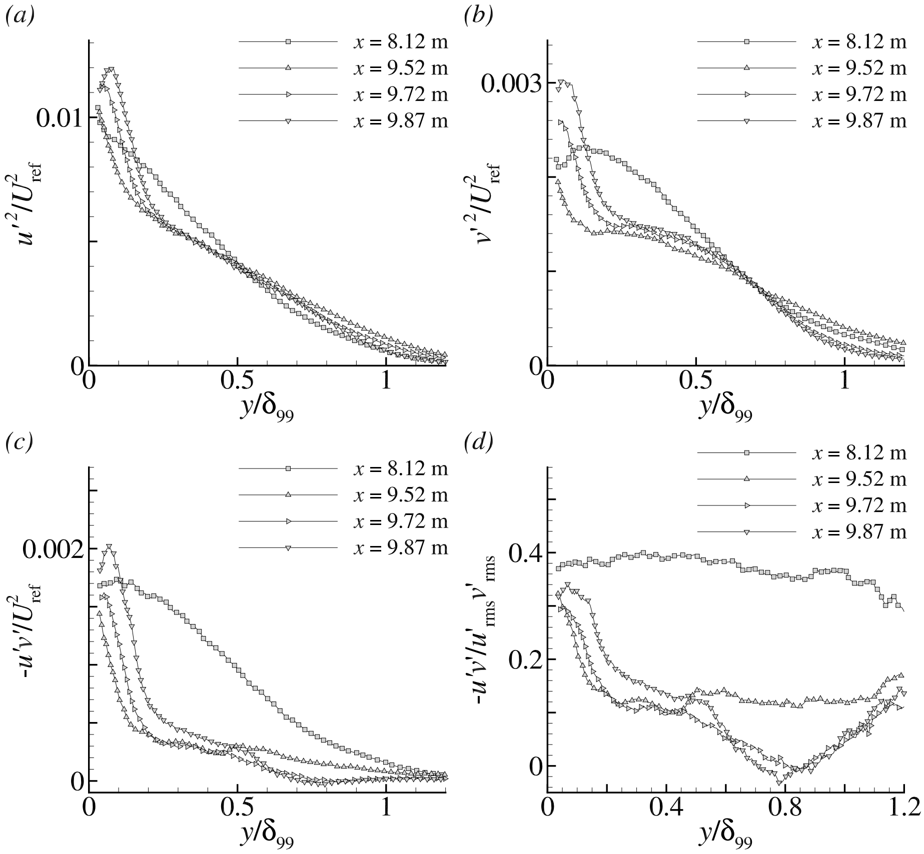

Figure 9.4: Streamwise evolution of Reynolds stresses and correlation coefficient in the region of curvature and relaxation at adverse pressure gradient for $U_\infty = 10\,\mathrm{m/s}$.

is comparable to experiments in the literature at similar Re_θ. Albeit the coefficient cannot be expected to be constant across the inner layer nor independent of the Reynolds number, see Marusic et al. [2013], it could give some valuable indications about the turbulence structure and departure from equilibrium, see Gungor et al. [2014]. At $x = 9.32\,\mathrm{m}$ and at $x = 9.42\,\mathrm{m}$, we observe that the correlation coefficient is significantly reduced for $y/\delta_{99} > 0.1$.

During the second part of the curvature region and the relaxation on the inclined flat wall, the flow experiences an adverse pressure gradient. For $\overline{u'^2}$ and $\overline{v'^2}$ we observe an increase in the inner region for $y/\delta_{99} < 0.2$ and a new inner maximum forms at around $y/\delta_{99} \approx 0.072$ at $x = 9.87\,\mathrm{m}$, see figure 9.4 (a). The streamwise increase of $\overline{v'^2}$ is larger than for $\overline{u'^2}$, see figure 9.4 (b). The maximum of $\overline{u'^2}$ and $\overline{v'^2}$ is larger than at the position of almost zero pressure gradient. In the outer part, for $y/\delta_{99} > 0.7$, the changes compared to $x = 9.52\,\mathrm{m}$ could be attributed again to the effect of the meandering longitudinal vortices and the data evaluation at the turbulent/non-turbulent interface.

The Reynolds shear stress is increasing significantly in the region $y/\delta_{99} < 0.2$ from $x = 9.52\,\mathrm{m}$ to $x = 9.87\,\mathrm{m}$ and a new inner maximum appears at

$y/\delta_{99} \approx 0.07$ for $x = 9.87\,\mathrm{m}$, see figure 9.4 (c), whereas the increase is much slower further away from the wall for $0.2 < y/\delta_{99} < 0.5$. In the outer part, for $y/\delta_{99} > 0.7$ we observe a further reduction of $-\overline{u'v'}$, ceasing to almost zero in this region with small negative values for $x = 9.87\,\mathrm{m}$. The correlation coefficient is increasing in the inner 20% of the boundary layer after the end of curvature, see figure 9.4 (d). Further away from the wall, for $0.2 < y/\delta_{99} < 0.6$, the increase is slower and starts from a much smaller level reached at $x = 9.52\,\mathrm{m}$. In the outer layer for $y/\delta_{99} > 0.7$ the correlation coefficient is still decreasing in streamwise direction. The results near and above the boundary layer edge are supposed to be affected by measurement uncertainties and numerical errors.

Further downstream in the adverse pressure gradient region on the inclined flat plate, $\overline{u'^2}$, $\overline{v'^2}$ and $-\overline{u'v'}$ are still increasing for $y < 0.3\delta_{99}$, whereas the increase is small for $0.3 < y/\delta_{99} < 0.6$, see figure 9.5 (a) - (c). The correlation coefficient appears to recover on the inclined flat wall in streamwise direction and could exhibit a small overshoot during relaxation at $x = 10.17$m, but this is not clear due to the uncertainty of the data, see figure 9.5 (d). The extent of the region where the correlation coefficient becomes close to 0.4 is increasing in streamwise direction and a level similar to $x = 8.12\,\mathrm{m}$ is reached for $y < 0.11\delta_{99}$ at $x = 9.94\,\mathrm{m}$ and for $y < 0.25\delta_{99}$ at $x = 10.17$m. Above $y > 0.3\delta_{99}$ the correlation coefficient is still much smaller than for $x = 8.12\,\mathrm{m}$.

For comparison, we show the 3D LPT STB results for $U_\infty = 36\,\mathrm{m/s}$ in figure 9.6. The Reynolds stresses are shown in figure 9.6 (a) and we note that $\delta_{99}^+ = 10530$. The correlation coefficient and the anisotropy coefficient are shown in figure 9.6 (b). For the correlation coefficient, the maximum value is around 0.338. For the Bradshaw anisotropy ratio $a_{12} = \left|\overline{u'v'}\right|/k$ with $k = 0.5(\overline{u'^2} + \overline{v'^2} + \overline{w'^2})$ we find a maximum value of around $a_{12} = 0.208$.

9.2.2 Discussion

A common feature of turbulent boundary layers subjected to strong convex curvature ($\delta_{99}/R_\mathrm{c} > 0.05$) is the strong reduction of the magnitude of the Reynolds shear stress $\overline{u'v'}$ in the outer part of the boundary layer for $y > 0.3\delta_{99}$ and even below, see Gillis and Johnston [1983]. The results in figure 9.3 (c) and in figure 9.4 (c) can be compared with figure 2 in Gillis and Johnston [1983]. Therein a qualitatively similar behaviour can be observed for the station at $x^*_\mathrm{curv} = 2.3$ and a turn angle of 13°, whereas for $x^*_\mathrm{curv} = 5.6$ and a turn angle of 30° already significant negative values for $-\overline{u'v'}$ are observed for $y > 0.4\delta_{99}$, which cannot be found for the present flow.

The relaxation of the turbulence quantities is more complex than for the mean flow and occurs in several stages. Alving et al. [1990] report that, during relaxation, the stress levels rise to higher values than upstream of curvature, and the ratios of the Reynolds stresses are found to be distorted. Qualitatively similar results are described in Gillis and Johnston [1983], albeit their measurements are only for the initial stage of recovery ($x_\mathrm{relax} \leq 21\delta_{99}$). Values for $-\overline{u'v'}$ of up to $1.25u_\tau^2$ are shown in figure 19 in Gillis and Johnston [1983] and are observed even for the last measurement position at $x^*_\mathrm{relax} = 21$. The overshoot shown for $x^*_\mathrm{relax} = 0.8$ in figure 13 (a) in Alving et al. [1990] is little larger. For the present flow, the relaxation on the inclined flat plate is superposed by the adverse pressure gradient. The maximum of $-\overline{u'v'}$ is increasing in streamwise direction and the elevation above the upstream level is larger than for the flow

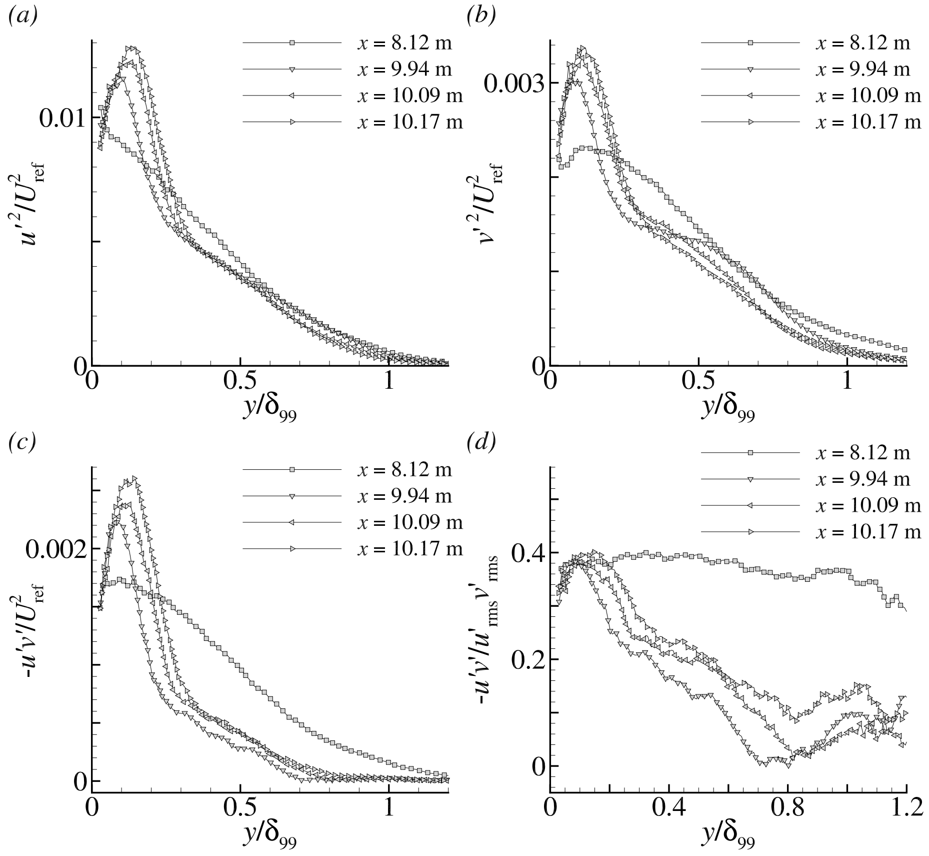

Figure 9.5: Streamwise evolution of Reynolds stresses and correlation coefficient in the adverse pressure gradient region on the inclined flat plate for $U_\infty = 10\,\mathrm{m/s}$.

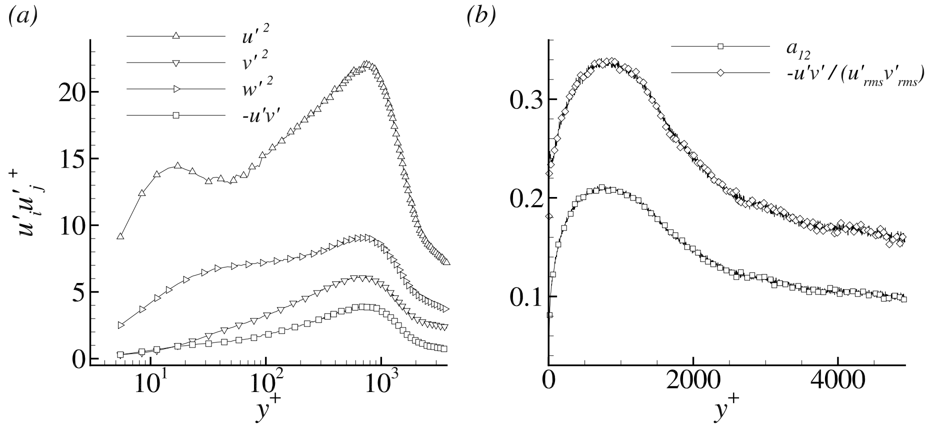

Figure 9.6: 3D LPT STB data for $U_\infty = 36\,\mathrm{m/s}$ at $x = 9.944\,\mathrm{m}$. (a) Reynolds stresses and (b) correlation coefficient and anisotropy coefficient.

by Gillis and Johnston [1983], which is attributed to the adverse pressure gradient. The role of small details of the present flow compared to the reference flows in table 9.3 remain unanswered. The first difference is that the curvature of the present geometry is continuous and joins smoothly the inclined flat plate in constrast to the reference flows. The second difference is that the turning angle before relaxation is only 14.4°.

Gillis and Johnston [1983] also report a small overshoot in the structural parameter a_{12} compared to the values upstream of curvature for $y < 0.3\delta_{99}$ for their measurement station 12 at $x^*_{\mathrm{relax}} = 4$ during relaxation. In the present experiment, a small overshoot of the correlation coefficient compared to the value at $x = 8.12\,\mathrm{m}$ might be seen for the most downstream position at $x = 10.17\mathrm{m}$ (or $x^*_{\mathrm{relax}} \approx 2.5$), but this could be influenced by uncertainties in the measurement. The 3D LPT STB results for $U_\infty = 36\,\mathrm{m/s}$ indicate a significant reduction of a_{12} at $9,944\,\mathrm{m}$.

9.3 Relaxation and history effects

On the inclined flat plate for $x > 9.75\,\mathrm{m}$, the relaxation of curvature is superimposed by the adverse pressure gradient. We study the eddy turnover time $\tau_{\mathrm{t.o.}}$ to estimate the relaxation of history effects, motivated by the work in Wilcox [1998] and Sillero et al. [2013]. Two definitions for $\tau_{\mathrm{t.o.}}$ are considered. The first definition is based on the turbulent shear stress $|\overline{u'v'}|$

$$\tau_{\mathrm{t.o.}} = \kappa_0 * y / |\overline{u'v'}|^{1/2} \tag{9.1}$$

with $\kappa_0 = 0.41$. The second definition is based on the turbulent kinetic energy k

$$\tau_{\mathrm{t.o.}} = \kappa_0 * y / k^{1/2} \tag{9.2}$$

with $k = \overline{u'^2} + \overline{v'^2} + \overline{w'^2}$. Since the 2D2C PIV method only provides $\overline{u'^2}$ and $\overline{v'^2}$, we use the approximation $\overline{w'^2} = 1.3\overline{v'^2}$. The results are shown in figure 9.7 for (9.1) and in figure 9.8 for (9.2), both for the case $U_\infty = 10\,\mathrm{m/s}$. Therein the turnover length $\delta_{\mathrm{t.o.}} = U\tau_{\mathrm{t.o.}}$ is the corresponding streamwise travelling distance of the local mean flow $U(y)$, see Sillero et al. [2013]. Following this work, the flow is assumed to relax to equilibrium after $2\tau_{\mathrm{t.o.}}$.

The values for the turnover length based on $|\overline{u'v'}|$ are larger than based on k. As an estimate for the turnover length we obtain $2\delta_{\mathrm{t.o.}} \approx 2.4\delta_{99,\mathrm{ref}}$ for $\tau_{\mathrm{t.o.}}$ based on $|\overline{u'v'}|$, and $2\delta_{\mathrm{t.o.}} \approx 0.9\delta_{99,\mathrm{ref}}$ for $\tau_{\mathrm{t.o.}}$ based on k, evaluated at a wall-distance of $y = 0.1\delta_{99}$ for the position $x = 9.72\,\mathrm{m}$. Closer to the wall, at $y = 0.05\delta_{99}$, the corresponding values are $2\delta_{\mathrm{t.o.}} \approx 0.4\delta_{99,\mathrm{ref}}$ and $2\delta_{\mathrm{t.o.}} \approx 0.18\delta_{99,\mathrm{ref}}$. This indicates that the near-wall flow relaxes rapidly, but not instantaneously. Indeed, we observe a recovery of the log-law region for $x \geq 9.94\,\mathrm{m}$, which is $1.5\delta_{99}$ downstream of the end of curvature. As the Reynolds stresses are increasing due to the adverse pressure gradient, the turnover length is decreasing in streamwise direction in the inner part of the boundary layer.

In the outer part of the boundary layer, the turnover length is strongly increasing for $y > 0.15\delta_{99}$. We observe values for $2\delta_{\mathrm{t.o.}}$ up to $16\delta_{99,\mathrm{ref}}$ (based on k) and up to $50\delta_{99,\mathrm{ref}}$ (based on $|\overline{u'v'}|$) at a wall-distance of $y = 0.6\delta_{99}$, due to the significant reduction of the Reynolds stresses and in particular of the shear

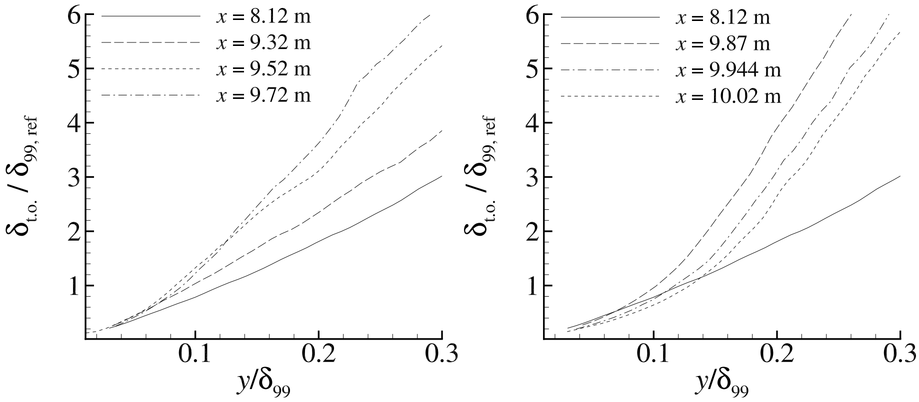

Figure 9.7: Estimation of history effects using the turnover length based on equation (9.1) for the case $U = 10\,\mathrm{m/s}$.

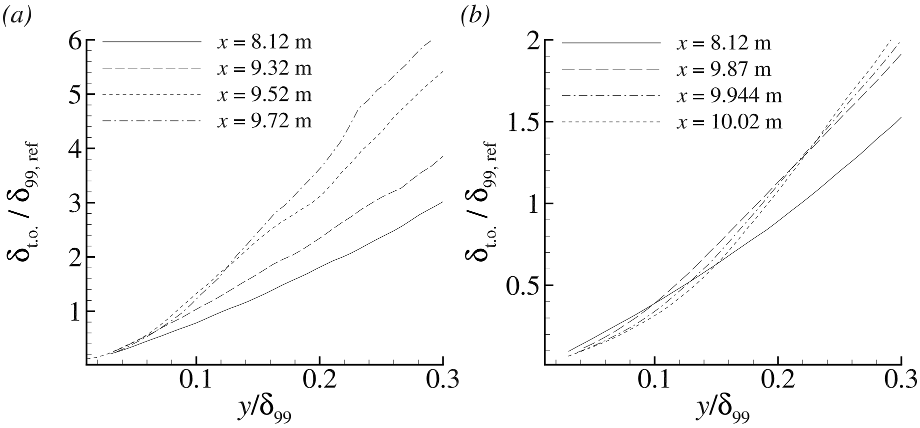

Figure 9.8: Estimation of history effects using the turnover length based on equation (9.2) for the case $U = 10\,\mathrm{m/s}$.

stress in the convex curvature region and the slow recovery of the Reynolds stresses in the outer part of the boundary layer.

9.4 Discussion of adverse pressure gradient and history effects

In this section, we study the mean velocity profile in the region $y^+ < 150$ is detail. The aim is to discuss the role of possible additional effects, which are neglected in the simple model, e.g., history effects due to the upstream region of curvature, relaxation from curvature on the flat wall, and Reynolds number effects. We compare the μPTV data at $\Delta p_x^+ = 0.0182$ with some literature data, which are at a similar value of Δp_x^+. We use the data at $x/\delta_0 = 15.6$ by Manhart and Friedrich [2002] with $\Delta p_x^+ = 0.0186$, the data at $x/Y = -5$ for case C by Coleman et al. [2018] with $\Delta p_x^+ = 0.017$, and the data at $x = 0.723\,\mathrm{m}$

by Nagano et al. [1991] with $\Delta p_x^+ = 0.0188$ and $Re_\theta \approx 1900$. Therein δ_0 and Y denote the reference length used in the corresponding publications.

The first question is if there is a significant deviation of the mean velocity from the zero pressure gradient case, where we use the DNS data by Schlatter and Örlü [2010] as a reference. The second question considers the correlation (2.16) by Nickels [2004] and the correlation of $K_\mathrm{i} B_\mathrm{i}$ versus B_i proposed by Nagib and Chauhan [2008]. If both correlations hold simultaneously, then K_i and B_i would be determined by the local value of Δp_x^+. This would imply that the mean velocity profiles of different flows, but for the same value of Δp_x^+, should be close to each other at least in a small log-law fit region, provided that Re is large enough.

The results are shown in figure 9.9. To assess if the deviations are significant, we include the error bars. For the μPTV data we assume an estimated overall uncertainty in u^+ of 3.1%, with an uncertainty contribution of 2.1% for u_τ from OFI and an assumed uncertainty of 1% for U. Moreover we assume an uncertainty of 3.1% in y^+ due to the uncertainty in u_τ, in ν, and in the wall position. For the DNS data by Coleman et al. [2018], we include an error bar associated with an estimated uncertainty of 1% for u_τ, based on a personal communication by Coleman [2018]. The different curves are close to each other for $y^+ < 8$, and the curves start to deviate for $y^+ > 10$. A downward shift Δu^+ of the mean velocity profile in the log-law fit region can be observed for all profiles, but with a small variation. The downward shift is $\Delta u^+ = -0.6$ for the profile by Manhart and Friedrich [2002], and $\Delta u^+ = -0.3$ for the profile by Coleman et al. [2018]. A downward shift in the region $y^+ < 100$ can be observed also in figure 6 in Lee and Sung [2008] at $Re_\theta = 1350$, where the shift is increasing with an increasing value of β_RC, and in figure 6 in Bobke et al. [2017]. Moreover it can be observed for the Couette-Poiseuille flow by Coleman et al. [2015]. Therein, figure 8 gives an overview for the value of u^+ at $y^+ = 50$ for different flows in the literature.

The deviation between the μPTV data and the data by Coleman et al. [2018] in the near wall region cannot be explained alone by the uncertainty of each individual data-set. This brings up the question of additional flow parameters to explain this deviation. There are different possible parameters, which could give a contribution to the observed spreading of the mean velocity profiles. However, it is also possible that two effects counterbalance or cancel each other, suggesting a collapse of the data and masking differences.

The first aspect is the question of Reynolds number effects, which, for turbulent boundary layers at ZPG, can cause an upward shift, see Wei et al. [2005b]. However, this effect appears to be small if $Re_\theta > 1400$ in Wei et al. [2005b] and for the DNS data by Schlatter and Örlü [2010]. Moreover, effects related to the mesolayer could arise. The flow region corresponds to the y^+-regime of the mesolayer in ZPG boundary layers, see George and Castillo [1997]. We also remark a recent discussion on details of the near-wall mean-velocity profile at ZPG, e.g., the proposal to account for an observed overshoot above the log-law near $y^+ \approx 50$ by Chauhan et al. [2007].

Then there is the question if other, possibly higher order terms, with additional parameters besides Δp_x^+ and $\Delta u_{\tau,x}^+$ govern the near wall solution. We remark that the μPTV data and the profile by Coleman et al. [2018] are both for the same value of Δp_x^+ and of $\Delta u_{\tau,x}^+ = -6.44 \times 10^{-5}$. Another possible parameter is the coefficient of instantaneous backflow, see Alving and Fernholz

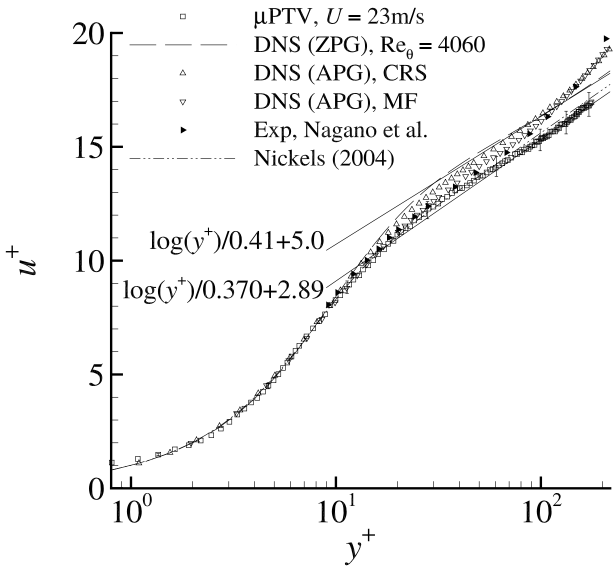

Figure 9.9: Mean velocity profiles for different flows at a streamwise position with $\Delta p_x^+ = 0.018 \pm 0.01$ using case C by Coleman et al. [2018] (CRS), Manhart and Friedrich [2002] (MF), Nagano et al. [1991], and the ZPG data by Schlatter and Örlü [2010].

[1995a] and Bross et al. [2019]. This could have an influence near separation, but the data considered are sufficiently far upstream from the position of incipient detachment (1% backflow).

Moreover there is the question if details of the flow in the outer part of the inner layer ($300 < y < 0.15\delta_{99}^+$) have an influence on the flow in the region $y^+ < 150$. This could be due to details of the mean velocity profile, e.g., the observed upward turn above the log-law in the sqrt-law region, which depends on Δp_x^+ and $\Delta u_{\tau,x}^+$.

Another question are long-living history effects, see, e.g., Marusic et al. [2015] and Schlatter and Örlü [2010] for the ZPG case. For the present μPTV data, possible long-living history effects are due to the flow acceleration over the first ramp with concave-convex curvature and possible Görtner vortices, and due to the convex curvature region for $x > 8.99$ m. On the convex wall, a deviation from the universal log-law in the inner layer and even below $y^+ < 200$ might be indicated by the 2D2C PIV data, but additional high resolution data could not be measured in this region. From the present data, the question of a possible change of the log-law slope coefficient K_i and intercept B_i caused by the convex curvature and a relaxation of K_i and B_i on the flat inclined plate cannot be answered. If we assume for a moment that the log-law intercept is reduced in parts due to history effects of the convex curvature region, then this would imply little larger values for B_i in the absence of the curvature region. This would shift the data closer to the correlation by Nagib and Chauhan [2008] in figure 6.4 (b).

From these considerations more open questions than answers arise. Despite these questions, the following conclusions are drawn. First, the present data are seen as an indication to support the reduction of the slope coefficient K_i in the log-law fit region caused by the adverse pressure gradient, as proposed by Nickels [2004]. However, the possibility that the observed reduction of K_i is, at least in parts, due to history effects of the convex curvature region, cannot be excluded due to the lack of data. Secondly, we tend to conclude that the log-law intercept is altered by the pressure gradient and influenced by small reminiscences of history effects.

9.5 Summary

The response time of the flow to streamwise changing flow conditions, e.g., the relaxation from curvature on the flat plate, is estimated using the eddy turn over time. The corresponding streamwise travelling distance of the mean flow is of the order of the local boundary layer thickness for the inner part of the boundary layer, i.e., the flow in the inner layer adjusts fast but not instantaneously. This indicates the possibility of small history effects. The comparison of the mean velocity profile of the present flow and the profiles of the literature data base at a similar value of Δp_x^+ and $\Delta u_{\tau,x}^+$ shows subtle, but clear, differences in the region $y^+ < 150$, see figure 9.9. This suggests that higher order effects are negleced by the simple model based on Δp_x^+ and $\Delta u_{\tau,x}^+$, e.g., due to details of the streamwise evolution of the flow. Moreover viscous effects associated with the mesolayer are not included in the model. Therefore, regarding the similarity of the mean velocity profile, we may conclude that the parameters Δp_x^+ and $\Delta u_{\tau,x}^+$ describe only the leading order effects.

Chapter 10

Conclusions

We presented an analysis of the inner layer of turbulent boundary layers at adverse pressure gradient. The goal was to determine the resilience of the log-law, the possible change of the log-law slope and the appearance of a square-root law above the log-law. For this purpose we performed a new wind-tunnel experimental of a turbulent boundary layer at adverse pressure gradient with effects of convex curvature and relaxation from curvature, and we analysed a data base from the literature.

The first conclusion concerns the measurement technique. We confirmed that the accuracy and uncertainty of the measurement technique becomes a critical issue for the study of wall-laws for the mean velocity and for the Reynolds stresses. High resolution particle tracking velocimetry (PTV) methods were shown to provide a substantial improvement compared to classical partical image velocimetry (PIV). Three-dimensional Lagrangian particle tracking (LPT) gave high resolution data for the mean velocity and for the Reynolds stresses from the viscous sublayer up to $0.4\,\delta_{99}$. Microscopic PTV (μPTV) gave high resolution data from the viscous sublayer up to $y^+ = 200$. We found that a high resolution method is needed to accurately determine the mean velocity gradient below $y^+ = 200$ to evaluate the log-law slope and the Reynolds stresses. A particular challenge remains to accurately measure the mean velocity profile in the viscous sublayer below $y^+ = 2.5$ and to determine the wall shear stress from the mean velocity profile in the viscous sublayer. Oil film interferometry was confirmed to be an important alternative to determine the wall shear stress at high Reynolds numbers.

The question of accuracy requirements for experimental data for wall laws, in particular for a possible change of the log-law slope, was also investigated. The major contribution to the overall uncertainty stems from the wall shear stress. In the present work we reached at best an overall relative uncertainty of 3% for u^+ vs. y^+. The comparison with other data from DNS and experiments suggested that a smaller uncertainty bound is needed for definite conclusions on a change of the log-law for moderately strong values of $\Delta p_x^+ = 0.02$ and below. Regarding the technical reasons for the uncertainty, it was found that near the wall, in particular for high *Re* flows with their very small viscous length scale, details of the particle tracking method become important, e.g., reflections of the laser light sheet at the wall, and the determination of the exact wall-position, confirming the results by Örlü et al. [2010]. For recent developments to improve the experimental accuracy, see Willert et al. [2018], Novara et al. [2019], and Bross et al. [2019].

In the adverse pressure gradient region, we found a composite form of the mean velocity profile in the inner layer, confirming an early proposal by Perry et al. [1966]. The composite profile was found to consist of a thin log-law region and a square-root law above the log-law up to $0.12\,\delta_{99}$. The square-root law was demonstrated by a plateau of the mean velocity slope diagnostic function. As the plateau was found to have only a moderate extent even for the large Reynolds number $Re_\theta = 57000$, we infer that the square-root law region appears only at sufficiently large Reynolds numbers. From this we conclude the need for high Reynolds number data for the study of wall-laws at adverse pressure gradients.

Regarding the resilience of the log-law and regarding the work by Nickels [2004], we found lower values for the log-law slope coefficient K_i in the adverse pressure gradient region than for the zero pressure gradient region. The log-law slope coefficient was found to be decreasing with increasing values of the pressure gradient parameter Δp_x^+. We found a value of $K_\mathrm{i} = 0.370 \pm 0.017$ for $\Delta p_x^+ = 0.018$. However, the reduction could not be demonstrated to be significant due to the measurement uncertainty, and because the question of possible history effects of the upstream located region of convex wall curvature could not be answered. We mention that the corresponding theoretically expected value of the log-law slope predicted by Nickels [2004] is $K_\mathrm{i} = 0.365$ for $\Delta p_x^+ = 0.018$. We also showed that using the value for u_τ from the Clauser chart gives erroneously smaller values for K_i than if a direct method of u_τ was used.

Then we studied an analytical model for the total shear stress in the inner layer, which was proposed by Coles [1955] and Perry et al. [1966]. Its parameters are the pressure gradient parameter and the wall shear stress gradient parameter. The model uses an approximation for the mean inertia effects, where we substituted the composite mean velocity profile. This model was found successful to describe the measured turbulent shear stress. This was seen as an indication that it not only the pressure gradient parameter, but also the local flow deceleration, which govern the turbulent shear stress. In particular, we found that the sqrt-law region for the mean velocity is not related to the existence of a region of a linear shear stress. Then an analytical relation for the turbulent viscosity was described for the log-law region and for the square-root law region. This model also depends on these two parameters. We concluded that we cannot expect that a model for the turbulent viscosity based on a pressure gradient parameter alone that describes the range of experimental results.

Then we compared the present results for the mean velocity and the Reynolds stresses with other adverse pressure gradient turbulent boundary layer flows in the literature. We found that the analytical model for the total shear stress can describe flows near equilibrium and flows with significant effects of streamwise deceleration. We remark that the model for the total shear stress was found to be sensitive with respect to the values of the parameters and to be influenced significantly by errors and uncertainties in the data. Regarding the similarity of the mean velocity, the profiles for different flows were found to almost collapse provided that the values for the pressure gradient parameter and for the wall shear stress gradient parameter were close to each other. Moreover we showed that the mean-velocity profiles of flows with the same value for the pressure gradient parameter and different values for the wall shear stress gradient parameter do not collapse. We mention that the model implicitely includes some effects of flow history due to the friction velocity.

The observation of mean flow similarity for similar values of Δp_x^+ and $\Delta u_{\tau,x}^+$ was remarkable due to the significant differences in the upstream history of the different flows. For the present flow, the response time of the flow to streamwise changing flow conditions, e.g., from curved to flat wall, was estimated using the eddy turn over time. The corresponding streamwise travelling distance of the mean flow was around 1-2 local boundary layer thickness for the inner 15 % of the boundary layer. From this we concluded that the flow in the inner layer adjusts fast but not instantaneously and expected small history effects, suggesting that higher order effects are negleced by the simple model based on Δp_x^+ and $\Delta u_{\tau,x}^+$. Moreover the role of viscous effects and the location of the thin log-law region compared to a possible mesolayer, proposed by George and Castillo [1997], needs to be studied for adverse pressure gradients.

The present boundary layer flow was subjected to a streamwise changing pressure gradient, curvature and relaxation, and we found several open questions for future research. The first question is on the combination of two effects, i.e., the combined effect of pressure gradient and curvature, and the simultaneous effect of adverse pressure gradient and relaxation from curvature on a flat plate. This would need a series of new experiments with a parametric variation of each effect. The second question is about streamwise changing flows and their delayed response time, i.e., departure from and relaxation towards equilibrium. Then a sufficient number of streamwise stations for detail measurements are needed to study the streamwise evolution of the flow. For the present flow only a single detail measurement position could be studied due to the large amount of time to set-up and to calibrate the 3D Lagrangian particle tracking method. From this we conclude the need to reduce the measurement time for a single station.

Another open question was the possible appearance of longitudinal vortices which could explain the observed spanwise variation of the wall-shear stress from the oil-film interferometry results. We could show that longitudinal Görtler-like vortices could be generated in the concave curvature region of the accelerating ramp, which could be persistent until the begin of the focus region more than at 4 m downstream. The longitudinal vortices could not be studied in detail due to the lack of data. After the measurement campaign we were able to visualise qualitatively the generation of longitudinal vortices as the flow passes the concave curvature ramp.

To answer some of the open questions, we performed a new wind-tunnel experiment within the DLR internal project “VicToria”. The geometry model was modified to increase the adverse pressure gradient and to cause flow separation with a thin recirculation bubble. However, the measurements are still ongoing and the evaluation of the results is subject to future research.

Acknowledgement

The experiment was funded within the DFG-project “Analyse turbulenter Grenzschichten mit Druckgradient bei großen Reynoldszahlen mit hochauflösenden Vielkamera-messverfahren” (Grant KA 1808/14-1 & SCHR 1165/3-1) and by the DLR Institute of Aerodynamics and Flow Technology. The authors gratefully acknowledge the assistance of Martin Bitter, Felix Eich, Rainer Hain, Sven Scharnowski, Janos Agocs and Reinhard Geisler for the wind tunnel experiment. The authors are thankful to Cord Rossow, Rolf Radespiel, Andreas Krumbein, and Dieter Schwamborn for valuable discussions. The authors are very grateful to Per-Age Krogstad, to Gary Coleman, to Michael Manhart and Nikolaus Peller, and to the partners of the International Collaboration on Experimental Turbulence (ICET) and in particular to Sean C. C. Bailey and to Ivan Marusic, for kindly providing their data. The thanks are extended to all authors who put their flow data on the web and for all contributors to the data collection by Coles and Hirst for providing their data in a book for public use.

Appendix A

Flow conditions during the wind-tunnel measurements

In this section we summarise the flow conditions in the wind-tunnel. The reference pressure p_∞ was measured downstream of the model near the exit of the test section. Table A.1 describes the conditions for the different measurement campaigns.

U_∞ in m/s	Meas. techn.	T_∞ in K	p_∞ in Pa	ρ_∞ in kg/m^3	$\mu_\infty \times 10^{-5}$ in Ns/m^2	$\nu_\infty \times 10^{-5}$ in m^2/s
10	2D2C PIV	281.85	95400	1.1791	1.7804	1.5100
10	2D-μPTV	282.52	95455	1.1770	1.7838	1.5155
10	OFI	300.51	95210	1.1021	1.8383	1.6680
23	2D2C PIV	285.43	95010	1.1600	1.7984	1.5503
23	2D-μPTV	284.1	94992	1.1648	1.7918	1.5383
23	OFI	296.76	95006	1.1132	1.8199	1.6349
36	2D2C PIV	284.58	94415	1.1558	1.7942	1.5524
36	2D-μPTV	283.35	94285	1.1592	1.7880	1.5425
36	3D PTV STB	284.58	94415	1.1564	1.7942	1.5515
36	OFI	298.92	94482	1.0971	1.8295	1.6676

Table A.1: Summary of flow conditions in the wind tunnel.

Appendix B

Mean velocity slope diagnostic function for the log-law

We show the results for the mean velocity slope diagnostic function for the 3D LPT data for the case $U_\infty = 36\,\mathrm{m/s}$. In the first step we apply a smoothing to the data, using a Gaussian filter with a kernel of 7 points, i.e., using the data points $i-3,\dots,i+3$ for data point i, corresponding to a half filter width of $8.7\delta_\nu$. In the second step, we use a linear regression with a 3-point stencil $i-1, i, i+1$ for data point i. We find an approximative plateau in the region $84 < y^+ < 152$, which is shown in figure B.1.

For the μPTV data at $U_\infty = 23\,\mathrm{m/s}$, the result is not shown. There are large oscillations for the slope diagnostic function caused by the velocity gradient, if the raw data are used. As a remedy, we used different versions of the smoothing method described above, but the results still show some ambiguity and are less clear than for the case $U_\infty = 36\,\mathrm{m/s}$.

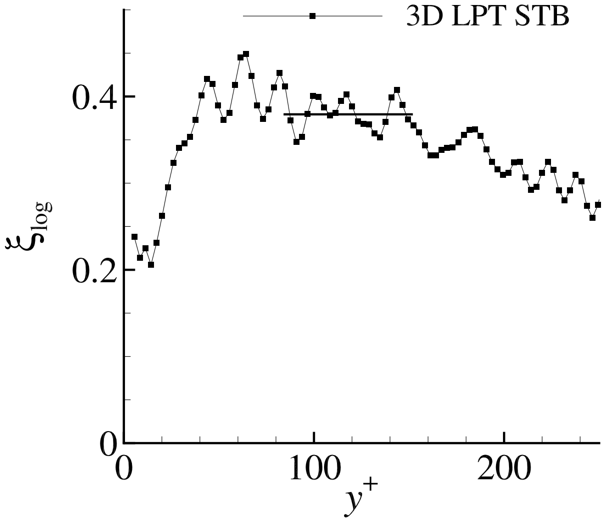

Figure B.1: Mean velocity slope diagnostic function for the log-law for $U_\infty = 36\,\mathrm{m/s}$.

Appendix C

Uncertainty analysis

In this section we describe the uncertainty analysis for the different methods to determine the friction velocity u_τ, and for the evaluation of the log-law slope.

C.1 Determination of the friction velocity from the data in the viscous sublayer

First we consider the uncertainties for the μPTV data for $U_\infty = 23\,\mathrm{m/s}$. For the measurements using oil film interferometry (OFI), the uncertainty ϵ in u_τ is estimated to be 2.0%, which takes into account the uncertainty of the OFI method and the uncertainty in the flow conditions. For comparison Harun et al. [2013] report an uncertainty of 1% and Pailhas et al. [2009] report a value of 1.5%. Then we consider the method to determine u_τ by a least-squares fit of the data to the relation $u^+ = y^+$ in the region $y^+ \in [2 \pm 0.1; 4.6 \pm 0.6]$. The sources of uncertainties identified in this work are listed in table C.1 together with their contribution to the overall uncertainty. For the overall uncertainty for u_τ the estimate is 4.4%.

The uncertainty ϵ for the skin friction coefficient c_f takes into account the relative uncertainty in u_τ and additionally the relative uncertainty in U_∞, which is estimated to be 1.3%. The overall uncertainty in c_f is therefore 11%.

For the method to determine u_τ using a least-squares fit of the data to the

Sources of uncertainties	$\epsilon(u_\tau)$
No reliable data points below $y^+ \leq 1.9$	1.6%
Spreading in $U(y)$ due to not enough samples	0.5%
Uncertainty in the wall position ($\Delta y^+ = 0.3$)	0.5%
Possible systematic error of data points $U(y)$ for $y^+ < 2.6$ (ϵ_U of 2%)	1.3%
Uncertainty due to an estimated uncertainty in ν of 1%	0.5%
Estimated total uncertainty	4.4%

Table C.1: Sources of uncertainties ϵ for the determination of u_τ using a least-squares fit of the data to the viscous sublayer profile $u^+ = y^+$ in the region $y^+ \in [2; 4.6]$ and uncertainty quantification for the μPTV data at $U_\infty = 23\,\mathrm{m/s}$.

Sources of uncertainties	$\epsilon(u_\tau)$
Variation of lower and upper bound for fit $[4 \pm 2, 17 \pm 3]$	<0.1%
Uncertainty in the wall position ($\Delta y^+ = 0.3$)	1.0%
Uncertainty due to an estimated uncertainty in ν of 1%	0.3%
Additional unknown systematic uncertainty	2.5%
Estimated total uncertainty	3.8%

Table C.2: Sources of uncertainties ϵ for the determination of u_τ using a least-squares fit of the data to the profile by Nickels [2004] in the region $y^+ \in [2;20]$ and their quantification for the μPTV data at $U_\infty = 23\,\mathrm{m/s}$.

Sources of uncertainties	$\epsilon(u_\tau)$
Variation of upper bound for fit $y^+ \leq [5, 16.5 \pm 3.5]$	0.3%
Uncertainty in the wall position ($\Delta y^+ = 0.3$)	0.8%
Uncertainty due to an estimated uncertainty in ν of 1%	0.4%
Additional unknown systematic uncertainty	2.5%
Estimated total uncertainty	4.0%

Table C.3: Sources of uncertainties ϵ for the determination of u_τ using a fit to the profile by Nickels [2004] in the region $y^+ \in [5;20]$ for the 3D LPT data for $U_\infty = 36\,\mathrm{m/s}$.

profile by Nickels [2004] in the region $y^+ \in [2;20]$, the sources of uncertainties found in this work and the estimated uncertainties are listed in table C.2. The overall uncertainty for u_τ is estimated to be 3.8%.

Then we consider the estimate for the uncertainties for the 3D LPT data for $U_\infty = 36\,\mathrm{m/s}$ for the method to determine u_τ using a fit to the profile by Nickels [2004] in the region $y^+ \in [5;20]$. The sources of uncertainties found in this work and the estimated uncertainties are listed in table C.3. The overall uncertainty for u_τ is estimated to be 4.0%.

C.2 Determination of the log-law slope

Then we consider the uncertainty for the log-law slope K_i. The sources for uncertainties are the assumed region for the log-law fit, i.e., the lower bound $y^+_{\mathrm{log,min}}$ and the upper bound $y^+_{\mathrm{log,max}}$, and the uncertainty in u_τ. The uncertainty due to the choice of the log-law region is computed by a statistical variation of $y^+_{\mathrm{log,min}}$ and $y^+_{\mathrm{log,max}}$. For the case $U_\infty = 23\,\mathrm{m/s}$ we use for the lower bound $y^+_{\mathrm{log,min}} \in [82;92]$ and for the upper bound $y^+_{\mathrm{log,max}} \in [126;138]$. For the case $U_\infty = 36\,\mathrm{m/s}$ we use for the lower bound $y^+_{\mathrm{log,min}} \in [82;90]$ and for the upper bound $y^+_{\mathrm{log,max}} \in [142;150]$. The corresponding contribution to the relative uncertainty in K_i is 2.0% for the μPTV data for $U_\infty = 23\,\mathrm{m/s}$ and 0.9% for the 3D LPT data for $U_\infty = 36\,\mathrm{m/s}$. The other contributions to the uncertainty in K_i are the uncertainty in u_τ and the uncertainty in ν, which sum up to an additional uncertainty of 2.5% for the case $U_\infty = 23\,\mathrm{m/s}$ and to an uncertainty of 1.2% for the case $U_\infty = 36\,\mathrm{m/s}$. The overall uncertainty is the sum of the uncertainty in u_τ plus this additional uncertainty. The results are

Sources of uncertainties	$\epsilon(K_\mathrm{i})$
Variation of $y^+_{\mathrm{log,min}}$, $y^+_{\mathrm{log,max}}$ within the specified limits	2.0%
Uncertainty in the wall position ($\Delta y^+ = 0.3$)	0.25%
Uncertainty due to an estimated uncertainty in ν of 1%	0.25%
Uncertainty due to 2% uncertainty in u_τ for OFI	2.0%
Uncertainty due to 4.4% uncertainty in u_τ for fit to $u^+ = y^+$	4.4%
Uncertainty due to 3.8% uncertainty in u_τ for fit to profile by Nickels	3.8%
Uncertainty due to 6.1% uncertainty in u_τ for CCM	6.1%

Table C.4: Sources of uncertainties ϵ for the determination of K_i and uncertainty quantification for the μPTV data for $U_\infty = 23\,\mathrm{m/s}$.

Sources of uncertainties	$\epsilon(K_\mathrm{i})$
Variation of $y^+_{\mathrm{log,min}}$, $y^+_{\mathrm{log,max}}$ within the specified limits	0.9%
Uncertainty in the wall position ($\Delta y^+ = 0.3$)	0.3%
Uncertainty due to an estimated uncertainty in ν of 1%	<0.1%
Uncertainty due to 4.0% uncertainty in u_τ for fit to profile by Nickels	4.0%
Uncertainty due to 5.6% uncertainty in u_τ for CCM	5.6%
Uncertainty due to 5.6% uncertainty in u_τ for corrected CCM	5.6%

Table C.5: Sources of uncertainties ϵ for the determination of K_i and uncertainty quantification for the 3D LPT data for $U_\infty = 36\,\mathrm{m/s}$.

summarised for the case $U_\infty = 23\,\mathrm{m/s}$ in table C.4 and for the case $U_\infty = 36\,\mathrm{m/s}$ in table C.5.

C.3 Clauser chart method in the adverse pressure gradient region

We consider the uncertainty of the Clauser chart method (CCM) to determine u_τ for the present data. Monty et al. [2011] report an uncertainty for u_τ of 5% for an adverse pressure gradient beyond $\beta_{RC} = 2$. For the Preston tube, Patel [1965] gives an accuracy within 6% for $\Delta p_x^+ < 0.015$, see also Brown and Joubert [1969]. For the present flow, the deviation of the value for u_τ determined by the Clauser chart is smaller than 5% compared to the value for u_τ from the most reliable method. Therefore we assume a systematic error of 5% for the CCM. Moreover we have to take into account the additional sources for uncertainties. The sensitivity with respect to the interval $[y^+_{\mathrm{log,min}}, y^+_{\mathrm{log,max}}]$ is estimated by a statistical variation of the lower and upper bound. We obtain a relative uncertainty based on the $\pm 2\sigma$-interval of 0.65% for the μPTV data for $U_\infty = 23\,\mathrm{m/s}$. For the 3D LPT data for $U_\infty = 36\,\mathrm{m/s}$, we obtain a value smaller than 0.1%. The results are summarised in table C.6 for the case $U_\infty = 23\,\mathrm{m/s}$ and in table C.7 for the case $U_\infty = 36\,\mathrm{m/s}$.

Sources of uncertainties	$\epsilon(u_\tau)$
Variation of $y^+_{\mathrm{log,min}}$, $y^+_{\mathrm{log,max}}$ within the specified limits	0.2%
Variation of log-law coefficients ($\kappa = 0.41$, $B = 5.0$ vs. $\kappa = 0.384$, $B = 4.17$)	0.3%
Uncertainty of the wall position ($\Delta y^+ = 0.3$)	0.4%
Uncertainty due to an estimated uncertainty in ν of 1%	0.2%
Systematic error of CCM compared to OFI and fit to $u^+ = y^+$	5.0%
Estimated total uncertainty	6.1%

Table C.6: Sources of uncertainties ϵ for the determination of u_τ using the Clauser chart method and uncertainty quantification for the μPTV data at $U_\infty = 23\,\mathrm{m/s}$.

Sources of uncertainties	$\epsilon(u_\tau)$
Variation of $y^+_{\mathrm{log,min}}$, $y^+_{\mathrm{log,max}}$ within the specified limits	0.15%
Variation of log-law coefficients ($\kappa = 0.41$, $B = 5.0$ vs. $\kappa = 0.384$, $B = 4.17$)	0.2%
Uncertainty in the wall position ($\Delta y^+ = 0.3$)	0.05%
Uncertainty due to an estimated uncertainty in ν of 1%	0.15%
Systematic error of CCM compared to OFI and fit to $u^+ = y^+$	5.0%
Estimated total uncertainty	5.6%

Table C.7: Sources of uncertainties ϵ for the determination of u_τ using the Clauser chart method and uncertainty quantification for the 3D LPT data at $U_\infty = 36\,\mathrm{m/s}$.

Appendix D

Empirical correction method for the Clauser chart

We use an empirical method to correct the standard Clauser chart method for u_τ for the 3D LPT data for the case $U_\infty = 36\,\mathrm{m/s}$. For this purpose we use the result found in this work and the similar observation by Monty et al. [2011], that the value for u_τ by the Clauser chart is lower than the value determined by a direct method. Moreover we assume for simplicity that the correction is a linear function of Δp_x^+. Hence the empirical correction for $U_\infty = 36\,\mathrm{m/s}$ is expected to be smaller than for $U_\infty = 23\,\mathrm{m/s}$ due to the lower value for Δp_x^+. Putting this together, we use the empirical correction

$$u_{\tau,\mathrm{CCM+corr},36,v2} = u_{\tau,\mathrm{CCM},36}\left(1 + \frac{u_{\tau,\mathrm{vis},23} - u_{\tau,\mathrm{CCM},23}}{u_{\tau,\mathrm{CCM},23}}\,\frac{\Delta p^+_{x,36}}{\Delta p^+_{x,23}}\right) \tag{D.1}$$

where we use an additional subscript for the reference velocity. This empirically correction yields a value of $u_\tau = 0.7885\,\mathrm{m/s}$. Moreover we use the alternative empirical correction

$$u_{\tau,\mathrm{CCM+corr},36,v1} = u_{\tau,\mathrm{CCM},36}\left(1 + \frac{u_{\tau,\mathrm{vis},23} - u_{\tau,\mathrm{CCM},23}}{u_{\tau,\mathrm{CCM},23}}\right) \tag{D.2}$$

which yields the value $u_\tau = 0.7964\,\mathrm{m/s}$.

Appendix E

An analytical shear stress model for the sqrt-law region

In this section we describe the details used for the derivation of (7.4). In the sqrt-law region, we substitute (2.17) for U^+. The terms of $(U^+)^2$ were integrated individually from the wall to y^+ using the integral calculator Wolfram|Alpha (https://www.wolframalpha.com/calculators/integral-calculator/) and verified using numerical integration. For the relation obtained, we then use two approximations. First, we neglect the arising inverse tanh terms. Second, we avoid the singularity of $\log(y^+)$ as $y^+ \to 0$. Therefore in the second term we replace $(1 + \Delta p_x^+ y^+)^{3/2}$ by $(1 + \Delta p_x^+ y^+)^{3/2} - 1$. Similarly in the eleventh term we replace the $(1 + \Delta p_x^+ y^+)^{1/2}$ by $(1 + \Delta p_x^+ y^+)^{1/2} - 1$. For the present case of $\Delta p_x^+ = 0.011$, these modifications cause only negligible changes for the final result for the relevant y^+-values in the sqrt-law region.

Appendix F

On the possibility of Görtler vortices

In this section we attempt to study the possibility that longitudinal Görtler-like vortices are generated in the concave curvature region of the accelerating ramp at around $x = 3.8\,\text{m}$ and could persist until the begin of the focus region at $x = 8.12\,\text{m}$. Following Bandyopadhyay and Ahmed [1993] we use the turbulent Görtler number based on θ

$$Go_{t,\theta} = \frac{U_e \theta}{\nu_t} \sqrt{\frac{\theta}{R_c}} \tag{F.1}$$

where the turbulent viscosity ν_t is used instead of the laminar viscosity ν, and ν_t is computed from Clauser's relation $\nu_t = 0.018 U_e \delta^*$. Moreover R_c is the radius of curvature with $R_c = 1.08\,\text{m}$. From RANS simulations using the model by Spalart and Allmaras [1992] we estimate the values $\theta = 0.0090\,\text{m}$, $\delta^* = 0.0116\,\text{m}$, and $\delta_{99} = 0.094\,\text{m}$, and we obtain $Go_{t,\theta} = 3.95$.

Denote $\alpha = 2\pi/\lambda$ the wavenumber associated with spanwise non-uniformities of wavelength λ. Then using figure 4 in Tani [1962], disturbances are amplified if $\alpha\theta \lessapprox 1$, i.e., for $\lambda > 0.056\,\text{m}$. Maximum amplification is estimated for $\alpha\theta \approx 0.55$ from figure 3 in Saric [1994], i.e., for $\lambda \approx 0.103\,\text{m}$, which is of the order of the local boundary layer thickness. The corresponding uncertainty in λ is given by the uncertainty of θ plus an additional uncertainty to determine λ from $Go_{t,\theta}$, including the uncertainty in $Go_{t,\theta}$.

The OFI measurements are over a spanwise extent of 0.12 m for one streamwise reference position. However, the data are ambiguous. For $U_\infty = 23\,\text{m/s}$, the pattern of a single wave could be seen. We estimate a wavelength in the range 0.10 m to 0.14 m and an amplitude of 1.3% for u_τ. Thus the theoretically predicted wavelength for maximum amplification is in good agreement with the wavelength of the spanwise variation for c_f. As the diameter of the longitudinal vortices is not smaller than the boundary layer thickness, they are not likely to be destroyed by turbulent mixing, following the argument by Smits et al. [1979]. We estimate the vortex diameter as δ_{99} and the circumferential velocity U_θ as $0.05 U_e$, following again Smits et al. [1979]. The time needed by the vortex to complete one revolution is $T_{\text{rev}} = \pi \delta_{99} / U_\theta$. Then the corresponding streamwise travelling distance $L_x = U_e T_{\text{rev}} = 20\pi\delta_{99}$ is about 5.9 m, using $\delta_{99} = 0.094\,\text{m}$ at

$x = 3.8\,\mathrm{m}$ in the concave bend. This would imply that the longitudinal vortices could persist until the begin of the focus region at $x = 8.12\,\mathrm{m}$.

For $U_\infty = 36\,\mathrm{m/s}$ the spanwise behaviour of c_f shows a maximum near the center of the measurement field and a minimum near its boundary, and the difference between maximum and minimum of u_τ is around 3.8%, corresponding to an amplitude of 1.9% of a possible wave.

Bibliography

R. J. Adrian. Hairpin vortex organization in wall turbulence. *Phys. Fluids*, 19: 041301, 2007.

N. Afzal. Wake layer in turbulent boundary layer with pressure gradient: A new approach. In K. Gersten, editor, *IUTAM Symposium on Asymptotic Methods for Turbulent Shear Flows at High Reynolds Numbers*, pages 95–118. Kluwer Academic Publisher, 1996.

N. Afzal. Turbulent boundary layer with negligible wall stress. *J Fluid Eng. – T. ASME*, 130:051205–1–15, 2008.

A. E. Alving and H. H. Fernholz. Mean-velocity scaling in and around a mild, turbulent separation bubble. *Phys. Fluids*, 7:1956–1969, 1995a.

A. E. Alving and H. H. Fernholz. Turbulence measurements around a mild separation bubble and down-stream of reattachment. *J. Fluid Mech.*, 322: 279–328, 1995b.

A. E. Alving, A. J. Smits, and J. H. Watmuff. Turbulent boundary layer relaxation from convex curvature. *J. Fluid Mech.*, 211:529–556, 1990.

C. Atkinson, V. Kitsios, and J. Soria. Statistics and scaling of axisymmetric turbulent boundary layers under the transition from zero to adverse pressure gradients. In *19th Australasian Fluid Mechanics Conference, Melbourne, Australia 8-11 December 2014*, 2014.

C. Atkinson, A. J. Buchner, M. Eisfelder, V. Kitsios, and J. Soria. Time-resolved PIV measurements of a self-similar adverse pressure gradient turbulent boundary layer. In *18th International Symposium on the Application of Laser and Imaging Techniques to Fluid Mechanics, Lisbon, Portugal, July 4-7, 2016*, 2016.

S. C. C. Bailey, M. Hultmark, J. P. Monty, P. H. Alfredsson, M. S. Chong, R. D. Duncan, J. H. M. Fransson, N. Hutchins, I. Marusic, B. J. McKeon, H. M. Nagib, R. Örlü, A. Segalini, A. J. Smits, and R. Vinuesa. Obtaining accurate mean velocity measurements in high Reynolds number turbulent boundary layers using pitot tubes. *J. Fluid Mech.*, 715:642–670, 2013.

S. C. C. Bailey, M. Vallikivi, M. Hultmark, and A. J. Smits. Estimating the value of von Kármán's constant in turbulent pipe flow. *J. Fluid Mech.*, 749: 79–98, 2014.

P. Bandyopadhyay and A. Ahmed. Turbulent boundary layers subjected to multiple curvatures and pressure gradients. *J. Fluid Mech.*, 246:503–527, 1993.

V. Baskaran, A. J. Smits, and P. N. Joubert. A turbulent flow over a curved hill. Part 1. Growth of an internal boundary layer. *J. Fluid Mech.*, 182:47–83, 1987.

A. Bobke, R. Vinuesa, R. Örlü, and P. Schlatter. History effects and near equilibrium in adverse-pressure-gradient turbulent boundary layers. *J. Fluid Mech.*, 820:667–692, 2017.

P. Bradshaw. *Turbulence*. Springer, 1970.

M. Bross, T. T. Fuchs, and C. J. Kähler. Interaction of coherent flow structures in adverse pressure gradient turbulent boundary layers. *J. Fluid Mech.*, 873: 287–321, 2019.

K. C. Brown and P. N. Joubert. The measurement of skin friction in turbulent boundary layers with adverse pressure gradients. *J. Fluid Mech.*, 35:737–757, 1969.

R. H. Bush, T. S. Chyczewski, K. Duraisamy, B. Eisfeld, C. L. Rumsey, and B. R. Smith. Recommendations for future efforts in RANS modeling and simulation. 2019. AIAA Paper 2019-0317.

L. Castillo, X. Wang, and W. K. George. Separation criterion for turbulent boundary layers via similarity analysis. *J. Fluids Eng.*, 126:297–304, 2004.

K. A. Chauhan, H. M. Nagib, and P. A. Monkewitz. On the composite logarithmic profile in zero pressure gradient turbulent boundary layers. 2007. AIAA Paper 2007-0532.

K. A. Chauhan, J. Philip, C. M. de Silva, N. Hutchins, and I. Marusic. The turbulent/non-turbulent interface and entrainment in a boundary layer. *J. Fluid Mech.*, 742:119–151, 2014a.

K. A. Chauhan, J. Philip, and I. Marusic. Scaling of the turbulent/non-turbulent interface in boundary layers. *J. Fluid Mech.*, 751:298–328, 2014b.

C. Cierpka, S. Scharnowski, and C. J. Kähler. Parallax correction for precise near-wall flow investigations using particle imaging. *Appl. Opt.*, 52:2923–2931, 2013.

G. N. Coleman. personal communication, 2018.

G. N. Coleman, A. V. Garbaruk, and P. R. Spalart. Direct numerical simulation, theories and modelling of wall turbulence with a range of pressure gradients. *Flow, Turbul. Combust.*, 95:261–276, 2015.

G. N. Coleman, S. Pirozzoli, M. Quadrio, and P. R. Spalart. Direct numerical simulation and theory of a wall-bounded flow with zero skin friction. *Flow, Turbul. Combust.*, 99:553–564, 2017.

G. N. Coleman, C. L. Rumsey, and P. R. Spalart. Numerical study of turbulent separation bubbles with varying pressure gradient and Reynolds number. *J. Fluid Mech.*, 847:28–70, 2018.

D. Coles. The law of the wall in turbulent shear flow. In H. H. Görtler and W. Tollmien, editors, *50 Jahre Grenzschichtforschung (50 Years of Boundary Layer Research*, pages 153–163. Vieweg, Braunschweig, 1955.

D. Coles. The law of the wake in the turbulent boundary layer. *J. Fluid Mech.*, 1:191–226, 1956.

D. E. Coles and E. A. Hirst. Computation of Turbulent Boundary Layers - 1968 AFOSR-IFP-Stanford Conference. Thermosciences Division, Department of Mechanical Engineering, Stanford University, 1969.

C. Cuvier, J. M. Foucaut, C. Braud, and M. Stanislas. Characterisation of a high reynolds number boundary layer subject to pressure gradient and separation. *J. Turbul.*, 15:473–515, 2014.

P. Dengel and H. H. Fernholz. An experimental investigation of an incompressible turbulent boundary layer in the vicinity of separation. *J. Fluid Mech.*, 212:615–636, 1990.

S. A. Dixit and O. N. Ramesh. Pressure-gradient-dependent logarithmic laws in sink flow turbulent boundary layers. *J. Fluid Mech.*, 615:445–475, 2008.

S. Drobniak, W. Elsner, A. Drozdz, and M. Materny. Experimental analysis of turbulent boundary layer with adverse pressure gradient corresponding to turbomachinery conditions. In M. Stanislas, J. Jimenez, and I. Marusic, editors, *Progress in Wall Turbulence: Understanding and Modelling*, ERCOFTAC Series, pages 143–150. Springer, 2010.

P. A. Durbin and S. E. Belcher. Scaling of adverse-pressure-gradient boundary layers. *J. Fluid Mech.*, 238:699–722, 1992.

F. Eich. personal communication, 2017.

B. Eisfeld, C. Rumsey, and V. Togiti. Verification and validation of a second-moment-closure model. *AAIA J.*, 54:1524–1541, 2016.

K. Elsberry, J. Loeffler, M. D. Zhou, and I. Wygnanski. An experimental study of a boundary layer that is maintained on the verge of separation. *J. Fluid Mech.*, 423:227–261, 2000.

R. A. Galbraith, S. Sjolander, and M. R. Head. Mixing length in the wall region of turbulent boundary layers. *Aeronaut. Quart.*, 28:97–110, 1977.

W. K. George and L. Castillo. Zero-pressure gradient turbulent boundary layer. *Appl. Mech. Rev.*, 50:689–729, 1997.

M. M. Gibson, C. A. Verriopoulos, and N. S. Vlachos. Turbulent boundary layer on a mildly curved convex surface. *Exp. Fluids*, 2:17–24, 1984.

J. C. Gillis and J. P. Johnston. Turbulent boundary-layer flow and structure on a convex wall and its redevelopment on a flat wall. *J. Fluid Mech.*, 135: 123–153, 1983.

J. C. Gillis, J. P. Johnston, W. M. Kays, and R. J. Moffat. Turbulent boundary layer on a convex curved surface. Technical report, **HMT-31**, Department of Mechanical Engineering, Stanford University, 1980.

P. S. Granville. A modified van Driest formula for the mixing length of turbulent boundary layers in pressure gradients. *J Fluid Eng. – T. ASME*, 111:94–97, 1989.

A. G. Gungor, Y. Maciel, M. P. Simens, and J. Soria. Analysis of a turbulent boundary layer subjected to a strong adverse pressure gradient. *Journal of Physics: Conference Series*, 506:012007, 2014.

A. G. Gungor, Y. Maciel, M. P. Simens, and J. Soria. Scaling and statistics of large-defect adverse pressure gradient turbulent boundary layer. *Int. J. Heat Fluid Flow*, 59:109–124, 2016.

Z. Harun, J. P. Monty, R. Mathis, and I. Marusic. Pressure gradient effects on the large-scale structure of turbulent boundary layers. *J. Fluid Mech.*, 715: 477–498, 2013.

J. O. Hinze. *Turbulence.* McGraw-Hill, 1975.

P. G. Huang and P. Bradshaw. Law of the wall for turbulent flows in pressure gradients. *AAIA J.*, 33:624–632, 1995.

M. Hultmark, M. Vallikivi, S. C. C. Bailey, and A. J. Smits. Turbulent pipe flow at extreme Reynolds numbers. *Phys. Rev. Lett.*, 108:094501, 2012.

M. Inoue, D. I. Pullin, Z. Harun, and I. Marusic. LES of the adverse-pressure gradient turbulent boundary layer. *Int. J. Heat Fluid Flow*, 44:293–300, 2013.

R. Johnstone, G. N. Coleman, and P. R. Spalart. The resilience of the logarithmic law to pressure gradients: evidence from direct numerical simulation. *J. Fluid Mech.*, 643:163–175, 2010.

M. B. Jones, I. Marusic, and E. E. Perry. Evolution and structure of sink-flow turbulent boundary layers. *J. Fluid Mech.*, 428:1–27, 2001.

B. A. Kader and A. M. Yaglom. Similarity treatment of moving-equilibrium turbulent boundary layers in adverse pressure gradients. *J. Fluid Mech.*, 89: 305–342, 1978.

C. J. Kähler, U. Scholz, and J. Ortmanns. Wall-shear-stress and near-wall turbulence measurements up to single pixel resolution by means of long-distance micro-PIV. *Exp. Fluids*, 41:327–341, 2006.

C. J. Kähler, S. Scharnowski, and C. Cierpka. On the resolution limit of digital particle image velocimetry. *Exp. Fluids*, 52:1629–1639, 2012a.

C. J. Kähler, S. Scharnowski, and C. Cierpka. On the uncertainty of digital PIV and PTV near walls. *Exp. Fluids*, 52:1641–1656, 2012b.

R. Kiel. *Experimentelle Untersuchung einer Strömung mit beheiztem lokalen Ablösewirbel an einer geraden Wand.* PhD thesis, Dissertation Ruhr-Universität Bochum, also VDI Fortschrittsbericht, Reihe 7, Nr. 281, VDI-Verlag Düsseldorf, 1995.

N. Kim and D. L. Rhode. Streamwise curvature effect of the incompressible turbulent mean velocity over curved surfaces. *J Fluid Eng. – T. ASME*, 122: 547–551, 2000.

V. Kitsios, C. Atkinson, J. A. Sillero, G. Borell, A. G. Gungor, J. Jimenez, and J. Soria. Direct numerical simulation of a self-similar adverse pressure gradient turbulent boundary layer. *Int. J. Heat Fluid Flow*, 61:129–136, 2016.

V. Kitsios, A. Sekimoto, C. Atkinson, J. A. Sillero, G. Borell, A. G. Gungor, J. Jimenez, and J. Soria. Direct numerical simulation of a self-similar adverse pressure gradient turbulent boundary layer at the verge of separation. *J. Fluid Mech.*, 829:392–419, 2017.

T. Knopp. A new wall-law for adverse pressure gradient flows and modification of k-ω type RANS turbulence models. 2016. AIAA Paper 2016-0588.

T. Knopp and A. Probst. An algebraic sensor for the RANS-LES switch in delayed detached-eddy simulation. In *New Results in Numerical and Experimental Fluid Mechanics VIII*, volume 121 of *Notes on Numerical Fluid Mechanics and Multidisciplinary Design*, pages 457–464, 2013.

T. Knopp, D. Schanz, A. Schröder, M. Dumitra, R. Hain, and C. J. Kähler. Experimental investigation of the log-law for an adverse pressure gradient turbulent boundary layer flow at Re_θ up to 10000. *Flow, Turbul. Combust.*, 92:451–471, 2014.

T. Knopp, N. A. Buchmann, D. Schanz, B. Eisfeld, C. Cierpka, R. Hain, A. Schröder, and C. J. Kähler. Investigation of scaling laws in a turbulent boundary layer flow with adverse pressure gradient using PIV. *J. Turbul.*, 16: 250–272, 2015.

T. Knopp, N. Reuther, M. Novara, E. Schülein, D. Schanz, A. Schröder, and C. J. Kähler. Investigation of a turbulent boundary layer flow at high Reynolds number using particle-imaging and implications for RANS modeling. In *Tenth International Symposium on Turbulence and Shear Flow Phenomena (TSFP10) July 6-9, 2017, Swissotel, Chicago-IL, USA*, 2017.

Y. S. Kwon, N. Hutchins, and J. P. Monty. On the use of the Reynolds decomposition in the intermittent region of turbulent boundary layers. *J. Fluid Mech.*, 794:5–16, 2016.

J.-H. Lee and H. J. Sung. Effects of an adverse pressure gradient on a turbulent boundary layer. *Int. J. Heat Fluid Flow*, 29:568–578, 2008.

J.-H. Lee and H. J. Sung. Structures in turbulent boundary layers subjected to adverse pressure gradients. *J. Fluid Mech.*, 639:101–131, 2009.

P. Luchini. Universality of the turbulent velocity profile. *Phys. Rev. Lett.*, 118: 224501, 2017.

Y. Maciel, K. S. Rossignol, and J. Lemay. Self-similarity in the outer region of adverse-pressure-gradient turbulent boundary layers. *AAIA J.*, 44:2450–2464, 2006a.

Y. Maciel, K. S. Rossignol, and J. Lemay. A study of a separated turbulent boundary layer in stalled-airfoil-type flow conditions. *Exp. Fluids*, 41:573–590, 2006b.

Y. Maciel, T. Wei, and A. G. Gungor M. P. Simens. Outer scales and parameters of adverse-pressure-gradient turbulent boundary layers. *J. Fluid Mech.*, 844: 5–35, 2018.

M. Manhart and R. Friedrich. DNS of a turbulent boundary layer with separation. *Int. J. Heat Fluid Flow*, 23:672–581, 2002.

M. Manhart, N. Peller, and C. Brun. Near-wall scaling for turbulent boundary layers with adverse pressure gradient. *Theor. Comput. Fluid Dyn.*, 22:243–260, 2008.

I. Marusic and A. E. Perry. A wall-wake model for the turbulence structure of boundary layers. Part 2. Further experimental support. *J. Fluid Mech.*, 298: 389–407, 1995.

I. Marusic, J. P. Monty, M. Hultmark, and A. J. Smits. On the logarithmic region in wall turbulence. *J. Fluid Mech.*, 716:R3–1–R3–11, 2013.

I. Marusic, K. A. Chauhan, V. Kulandaivelu, and N. Hutchins. Evolution of zero-pressure-gradient boundary layers from different tripping conditions. *J. Fluid Mech.*, 783:379–411, 2015.

Y. Marusic and J. P. Monty. Attached eddy model of wall turbulence. *Annu. Rev. Fluid Mech.*, 51:49–74, 2019.

H. McDonald. The effect of pressure gradient on the law of the wall in turbulent flow. *J. Fluid Mech.*, 35:311–336, 1969.

G. L. Mellor. The effects of pressure gradients on turbulent flow near a smooth wall. *J. Fluid Mech.*, 24:255–274, 1966.

G. L. Mellor and D. M. Gibson. Equilibrium turbulent boundary layers. *J. Fluid Mech.*, 24:225–253, 1966.

J. P. Monty, Z. Harun, and I. Marusic. A parametric study of adverse pressure gradient turbulent boundary layers. *Int. J. Heat Fluid Flow*, 32:575–585, 2011.

Y. Nagano, M. Tagawa, and T. Tsuji. Effects of adverse pressure gradients on mean flows and turbulence statistics in a boundary layer. In *Eighth symposium on turbulent shear flows, Technical University of Munich, September 9-11, 1991*, 1991.

H. M. Nagib and K. A. Chauhan. Variations of von Kármán coefficient in canonical flows. *Phys. Fluids*, 20:101518–1–10, 2008. doi: 10.1063/1.3006423.

T. B. Nickels. Inner scaling for wall-bounded flows subject to large pressure gradients. *J. Fluid Mech.*, 521:217–239, 2004.

M. J. Nituch, S. Sjolander, and M. R. Head. An improved version of the Cebeci-Smith eddy-viscosity model. *Aeronaut. Quart.*, 29(3):207–225, 1978.

M. Novara, D. Schanz, N. Reuther, C. J. Kähler, and A. Schröder. Lagrangian 3D particle tracking in high-speed flows: Shake-The-Box for multi-pulse systems. *Exp. Fluids*, 57:128 1–20, 2016.

M. Novara, D. Schanz, R. Geisler, S. Gesemann, C. Voss, and A. Schröder. Multi-exposed recordings for 3D Lagrangian particle tracking with multi-pulse Shake-The-Box. *Exp. Fluids*, 60:44–63, 2019.

R. Örlü, J. H. M. Fransson, and P. H. Alfredsson. On near wall measurements of wall bounded flows - the necessity of an accurate determination of the wall position. *Prog. Aerosp. Sci.*, 46:353–387, 2010.

J. M. Österlund, A. V. Johansson, H. M. Nagib, and M. H. Hites. A note on the overlap region in turbulent boundary layers. *Phys. Fluids*, 12:1–4, 2000.

G. Pailhas, P. Barricau, Y. Touvet, and L. Perret. Friction measurement in zero and adverse pressure gradient boundary layer using oil droplet interferometric method. *Exp. Fluids*, 47:195–207, 2009.

V. C. Patel. Calibration of the preston tube and limitations on its use in pressure gradients. *J. Fluid Mech.*, 23:185–208, 1965.

A. E. Perry. Turbulent boundary layers in decreasing adverse presssure gradients. *J. Fluid Mech.*, 25:481–506, 1966.

A. E. Perry and W. H. Schofield. Mean velocity and shear stress distributions in turbulent boundary layers. *Phys. Fluids*, 16:2068–2074, 1973.

A. E. Perry, J. B. Bell, and P. N. Joubert. Velocity and temperature profiles in adverse pressure gradient turbulent boundary layers. *J. Fluid Mech.*, 25: 299–320, 1966.

St. B. Pope. *Turbulent flows.* Cambridge University Press, 2000.

A. Probst, R. Radespiel, and T. Knopp. Detached-eddy simulation of aerodynamic flows using a Reynolds-stress background model and algebraic RANS/LES sensors. 2011. AIAA Paper 2011-3206.

B. R. Ramaprian and B. G. Shivaprasad. The structure of turbulent boundary layers along mildly curved surfaces. *J. Fluid Mech.*, 85:273–303, 1978.

M. S. Rao and H. A. Hassan. Modeling turbulence in the presence of adverse pressure gradients. *J. Aircraft*, 35:500–502, 1998.

N. Reuther and C. J. Kähler. Evaluation of large-scale turbulent/non-turbulent interface detection methods for wall-bounded flows. *Exp. Fluids*, 59:121 1–17, 2018.

N. Reuther and C. J. Kähler. Effect of intermittency on the outer scales in turbulent boundary layers. In *11th International Symposium on Turbulence and Shear Flow Phenomena (TSFP-11), Southampton, UK, July 30 - August 2, 2019*, 2019.

N. Reuther, S. Scharnowski, R. Hain, D. Schanz, A. Schröder, and C. J. Kähler. Experimental investigation of adverse pressure gradient turbulent boundary layers by means of large-scale PIV. In *11th International Symposium on Particle Image Velocimetry - PIV15, Santa Barbara, California, September 14-16, 2015*, 2015.

J. C. Rotta. Turbulent boundary layers in incompressible flow. *Prog. Aeronaut. Sci.*, 2:1–219, 1962.

A. E. Samuel and P. N . Joubert. A boundary layer developing in an increasingly adverse pressure gradient. *J. Fluid Mech.*, 66:481–505, 1974.

S. Saric. Görtler Vortices. *Annu. Rev. Fluid Mech.*, 26:379–409, 1994.

D. M. Schatzman and F. O. Thomas. An experimental investigation of an unsteady adverse pressure gradient turbulent boundary layer: embedded shear layer scaling. *J. Fluid Mech.*, 815:592–642, 2017.

B. Scheichl and A. Kluwick. On turbulent marginal separation: How the logarithmic law of the wall is superseeded by the half-power law. In *Proceedings of International Conference on Boundary and Interior Layers BAIL 2006, Göttingen*, 2006.

B. Scheichl and A. Kluwick. On turbulent marginal boundery layer separation: How the half-power law superseedes the logarithmic law of the wall. *Int. J. Comput. Sci. Math.*, 1:343–359, 2007.

P. Schlatter and R. Örlü. Assessment of direct numerical simulation data of turbulent boundary layers. *J. Fluid Mech.*, 659:1–11, 2010.

W. H. Schofield. Equilibrium boundary layers in moderate to strong adverse pressure gradient. *J. Fluid Mech.*, 113:91–122, 1981.

W. H. Schofield. Two-dimensional separating turbulent boundary layers. *AAIA J.*, 24:1611–1620, 1986.

E. Schülein, N. Reuther, and T. Knopp. Optical skin friction measurements in a turbulent boundary layer with pressure gradient. In *New Results in Numerical and Experimental Fluid Mechanics. Contributions to the 20th STAB/DGLR Symposium Braunschweig, Germany 2016*, pages 95–104, 2017.

J. A. Sillero, J. Jimenez, and R. D. Moser. One-point statistics for turbulent wall-bounded flows at reynolds numbers up to $\delta^+ \approx 2000$. *Phys. Fluids*, 25: 105102–1, 2013.

D. Simmons, F. O. Thomas, and T. C. Corke. Smooth body flow separation experiments and their surface flow topology characterization. 2019. AIAA Paper 2019-3085.

R. L. Simpson. A model for the backflow mean velocity profile. *AAIA J.*, 21: 142–143, 1983.

R. L. Simpson, Y. T. Chew, and B. G. Shivaprasad. The structure of a separating turbulent boundary layer. Part 2. Higher-order turbulence results. *J. Fluid Mech.*, 113:53–73, 1981.

P. E. Skare and P. A. Krogstad. A turbulent equilibrium boundary layer near separation. *J. Fluid Mech.*, 272:319–348, 1994.

A. Skote and D. S. Henningson. Direct numerical simulation of a separated turbulent boundary layer. *J. Fluid Mech.*, 471:107–136, 2002.

A. J. Smits, S. T. B. Young, and P. Bradshaw. The effect of short regions of high surface curvature on turbulent boundary layers. *J. Fluid Mech.*, 94:209–242, 1979.

R. M. C. So and G. L. Mellor. Experiment on convex curvature effects in turbulent boundary layers. *J. Fluid Mech.*, 60:43–62, 1973.

J. Soria, C. Willert, O. Amili, J. Klinner, C. Atkinson, M. Stanislas, A. Schröder, R. Geisler, J. Agocs, A. Röse, C. J. Kähler, S. Scharnowski, R. Hain, J. M. Foucaut, C. Cuvier, S. Srinath, and J. P. Laval. Spatially and temporally resolved 2C-2D PIV in the inner layer of a high Reynolds number adverse pressure gradient turbulent boundary layer. In *8th Internatinal Symposium on the Application of Laser and Imaging Techniques to Fluid Mechanics, July 4-7, 2016, Lisbon, Portugal*, 2016.

P. R. Spalart. The law of the wall. indications from DNS, and opinion. In J. Jimenez M. Stanislas and I. Marusic, editors, *Progress in Wall Turbulence : Understanding and Modelling. Proceedings of the WALLTURB International Workshop held in Lille, France, April 21-23, 2009*, ERCOFTAC Series, pages 9–20. Springer, 2010.

P. R. Spalart. Philosophies and fallacies in turbulence modeling. *Prog. Aerosp. Sci.*, 74:1–15, 2015.

P. R. Spalart and S. R. Allmaras. A one-equation turbulence model for aerodynamics flows. 1992. AIAA Paper 1992-0439.

B. S. Stratford. The prediction of separation of the turbulent boundary layer. *J. Fluid Mech.*, 5:1–16, 1959.

W. Szablewski. Turbulente Strömungen in divergenten Kanälen. *Ing.-Arch.*, 22: 268–281, 1954.

W. Szablewski. Analyse von Messungen turbulenter Grenzschichten mittels der Wandgesetze. *Ing.-Arch.*, 29:291–300, 1960.

I. Tani. Production of longitudinal vortices in the boundary layer along a concave wall. *J. Geophys. Res.*, 77:3075–3080, 1962.

M. M. M. El Telbany and A. J. Reynolds. Velocity distributions in plane turbulent channel flows. *J. Fluid Mech.*, 100:1–29, 1980.

B. G. J. Thompson. A new two-parameter family of mean velocity profiles for incompressible turbulent boundary layers on smooth walls. Technical report, ARC R & M 3463, 1967.

A. A. Townsend. Equilibrium layers and wall turbulence. *J. Fluid Mech.*, 11: 97–120, 1961.

A. A. Townsend. *The Structure of Turbulent Shear Flow.* Cambridge University Press, 1976.

B. van den Berg. The law of the wall in two- and three-dimensional turbulent boundary layers. Technical Report NLR TR 72111 U, National Aerospace Laboratory NLR, Amsterdam, 1973.

B. van den Berg. A three-dimensional law of the wall for turbulent shear flows. *J. Fluid Mech.*, 70:149–160, 1975.

D. Vieth. *Berechnung der Impuls- und Wärmeübertragung in ebenen turbulenten Strömungen mit Ablösung bei hohen Reynolds-Zahlen.* PhD thesis, Ruhr Universität Bochum, 1996.

C. S. Vila, R. Örlü, R. Vinuesa, P. Schlatter, A. Ianiro, and S. Discetti. Adverse-pressure-gradient effects on turbulent boundary layers: Statistics and flow-field organization. *Flow, Turbul. Combust.*, 99:589–612, 2017.

R. Vinuesa, A. Bobke, R. Örlü, and P. Schlatter. On determining characteristic length scales in pressure-gradient turbulent boundary layers. *Phys. Fluids*, 28:055101, 2016.

R. Vinuesa, P. S. Negi, M. Atzori, A. Hanifi, D. S. Henningson, and P. Schlatter. Turbulent boundary layers around wing sections up to $Re_c = 1,000,000$. *Int. J. Heat Fluid Flow*, 72:86–99, 2018.

T. Wei, P. Fife, J. Klewicki, and P. McMurtry. Properties of the mean momentum balance in turbulent boundary layer, pipe and channel flows. *J. Fluid Mech.*, 522:303–327, 2005a.

T. Wei, R. Schmidt, and P. McMurtry. Comment on the Clauser chart method for determining the friction velocity. *Exp. Fluids*, 38:695–699, 2005b.

K. Wieghardt and W. Tillmann. Zur turbulenten Reibungsschicht bei Druckanstieg. Technical report, Untersuchungen und Mitteilungen der deutschen Luftfahrtforschung UM 6617, 1944.

D. C. Wilcox. *Turbulence modeling for CFD.* DWC Industries, La Canada, 1998.

C. Willert, J. Soria, C. Cuvier, J. M. Foucaut, and J. P. Laval. Flow reversal in turbulent boundary layers with varying pressure gradients. In *19th Internatinal Symposium on the Application of Laser and Imaging Techniques to Fluid Mechanics, July 16-19, 2018, Lisbon, Portugal*, 2018.

M. V. Zagarola and A. J. Smits. Scaling of the mean velocity profile for turbulent pipe flow. *Phys. Rev. Lett.*, 78(2):239–242, Jan 1997. doi: 10.1103/PhysRevLett.78.239.